Studies of Cobalt Fischer-Tropsch Catalysts using Electron Microscopy

Ofentse A. Makgae

Linacre College

University of Oxford

Supervisor: Angus I. Kirkland

Co-Supervisor: Emanuela Liberti

A thesis submitted for the degree of

Doctor of Philosophy

Trinity 2020

DEDICATION

To my grandmother, Mary Makgae

&

The rest of my family

"Now unto Him who is able to do exceedingly abundantly above all that we ask or think…" Ephesians 3:20

ACKNOWLEDGEMENTS

Firstly, I want to thank the Rhodes Trust and the Rhodes Scholarships for investing in my potential, which allowed me to have the world-class Oxford experience.

My supervisors: Prof. Angus Kirkland and Dr. Emanuela Liberti, thank you for allowing me to learn from your wisdom & experience, and for all the support and guidance throughout my study.

Most importantly, a huge gratitude to my family for the patience and support throughout my studies to this date.

Mr. Arthur Moya, thank you for the support, sharing experiments and ideas throughout our studies.

I am thankful to Dr. Chen Huang, for all the help with the experimental microscopy lessons and ideas, from the OJ to the GrandARM.

I would also like to thank the David Cockayne Centre for Electron Microscopy and electron Physical Sciences Imaging Centre (ePSIC) for all the training and experiments.

A sincere gratitude to the Oxford Electron Image Analysis Group for all the ideas that contributed to the success of this study.

To Professor Neil Coville and Dr. Tumelo Phaahlamohlaka; many thanks for the catalysts, experimental ideas and discussions. Dr. Benzhen Yao and Dr. Sergio Gonzales-Cortes for help with the *ex-situ* reduction experiments and specimen storage.

To all my close friends, thank you for the support, motivation and inspiration.

LIST OF PRESENTATIONS

Makgae, O. et al., Activation of Co Fischer-Tropsch catalyst: Exploring Co valence state and atomic structure under different reduction conditions using aberration-corrected STEM-EELS. 2019. *Microscopy and Microanalysis*. Portland, Oregon, USA. (**Poster**)

Makgae, O. et al., High-resolution imaging of Co_3O_4 nanoparticles via aberration-corrected exit wavefunction reconstruction. 2018. *International Microscopy Congress*. Syndey, Australia. (**Digital poster)**

Makgae, O. et al., Studies of carbon-supported Co3O4 nanocrystals using aberration-corrected exit wavefunction reconstruction. 2018. *Electron Microscopy and Analysis Group* (EMAG). Warwick, UK. (**Poster**).

Makgae, O. et al., Atomically resolved structure and active sites of Co3O4. 2017. *Proceedings of the Microscopy Society of Southern Africa*. Limpopo, South Africa. (**Oral, Fiona Graham Prize**)

LIST OF PUBLICATIONS

Makgae, O., Moya, A., Yao, B., Schuster, M., Edwards, P., Liberti, E., & Kirkland, A. (2019). Activation of Co Fischer-Tropsch Catalyst: Exploring Co Valence State under Different Reduction Conditions Using STEM-EELS. *Microscopy and Microanalysis*, *25*(S2), 668-669. doi:10.1017/S1431927619004070

Moya, A., **Makgae, O**., Liberti, E., & Kirkland, A. (2019). A Semi-quantitative Predictive Model for SnO2 Adatom Diffusion & Its Application to Exit Wave Reconstruction. *Microscopy and Microanalysis, 25*(S2), 108-109. doi:10.1017/S1431927619001272

Yao, B., Xiao, T., **Makgae, O**., Jui, X., Gonzales-Cortes, S., Guan, S., Kirkland, A.I., Dilworth, J.R., Thomas, J.M., & Edwards, P.P. (2020) Transforming Carbon Dioxide into Jet Fuel using an Organic Combustion-Synthesized Fe-Mn-K Catalyst. *Nature Communication* (in review).

Makgae, O., Moya, A., Huang, C., Liberti, E., & Kirkland, A.I. (2020) Atomically resolved active surfaces of supported Co_3O_4 catalyst with resolved surface lattice O atomic columns. (in preparation).

Makgae, O., Yao, B., Moya, A., Schuster, M., Edwards, P.P., Liberti, E., & Kirkland, A.I. (2020) Exploring the atomic structure and valence state of Co in the activation of Fischer-Tropsch catalysts under H_2 vs syngas (in preparation).

DECLARATION

I hereby declare that this thesis is my own original work. It has not been submitted for examination at any other University. Further, I have acknowledged all sources used and have cited these in the reference section.

The Co_3O_4 precursor used in this thesis was provided by Prof. Neil Coville from the University of the Witwatersrand. Mr. Arthur Moya performed the multislice simulations in Chapter 4. The *ParticleSpy* script used in Chapter 5 was developed by Dr. T. Slater.

ABSTRACT

The composition of reducing gas in the activation of Co Fischer-Tropsch (FT) catalyst has a direct influence on catalytic performance during FT synthesis. The nature of the reduction conditions of Co_3O_4 to metallic Co determines the active sites on the final Co FT catalyst, and its subsequent reactivity. Specifically, syngas activated Co FT catalysts have been known to have a higher catalytic performance compared to H_2. However, little is known about the Co physicochemical properties as a function of activation gas composition due to the rapid oxidation of Co in air. Electron microscopy (EM) has been used to probe various properties of materials under different environments with a high spatial resolution; thus, providing an understanding of the relationship between the surface structure and chemistry (spectroscopy) of materials on a local scale. Current literature on the studies of the activation of Co FT catalysts using electron microscopy (EM) has focused on the activation of Co FT catalysts in H_2, since H_2 activation is older and well understood. However, to date, there is limited literature on the activation of Co FT catalysts in syngas or the comparison of the effect of activation gas composition between syngas and H_2 using EM. Thus, this thesis expands our understanding of Co activation in Fischer-Tropsch synthesis by comparing, for the first time, catalyst activation under H_2 and syngas (H_2/CO = 2) using both *ex-situ* and *in-situ* high-resolution aberration-corrected analytical electron microscopy to determine the most effective routes for the activation of Co where maximum reduction is achieved.

Initially, the atomic structure of the active surfaces for CO and H_2 adsorption of a Co_3O_4 precursor supported on hollow carbon spheres were determined along several projections using focal series exit wavefunction reconstruction. The electron dose per frame in a focal series

required to restore the specimen exit wavefunction, where both oxygen and cobalt atomic columns are resolved without visible beam-induced damage, is determined. Subsequently, the active surface terminations of Co_3O_4 with resolved O, and Co atomic columns are presented and compared to calculated Co_3O_4 active surfaces for CO and H_2 adsorption and dissociation from density functional theory studies. Based on this comparison, the potential reactivity of the various Co_3O_4 surfaces towards reducing gases (H_2 and CO from syngas) is discussed.

The Co_3O_4 precursor was subsequently examined following *ex-situ* reduction under H_2 and syngas at 350°C. The physicochemical properties of the 350 °C *ex-situ* activated catalysts were investigated using annular dark-field high-resolution scanning transmission electron microscopy, in conjunction with electron energy loss spectroscopy. The high-resolution images and Co-$L_{3,2}$ and O-K edge fine structure features in the H_2 and syngas activated catalysts revealed better reducibility in syngas in contrast to H_2 at 350°C. These differences in the physicochemical properties of the Co catalyst activated under H_2 and syngas are discussed in relation to the thermodynamics of the reaction between Co_3O_4 and both reducing gases. The surface re-oxidation of Co in the air compared to the incomplete reduction of the catalyst is addressed, and the effect of increased activation temperature on the catalyst re-oxidation or incomplete reduction is explored. The disadvantage of high-temperature catalyst activation is also discussed. Finally, *in-situ* activation of Co FT catalysts under H_2 and syngas is proposed as a viable option to study the activation process, protected from atmospheric air, at near *operando* conditions. Both *ex-situ* and *in-situ* results indicate that syngas activation is the most effective method to obtain an active metallic Co sinter resistant catalyst at lower temperatures.

TABLE OF CONTENTS

LIST OF FIGURES

LIST OF TABLES

GLOSSARY

FT: Fischer-Tropsch.

EELS: electron energy loss spectroscopy.

HRTEM: high-resolution transmission electron microscope.

STEM: scanning transmission electron microscope.

ADF: annular dark field.

PCTF: phase-contrast transfer function.

DFT: density functional theory.

TEM: transmission electron microscope.

EWR: exit wavefunction reconstruction

Chapter 1 : Introduction

1.1 Overview of Thesis

Chapter 1: Provides an introduction to the background of this study and the proposed contribution to the field.

Chapter 2: Provides a detailed literature review on Co Fischer-Tropsch (FT) synthesis, including factors affecting the activation of Co FT catalyst, with an emphasis on the effect of activation gas composition. The chapter also discusses the limitations of conventional characterisation of Co FT catalysts and highlights the benefits of aberration-corrected analytical scanning transmission electron microscopy.

Chapter 3: Summarises the theory of image formation in transmission and scanning transmission electron microscopy, and a brief introduction to focal series exit wavefunction reconstruction. The chapter also discusses the *in-situ* electron microscopy technique, including the gas holder, microelectromechanical systems (MEMS) chip, and *in-situ* experimental details. Principles of electron energy loss spectroscopy, including the experimental imaging conditions used in the study, are also discussed.

Chapter 4: Reports on the characterisation of the precursor spinel Co_3O_4 using dose fractionated focal series exit wavefunction reconstruction. In this chapter, the electron dose required for specimen exit wavefunction reconstruction of Co_3O_4 is determined. The atomic structure and surface terminations of Co_3O_4 from several projections determined from the

restored phase of the specimen exit wavefunction are described. These are subsequently compared to theoretically known Co_3O_4 active sites for CO and H_2 adsorption.

Chapter 5: Reports on the activation of Co FT catalysts using H_2 and syngas. This chapter explores the Co structure-chemistry relationship as a function of activation gas composition. Studies of both *ex-situ* and *in-situ* activation of the Co FT catalyst (catalyst morphology, atomic structure, and Co valence state) are presented.

Chapter 6: Provides conclusions and recommendations for future work.

1.2 Background

Fischer-Tropsch (FT) synthesis is one of the most profitable and oldest catalytic reaction involving the hydrogenation of carbon monoxide into petroleum products over a transition metal catalyst (e.g. cobalt).[1,2] Biomass-derived syngas (a mixture of CO and H_2) has seen this process become increasingly attractive over the past few years due to strictly growing environmental regulations and increasing demand for biofuel to mitigate the effects of climate change.[3,4] In a typical industrial FT synthesis, precursor Co_3O_4 is activated in a fixed-bed reactor by introducing H_2 to convert the oxide into catalytically active metallic Co, after which syngas is passed through the reactor to produce petroleum products.[5]

The activation process is arguably the most crucial step in FT synthesis because it determines the evolution of catalytically active sites on Co during the conversion of Co_3O_4 to metallic Co under reducing gas atmosphere.[6,7] Additionally, studies have shown that the activation of Co FT catalysts has a direct influence on the catalytic activity and selectivity of the Co FT catalyst.[7–11] More specifically, it has been shown that activating the catalyst under H_2, results in a lower catalytic activity compared to activation with syngas (either a mixture or a sequential

CO & H_2 treatment).[7–11] The reason behind this is still not well understood. However, it is generally believed that the presence of CO during the activation of Co FT catalysts in syngas or sequential CO & H_2 leads to the formation of Co_2C which decomposes into hexagonal close-packed (hcp) Co.[7,9,10,12] In contrast to the face-centred cubic (fcc) Co formed during H_2 activation in the absence of CO.[7,9,10,12] Theoretical studies (density functional theory (DFT)) have shown that fcc Co surfaces consists mostly of the sites that are inactive for CO dissociation; a rate-determining step in FT synthesis, while hcp Co surfaces consists mainly of active sites for CO dissociation.[13]

These theoretical studies may provide insight into the relationship between catalyst structure (hcp vs fcc) and performance; however, they do not reveal any correlation between activation and structure.[13] The catalyst activation is a dynamic process with multiple variables (high-temperature gas-solid interactions) and thus requires detailed experimental characterisation for the process to be fully understood. However, the sensitivity of metallic Co to oxidation in the air has made the characterisation of the physicochemical properties of the Co catalysts a significant challenge.[14] As a result, the majority of characterisation studies of the active Co FT catalyst has relied on the bulk X-ray techniques[6,15,16], and temperature-programmed reduction[17] studies. For example, an *in-situ* XRD study of the activation of Co catalysts under H_2 versus sequential Co & H_2 showed that H_2 activation produced mainly fcc Co, while sequential Co & H_2 produced hcp Co.[6] Despite the usefulness and success of these techniques at determining the optimum Co_3O_4 reduction temperature and resultant Co phase as a function of activation parameters, they lack the necessary spatial resolution and the ability to directly correlate the physicochemical properties (i.e. catalyst morphology, atomic structure, and valence state) of the Co catalyst to its performance.

The development of aberration-corrected (scanning) transmission electron microscopy with *in-situ* capabilities has offered a great advantage to the understanding of catalysts under near

operando conditions.[18–20] In parallel, electron energy loss spectroscopy (EELS) can be used to obtain information about the valence state of Co from the Co-$L_{3,2}$ and O-K edge fine structure features (The L_3/L_2 peak intensity ratio of the Co-$L_{3,2}$ edge, the $L_{3,2}$ peak-to-peak energy separation, and the position of the L_3 peak, as well as the O-K pre-peak).[21–24] A combination of both techniques can, therefore, provide direct structural and chemical information of the activated Co FT catalyst at high spatial resolution. This has driven a growing interest in the application of electron microscopy to understand how the activation conditions of Co FT catalyst affect the reducibility and overall physicochemical properties of the active catalyst.[11,25,26]

1.3 Research Aims and Objectives

Despite recent efforts in the studies of Co catalyst activation using electron microscopy[11,25,26], there is still insufficient knowledge about the physicochemical properties of the active Co catalyst as a function of the different variables known to affect the activation process from bulk X-ray techniques, in particular the activation gas composition. The aim of this D.Phil. is to provide new insights into the effect of gas composition on the activation of Co FT catalysts using *ex-situ* and *in-situ* aberration-corrected analytical scanning transmission electron microscopy. The following key research questions will be explored in this study:

a) Which surface terminations are found on the precursor Co_3O_4, and how do they compare to the theoretical Co_3O_4 surface terminations known to be active for CO and H_2 adsorption and dissociation?
b) What is the difference in the morphology, structure, and chemistry (valence state) of the Co FT catalyst when activated in H_2 compared to syngas activation?
c) How does temperature affect the properties mentioned in (b)?

The answers to these questions will provide significant insights into the effect of gas composition on the structure-chemistry relationships in Co FT catalysts. It will further serve to improve our understanding of the relationship between catalyst activation and performance in Fischer-Tropsch synthesis beyond the conventional paradigm.

1.4 References

(1) Fischer, F.; Tropsch, H. *Berichte der Dtsch. Chem. Gesellschaft A B Ser.* **1926**, *59* (4), 830–831.

(2) Dry, M. E. *Catal. Today* **2002**, *71* (3), 227–241.

(3) Tijmensen, M. J. A.; Faaij, A. P. C.; Hamelinck, C. N.; van Hardeveld, M. R. M. *Biomass and Bioenergy* **2002**, *23* (2), 129–152.

(4) van Steen, E.; Claeys, M. *Chem. Eng. Technol.* **2008**, *31* (5), 655–666.

(5) Iglesia, E. *Appl. Catal. A Gen.* **1997**, *161* (1), 59–78.

(6) Braconnier, L.; Landrivon, E.; Clémençon, I.; Legens, C.; Diehl, F.; Schuurman, Y. *Catal. Today* **2013**, *215*, 18–23.

(7) de la Peña O'Shea, V. A.; Homs, N.; Fierro, J. L. G.; Ramírez de la Piscina, P. *Catal. Today* **2006**, *114* (4), 422–427.

(8) de la Peña O'Shea, V. A.; Campos-Martín, J. M.; Fierro, J. L. G. *Catal. Commun.* **2004**, *5* (10), 635–638.

(9) Gnanamani, M. K.; Jacobs, G.; Shafer, W. D.; Davis, B. H. *Catal. Today* **2013**, *215*, 13–

17.

(10) Ducreux, O.; Rebours, B.; Lynch, J.; Roy-Auberger, M.; Bazin, D. *Oil Gas Sci. Technol. - Rev. l'IFP* **2009**, *64* (1), 49–62.

(11) Dehghan, R.; Hansen, T. W.; Wagner, J. B.; Holmen, A.; Rytter, E.; Borg, Ø.; Walmsley, J. C. *Catal. Letters* **2011**, *141* (6), 754–761.

(12) Tsakoumis, N. E.; Patanou, E.; Lögdberg, S.; Johnsen, R. E.; Myrstad, R.; van Beek, W.; Rytter, E.; Blekkan, E. A. *ACS Catal.* **2019**, *9* (1), 511–520.

(13) Liu, J. X.; Su, H.-Y.; Sun, D. P.; Zhang, B.-Y.; Li, W. X. *J. Am. Chem. Soc.* **2013**, *135* (44), 16284–16287.

(14) Lancelot, C.; Ordomsky, V. V.; Stéphan, O.; Sadeqzadeh, M.; Karaca, H.; Lacroix, M.; Curulla-Ferré, D.; Luck, F.; Fongarland, P.; Griboval-Constant, A.; Khodakov, A. Y. *ACS Catal.* **2014**, *4* (12), 4510–4515.

(15) Khodakov, A. Y.; Lynch, J.; Bazin, D.; Rebours, B.; Zanier, N.; Moisson, B.; Chaumette, P. *J. Catal.* **1997**, *168* (1), 16–25.

(16) Bulavchenko, O. A.; Cherepanova, S. V.; Malakhov, V. V.; Dovlitova, L. S.; Ishchenko, A. V.; Tsybulya, S. V. *Kinet. Catal.* **2009**, *50* (2), 192–198.

(17) van Steen, E.; Sewell, G. S.; Makhothe, R. a.; Micklethwaite, C.; Manstein, H.; de Lange, M.; O'Connor, C. T. *J. Catal.* **1996**, *229* (162), 220–229.

(18) Boyes, E. D.; Gai, P. L. *Ultramicroscopy* **1997**, *67* (1–4), 219–232.

(19) Gai, P. L.; Boyes, E. D. *Microsc. Res. Tech.* **2009**, *72* (3), 153–164.

(20) Gai, P. L.; Boyes, E. D. *J. Phys. Conf. Ser.* **2010**, *241* (6), 7114–7117.

(21) Zhao, Y.; Feltes, T. E.; Regalbuto, J. R.; Meyer, R. J.; Klie, R. F. *J. Appl. Phys.* **2010**,

108 (6), 063704.

(22) Pearson, D. H.; Ahn, C. C.; Fultz, B. *Phys. Rev. B* **1993**, *47* (14), 8471–8478.

(23) Grunes, L. A.; Leapman, R. D.; Wilker, C. N.; Hoffmann, R.; Kunz, A. B. *Phys. Rev. B* **1982**, *25* (12), 7157–7173.

(24) Suntivich, J.; Hong, W. T.; Lee, Y. L.; Rondinelli, J. M.; Yang, W.; Goodenough, J. B.; Dabrowski, B.; Freeland, J. W.; Shao-Horn, Y. *J. Phys. Chem. C* **2014**, *118* (4), 1856–1863.

(25) Ward, M. R.; Boyes, E. D.; Gai, P. L. *ChemCatChem* **2013**, *5* (9), 2655–2661.

(26) Dembélé, K.; Bahri, M.; Melinte, G.; Hirlimann, C.; Berliet, A.; Maury, S.; Gay, A. S.; Ersen, O. *ChemCatChem* **2018**, *10* (18), 4004–4009.

Chapter 2 : Literature Review

2.1 Cobalt Fischer-Tropsch Synthesis

2.1.1 Fischer-Tropsch Synthesis

The hydrogenation of CO over transition metal catalysts (at 200-350 °C) to form long-chained hydrocarbons has underpinned the petroleum and fine chemicals industry for almost a century.[1] This process is known as Fischer-Tropsch (FT) synthesis. Several transition metals are known to be active for FT synthesis with decreasing activity in the following order: Ru > Fe > Co > Ni.[2,3] Ruthenium is the most active FT catalyst at low temperature (~200 °C) compared to other known FT metal catalysts.[3] However, due to its high cost, it is not economically viable for use in industrial FT synthesis, but it is instead used as a promoter.[4,5] Nickel is rarely used as an FT catalyst due to its high selectivity towards methane production- an undesirable FT synthesis product. As a result, Fe and Co are the two most used industrial FT catalysts.[6]

Cobalt catalysts are preferred over Fe for low-temperature (~220 °C) FT synthesis due to their higher CO conversion.[7] Also, Co catalysts are more resistant to several deactivation mechanisms, and thus have longer reaction lifetime, when compared to iron.[8–10] Hence, Co is considered the most attractive catalyst for low-temperature (200-250 °C) FT synthesis.[8] During Co FT synthesis, the hydrocarbon product formation mechanism occurs through the chemisorption of CO on the reduced metallic Co active site.[11] This is followed by the adsorption and dissociation of H_2 on the metallic Co surface, which subsequently reacts with the chemisorbed CO through nucleophilic addition. Finally, the hydrocarbon chain grows by the condensation of H_2O and the insertion of additional H_2 and CO molecules in a

condensation-addition polymerisation catalytic cycle. For a detailed account on the reaction mechanisms of FT synthesis, the reader is encouraged to see works by B.H. Davis.[11]

2.2 Activation of Cobalt Fischer-Tropsch Catalysts

Cobalt is rarely available naturally in a metallic state for industrial FT synthesis due to its rapid air oxidisation.[8,12] Consequently, the production of catalytically active metallic Co is achieved by reduction of supported Co_3O_4 in a sealed catalytic reactor before introducing syngas (a mixture of CO and H_2) for FT synthesis.[7] This process is referred to as catalyst activation. Catalyst activation is a crucial step in FT catalysis as it facilitates the evolution of the active sites on the final reduced Co catalyst.[13,14] Occasionally, depending on the reaction temperature, the composition of the reducing atmosphere, catalyst support, particle size, and catalyst promoter, Co_3O_4 does not entirely reduce to active metallic Co[15] resulting in a catalyst with mixed Co valence states and crystallographic phases which could impact CO conversion and product distribution during FT synthesis.[15]

2.2.1 Reducing Gas Composition

The effect of reducing gas composition on the reduction of Co_3O_4 and its subsequent effect on the FT synthesis has been extensively studied.[14,16–19] Two types of reducing gas atmospheres have been explored: H_2 and CO & H_2, either as a syngas mixture or sequential CO & H_2 treatment.

Hydrogen

The reduction of Co_3O_4 in H_2 is the most extensively studied Co catalyst activation method for FT synthesis since H_2 is an excellent gaseous reducing agent and the byproduct of the reaction is the non-toxic water vapour (eq. 2.1).[8] Thermodynamically, the reduction of Co_3O_4 to metallic Co (eq. 2.1) is a very endergonic reaction (ΔG^0_{298}= 802.26 kJ.mol^{-1}).[20–22] Temperature-programmed reduction (TPR) studies of Co_3O_4 have shown that the reduction of Co_3O_4 to metallic Co in H_2 is a two-step process: conversion of Co_3O_4 to CoO at 250-350 °C (eq. 2.2), followed by conversion of CoO to Co at 500-600 °C (eq. 2.3).[23]

$$Co_3O_4(s) + 4H_2(g) \leftrightarrow 3Co(s) + 4H_2O(g) \qquad (\Delta G^0_{298}\ 802.26\ \text{kJ.mol}^{-1}) \qquad (2.1)$$

$$Co_3O_4(s) + H_2(g) \leftrightarrow 3CoO(s) + H_2O(g) \qquad (\Delta G^0_{298}\ 150.69\ \text{kJ.mol}^{-1}) \qquad (2.2)$$

$$3CoO(s) + 3H_2(g) \leftrightarrow 3Co(s) + 3H_2O(g) \qquad (\Delta G^0_{298}\ 651.57\ \text{kJ.mol}^{-1}) \qquad (2.3)$$

Ernst *et al.*[24] have investigated the reducibility of Co_3O_4 in H_2 at 270, 370, and 500 °C. They showed that the presence of Co_3O_4 and CoO was observed on the reduced catalyst, without metallic Co, at 270 °C. Increasing the reduction temperature to 370 °C resulted in a mixture of metallic Co, Co_3O_4 and CoO, and at 500 °C, 82% metallic Co and 18% CoO were formed. Similarly, Khodakov *et al.*[15] reported the presence of Co_3O_4, CoO and Co on the H_2 reduced catalyst at 300 °C. These results are consistent with a reported TPR profile[23] and the thermodynamics of the reactions. However, these findings suggest that under industrially relevant Co FT catalyst activation temperatures (~350 °C)[8], H_2 gas does not entirely reduce Co_3O_4 to active metallic Co, resulting in a catalyst with mixed Co valence states. This renders the H_2 activation method ineffective for industrial FT catalysis since a catalyst with a high

surface density of metallic Co atoms is required for high activity in FT synthesis. Therefore, to obtain high metallic Co surface density under H_2 reduction, the temperature needs to be increased to 600 °C (or higher) to enhance the conversion of CoO to metallic Co (e.q. 2.3).[23] However, high reduction temperatures are seldomly used due to severe particle sintering and consequent loss of catalytic activity.[25] Overall, industrial activation of Co FT catalyst in H_2 requires a trade-off between minimising sintering and maximising reducibility, and for this reason, Co catalyst are typically promoted with hydrogenation catalysts such as Ru to enhance low-temperature Co_3O_4-H_2 reduction.[5]

Syngas

The activation of Co_3O_4 for FT synthesis in syngas (either sequential CO & H_2 treatment or a direct mixture) has been of recent interest due to the promising catalytic performance of a catalyst activated in syngas.[13,14,18,26] The sequential treatment procedure typically occurs in a two-step process: firstly, the formation of cobalt carbide (Co_2C) from the reaction of Co_3O_4 with CO at 230 °C (eq. 2.4 & 2.5); secondly, the formation of metallic Co from the decomposition of the carbide in H_2 at 230 °C as in reaction (eq. 2.6). Importantly, in contrast to H_2 reduction, the activation of Co_3O_4 in the syngas is thermodynamically favoured.

$$Co_3O_4(s) + CO(g) \leftrightarrow 3CoO(s) + CO_2(g) \qquad (\Delta G^0_{298}\ \text{-29.4 kJ.mol}^{-1}) \qquad (2.4)$$

$$2CoO(s) + 4CO(g) \leftrightarrow Co_2C(s) + 3CO_2(g) \qquad (\Delta G^0_{298}\ \text{13.9 kJ.mol}^{-1}) \qquad (2.5)$$

$$Co_2C(s) + 2H_2(g) \leftrightarrow 2Co(s) + CH_4(g) \qquad (\Delta G^0_{298}\ \text{-16 kJ.mol}^{-1}) \qquad (2.6)$$

Direct treatment of Co_3O_4 with a syngas mixture[14,16,26], as opposed to sequential treatment with CO and H_2, respectively, allows simultaneous reactions (eqs. 2.4 –2.6). The relevant reactions, however, include an essential side reaction; the disproportionation of CO to form carbonaceous material (eq. 2.7).

$$2CO(g) \leftrightarrow CO_2(g) + C(s) \qquad (\Delta G^0_{298} \text{ -120.1 kJ.mol}^{-1}) \qquad (2.7)$$

The main advantage of CO disproportionation is the formation of a sinter-resistant catalyst *in-situ*, where catalyst particles are held within carbon fibres during FT synthesis.[27,28] De la Peña O'Shea *et al*.[14] have reported a study of the activation of Co_3O_4 under syngas (CO/H_2=1) which observed the presence of Co together with graphitic carbon. Such a catalyst would be active and stable (resistant to deactivation from sintering) over long hours in the FT catalytic reactor. Fierro *et al*.[16] have reported a five-time increase in CO conversion for a syngas activated catalyst when compared to conventional H_2 activation (Figure 2.1). However, the syngas activated catalyst took *ca.* 15 hrs to reach the highest stable CO conversion level compared to 4 hrs with H_2 activation (Figure 2.1). The deactivation of Co catalyst due to the surface coverage of active sites by carbon encapsulating the nanoparticles may limit catalytic performance.[29] This has been observed to be more severe in the reaction of Co_3O_4 with CO in the absence of H_2 (Figure 2.1). *In-situ* electron microscopy[30] and TPR[29] has shown that the presence of H_2 in syngas drives the methanation of excess carbon formed from CO dissociation and disproportionation. Thus, creating a porous carbon shell through which the Co active sites are accessible during FT synthesis.

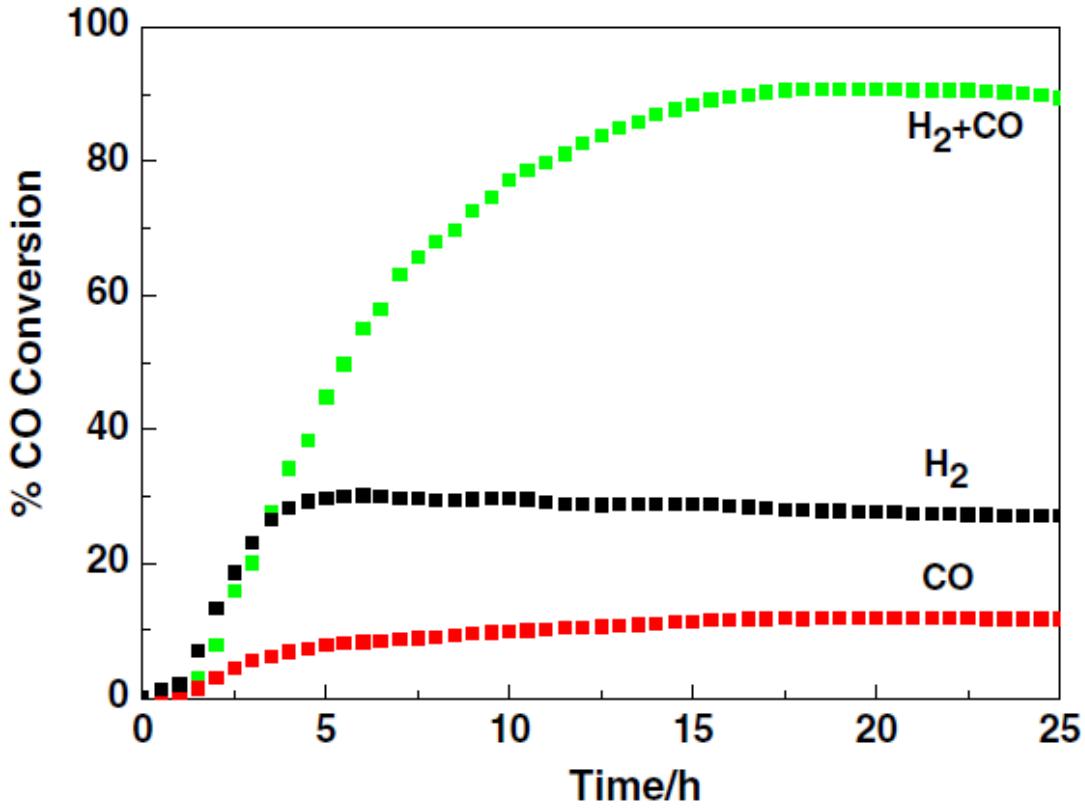

Figure 2.1. Conversion of CO over time for Co catalyst activated in CO, H_2 and H_2+CO (1:1). (Adapted from ref. [16] *© 2004 Elsevier B.V.)*

Numerous experimental studies have shown that the reduction of Co_3O_4 results in the formation of face centred cubic (fcc) and hexagonal close-packed (hcp) metallic Co.[13,15,18,31] Several authors have obtained either mixed[32] or pure[33] Co crystallographic phases from the reduction of Co_3O_4 which has been variously attributed to particle size[33] and temperature.[18] However, the most striking effect is due to the reducing gas.[17] Experimental studies have shown that reduction of Co_3O_4 under syngas ($CO+H_2$) produces hcp Co in contrast to the fcc Co phase produced under H_2 reduction.[17,18] To support this, Density Functional Theory (DFT) calculations suggest that the key is the formation and decomposition of Co_2C in syngas a reaction which is absent for H_2 reduction of Co_3O_4.[34] More specifically, the structural rearrangement of the orthorhombic Co_2C structure into the hcp Co structure during the

decomposition of Co_2C (eq. 2.6) is thermodynamically favoured due to the similarities in the two structures.[34]

The selectivity of hcp over fcc Co crystallographic phases is important as experimental data has shown that an hcp-*predominant* Co catalyst shows a higher CO conversion rate (catalytic activity) compared to fcc-*predominant* Co under equivalent FT synthesis conditions (Figure 2.2).[14,17,18,26] DFT calculations suggest that this difference in catalytic activity arises as hcp Co forms dense atomic active surface sites not found on fcc Co.[35] Additionally, DFT calculations also show that the activation energy for CO dissociation (a rate-limiting step in FT synthesis) is lower on high surface coverage hcp Co (10-11) surface (i.e. 1.21 eV) compared to high surface coverage fcc Co {111} surface (i.e. 2.48 eV).[35] This explains the experimentally observed differences in the rate of CO conversion between hcp and fcc Co (Figure 2.2). However, these DFT calculations are based on bulk Co crystallographic phases and relaxed Wulff models in a vacuum in the absence of catalyst support or surfactants, both of which affect the surface energies and free energy of real nanoparticles. Besides, high-resolution imaging of reduced Co_3O_4 particles have shown that both hcp and fcc Co phases can exist in the same particle.[32]

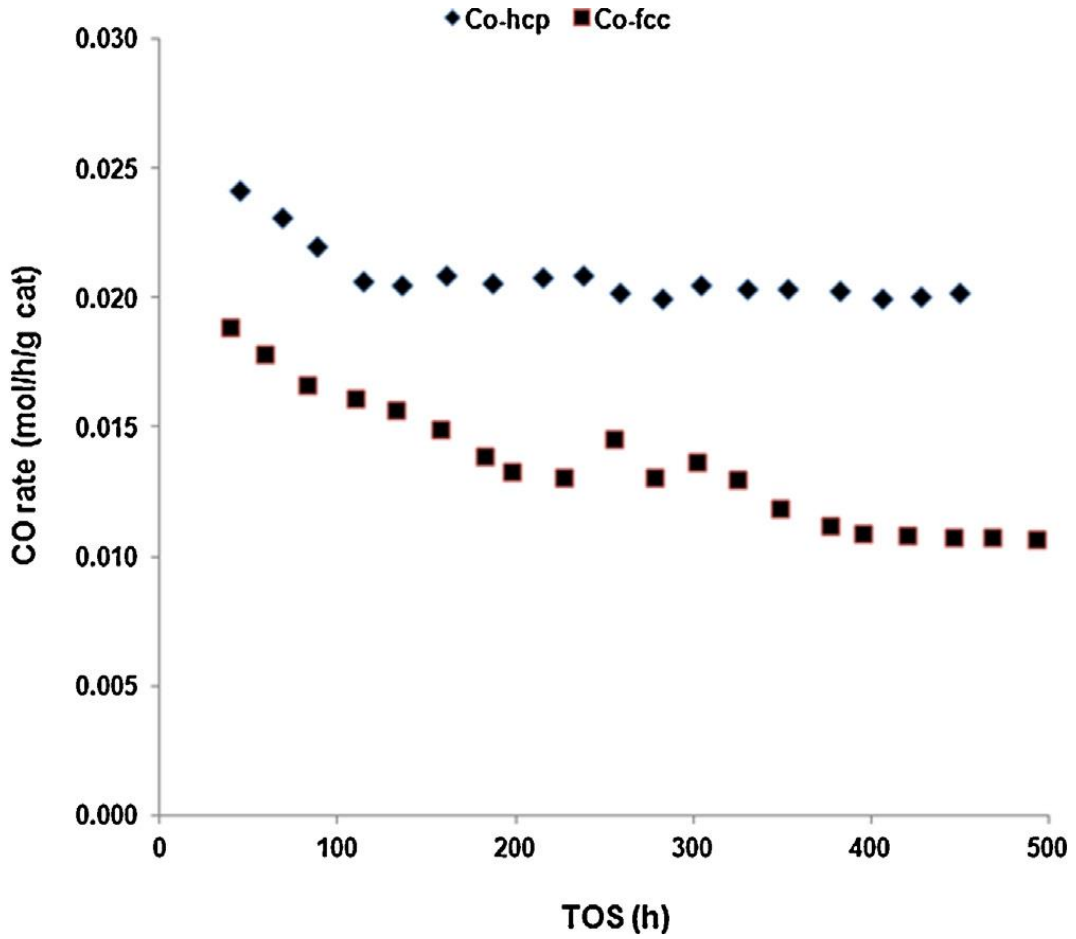

Figure 2.2. CO conversion rate for fcc Co (■) versus hcp Co (♦) as a function of time-on-stream. (Adapted from ref.[17] *© 2013 Elsevier B.V.)*

2.2.2 The Effect of Supports on Cobalt Fischer-Tropsch Catalysts

Cobalt FT catalysts are typically supported on high surface area oxides (such as TiO_2, Al_2O_3, and SiO_2) or porous carbon materials.[8] The interaction between the active metal catalyst and the support has a significant effect on the reducibility and subsequent activity and selectivity of the catalyst.[36,37] This interaction is generally known as metal-support-interaction (MSI). Inorganic oxide supports such as TiO_2, Al_2O_3 and SiO_2, generally have high surface binding energies[37], which can result in the formation of stable Co species (e.g. cobalt silicate) at the

metal-support interface, that can only be reduced at high temperatures.[38] Hence, studies of the effects of catalyst activation method on the physicochemical properties of the active metal catalyst, as in this D.Phil. project, require an inert catalyst support that does not severely affect the properties and the reducibility of the catalyst, such as carbon support. Similar precautions have been adopted before in the study of particle size effects on FT synthesis.[39]

Carbon Supports

Carbon-based materials are attractive catalyst supports due to their chemical inertness, low MSI, and controllable porosity and morphology.[40] Additionally, carbon supports can be chemically modified by the introduction of heteroatoms, such as nitrogen, into the carbon lattice to improve the reducibility of a catalyst.[41] The disadvantage in using modified or unmodified carbon supports for industrial FT synthesis is that, unlike inorganic oxides, they tend to gasify at high temperatures in the presence of H_2 to produce methane.[42] Industrial FT synthesis typically runs for several weeks or months and hence the loss of support through gasification would be significant.

There are several known carbon materials supports with different morphologies including nanotubes (CNTs)[43], nanofibers (CNFs)[39], solid[44] and hollow carbon spheres (HCSs)[45]. HCSs are the most versatile carbon supports, with precisely controllable particle diameter, shell thickness, surface area and porosity.[45] They are typically synthesised by covering a pre-synthesised template with a carbon source using chemical vapour deposition (CVD)[46] or solvothermal reaction[47], followed by the removal of the template using chemical etching or high-temperature annealing. The HCSs' diameter and pore size are determined by the size and porosity of the template. The thickness of the carbon shell is controlled by adjusting the concentration of the carbon source.[46] Templated synthesis of HCSs as supports, therefore,

offers essential flexibility in catalyst design where catalyst particles can either be supported inside or outside the surface of HCSs.[5]

Historically, colloidal silica spheres have been used as templates for the synthesis of HCSs due to their easily controllable size and porosity.[46] However, this method is not environmentally friendly or safe since the removal of the silica template requires a strongly corrosive chemical, hydrofluoric acid (HF). Alternatively, as used in this project, commercial polystyrene (PS) beads provide a convenient, fast, and chemical-free etching step for the templated synthesis of HCSs.[48,49] In the PS templated synthesis of HCSs, the PS template is removed by high-temperature treatment in an inert atmosphere during carbonisation of the carbon source.[49]

2.2.3 The Effect of Particle Size on Cobalt Fischer-Tropsch Catalysts

In the last decade, the influence of the Co particle size distribution on the reducibility, selectivity and activity of FT synthesis has been a growing field of research.[39,50–53] There are several ways to tailor a catalyst of specific particle size, for example, the careful design of the support porosity can offer several advantages in controlling Co particle size, dispersion, and reducibility. For example, Saib *et al.*[54] reported on the influence of the average pore size diameter (20, 40, 60, 100, and 150 Å) of silica on the physicochemical properties of silica supported Co FT catalysts. The authors found that the Co particle size increased with the pore diameter of the silica support. However, care should be taken when correlating the particle size to the reducibility of the catalyst, as this depends on the support. As discussed in section 2.2.2 above, inorganic oxide supports have strong MSI which can result in the formation of stable Co species (e.g. cobalt silicate) at the metal-support interface, that can only be reduced at high

temperatures compared to inert carbon supports. As a result, the reducibility of cobalt oxide on inorganic support generally decreases with decreasing particle size (generally < 60 Å).[15,54] In contrast, the reducibility of cobalt oxide on inert carbon supports increases with decreasing particle size.[39,51]

Breejen *et al*.[39] reported on the effect of the average cobalt particle size (20.6 – 160 Å) on FT synthesis using an inert carbon support. From this study, it was found that the turnover frequency (TOF) (i.e. the rate of conversion of reactants to products, per gram of catalyst, per hour) decreased with particle sizes below 60 Å. The authors also found that the particles below 60 Å were more selective towards CH_4 formation– an undesirable FT synthesis product.[39] In agreement, Bezemer *et al*.[51] also found that the rate of CO hydrogenation decreased for particle sizes below 60 Å.[51] In addition, the catalytic activity increased exponentially with the increase in particle size up to 60 Å in diameter, and then decreased exponentially for particles bigger than 65 Å.[51]

For inorganic oxide supports, Borg *et al*.[50] reported on the effects of cobalt particle size supported over alumina on the product distribution of the FT synthesis. Authors found that the C_{5+} selectivity increased exponentially with increase in Co particle size up to about 70-80 Å and became constant for particles > 90 Å, while CH_4 and C_{2-4} selectivity was at a minimum at particle sizes between 7-8 nm; leading to the conclusion that the optimum Co particle size for a good FT synthesis product distribution and activity was around this order.[50] This is generally agreed upon amongst most authors.[53–5556] It is therefore essential and warranted that for this D.Phil. research, a catalyst system of an optimum particle size (~ 60-65 Å) for an inert support is selected for activation studies without the influence of the support on the reducibility of the catalyst. However, this thesis will not explore the effects of particle size, since it has been well studied, and well understood[39,51]

2.3 Characterisation of Cobalt Fischer-Tropsch Catalysts

Cobalt FT catalysts have been routinely characterised using bulk X-ray based and temperature-programmed redox methods.[8] These techniques are useful in determining the bulk crystallographic phases in the reduced catalyst and the Co_3O_4 reduction temperature profile.[5] However, catalytic reactions are surface-active processes that depend on the atomic structure of the active surfaces of the catalyst.[57] Thus, bulk techniques such as XRD lack the necessary spatial resolution (~1 μm) to probe the surface structure of the catalysts.[58] Alternatively, aberration-corrected (scanning) transmission electron microscopy (AC-(S)TEM) can probe various properties of materials under different environments with a high spatial resolution (~50-80 pm). [59] Thus, it can provide an understanding of the relationship between the surface structure and chemistry (spectroscopy) of materials on a local scale.

2.3.1 Electron Microscopy of Cobalt Fischer-Tropsch Catalysts

Co_3O_4 Precursor

Precursor Co_3O_4 undergoes changes in Co oxidation state, particle size and morphology during the activation process, as described in section 2.2. It is therefore essential to characterise the as-prepared Co_3O_4 before reduction to understand the post-activation changes. Co_3O_4 has a *normal*-spinel crystal structure comprising of an oxygen fcc sub-lattice, and Co^{2+} and Co^{3+}

cations occupying respectively one-eighth of the tetrahedral interstitial sites and half of the octahedral sites per unit cell.[60] The spinel structure offers multiple possible surface terminations depending on the exposed surfaces and the overall shape of the crystal. The atomic arrangement of the Co_3O_4 surface terminations is critical to the activation of the Co catalyst as it may or not facilitate the adsorption of reducing gas (CO or H_2) molecules, thus affecting the surface reactivity of the as-prepared Co_3O_4. Importantly, DFT studies indicate that CO molecules in syngas preferentially adsorb on surfaces with a high concentration of Co^{3+}, while H_2 is preferentially adsorbed on surfaces with Co–O bridge sites.[61,62] Additionally, DFT calculations also indicate that the presence of surface lattice O makes a significant contribution to lowering the adsorption energy of CO on the active sites of Co_3O_4, improving the reactivity of Co_3O_4.[63]

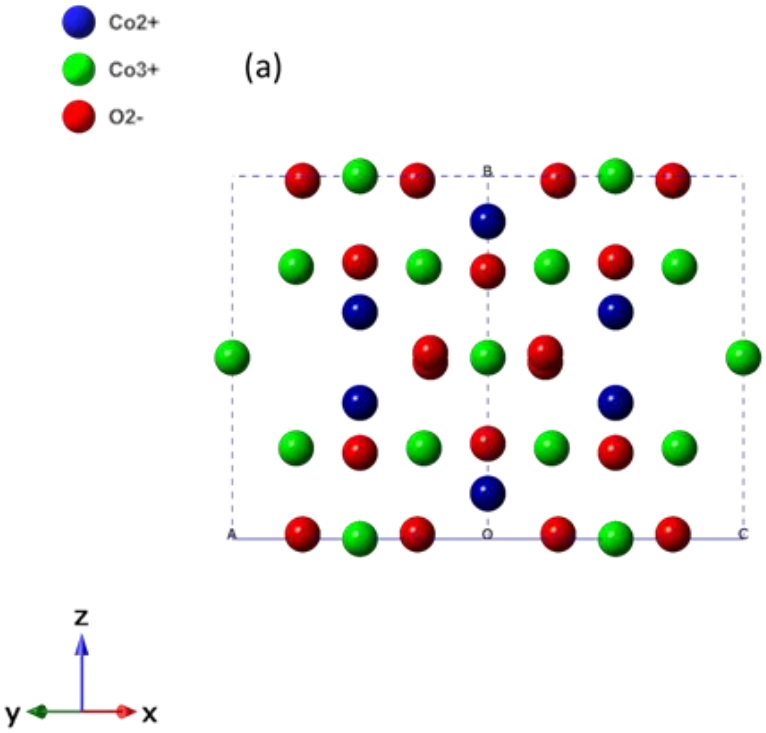

Figure 2.3. Atomic model of Co_3O_4 unit cell viewed along a <110> projection.

There are numerous reports on different morphologies of Co_3O_4 due to its extensive use as a multifunctional catalyst in many reactions other than FT.[64] Electron microscopy (EM) has been frequently used to determine the surface structure of nanoparticles, providing insight into the potential reactivity at different surfaces of metal catalysts.[57] For example, Xie *et al*.[65] reported a facet-dependent reactivity of Co_3O_4 nanorods for low-temperature CO oxidation. This is relevant to this D.Phil. because CO adsorption and dissociation in CO oxidation reactions occur in a similar way to syngas reaction with Co_3O_4. In their work, the authors argue that the {011} planes of the nanorods are more reactive than {111} planes due to the presence of Co^{3+} on the former.[65] However, this conclusion may be limited when drawn simply from the type of facet observed from low-resolution images in which the atomic surface terminations are not resolved. For example, DFT studies have shown that the atomic structure of {111} surfaces results in six possible terminations, some of which have Co^{3+} present.[66,67] Similarly, {011} surfaces can have two possible terminations, one of which has Co^{2+}.[66] Specific synthesis procedures using different surfactants can expose and stabilise one or more of these surface terminations under the right conditions.[65] Thus, atomically resolved characterisation of these surface terminations is necessary to fully understand the reactivity of the as-prepared Co_3O_4 surfaces towards reducing gases.

Yu *et al*.[60] have characterised the atomic structure and surface termination of a {111} surface of Co_3O_4 nanocubes (Figure 2.4), showing clearly resolved O and Co atomic columns. In this work, the {111} surface was found to be terminated by tetrahedral Co ions.[60] According to DFT calculations, this is the most energetically favoured termination among six possible surface terminations of the {111} surface.[67] However, it has also been theoretically shown that tetrahedral Co ions are the least reactive towards CO dissociation, but are more active towards H_2 dissociation.[61] Overall, there are still insufficient studies of the atomic surface terminations

of Co_3O_4 nanoparticles, which holds the key to understanding the reactivity of differently faceted Co_3O_4 nanoparticles towards different catalyst activation environments.

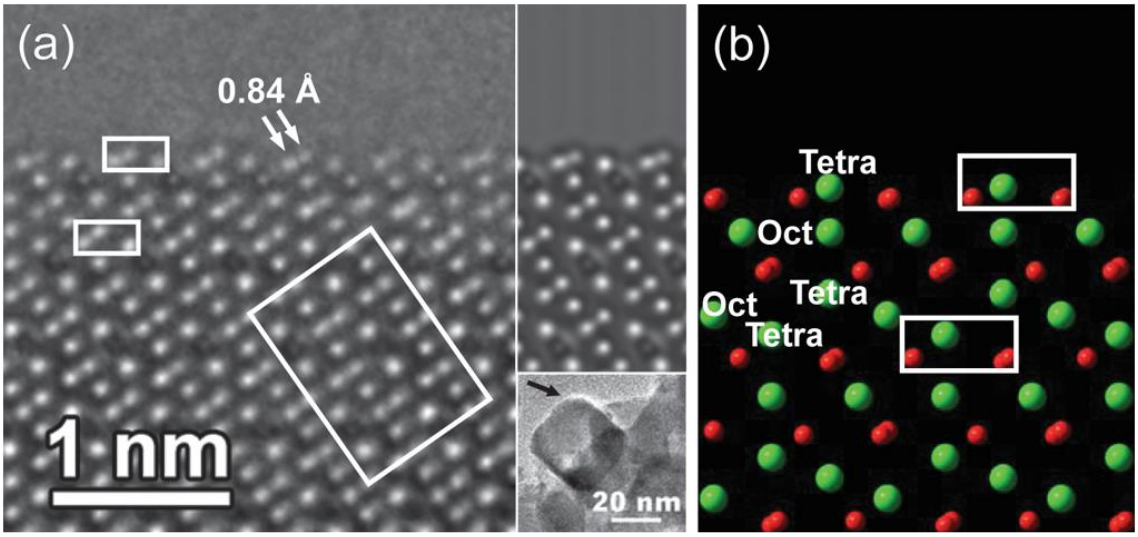

Figure 2.4. (a) AC-TEM image of a {111} surface of Co_3O_4 viewed along a <110> direction. A simulated image of the atomic model is shown as an insert in (a). The bottom-right inset shows an image of the particle at low magnification. (b) Atomic model of the {111} surface of Co_3O_4. The green and red spheres represent Co and O atoms, respectively. (Adapted from ref. [60] *© 2010 The American Physical Society.)*

Electron Microscopy Studies of the Reduction of Co_3O_4

***Ex-situ* Electron Microscopy**

Electron microscopy (EM) has been used *ex-situ* as an ancillary characterisation technique post-reduction of different catalytic systems (e.g. different promoters) using Co_3O_4 for FT synthesis.[68] Specifically, *ex-situ* EM has been used to determine average particle morphology and size, Co oxidation state, chemical composition, and the *local* atomic structure of the reduced Co_3O_4.[32,68,69] However, accurate quantitative *ex-situ* EM characterisation is challenging due to the rapid reoxidation of Co nanoparticles in air.[69] It has been shown that

reoxidation of Co nanoparticles results in the formation of an oxide layer which increases the average particle size and changes the chemical composition and Co oxidation state at the surface relative to the bulk.[32,70,71] In addition, Weststrate *et al*.[69] showed that extensive Co reoxidation changes the particle morphology by the transformation of Co nanoparticles into hollow cobalt oxide particles through Kirkendall effect[72]. In an attempt to circumvent this, the reduced Co FT catalyst particles were passivated (i.e. intentionally exposed to a controlled flow of oxygen) to form a thin (2-4 nm) oxide layer.[69]

Oxygen passivation protects the bulk of nanoparticles from further oxidation in air, thus preserving the pristine properties in the core of the reduced Co nanoparticle. For example, du Plessis *et al*.[32] characterised the core atomic structure of the H_2 reduced and O passivated Co nanoparticles. In this study, the authors showed evidence of a stacking sequence between fcc and hcp Co on the same nanoparticle reduced in H_2 (Figure 2.5), in contrast to an earlier XRD study[17] which showed, exclusively, fcc Co on H_2 reduced nanoparticles. However, although O passivation is useful in protecting the bulk physicochemical properties of Co nanoparticles, the oxide layer destroys the pristine active Co surfaces, which provide crucial pieces of information (e.g. facet termination) pertinent to catalysis. Hence, there is a clear need for *in-situ* EM techniques in which the reduction of Co_3O_4 can be studied without the influence of air or the need for O passivation.

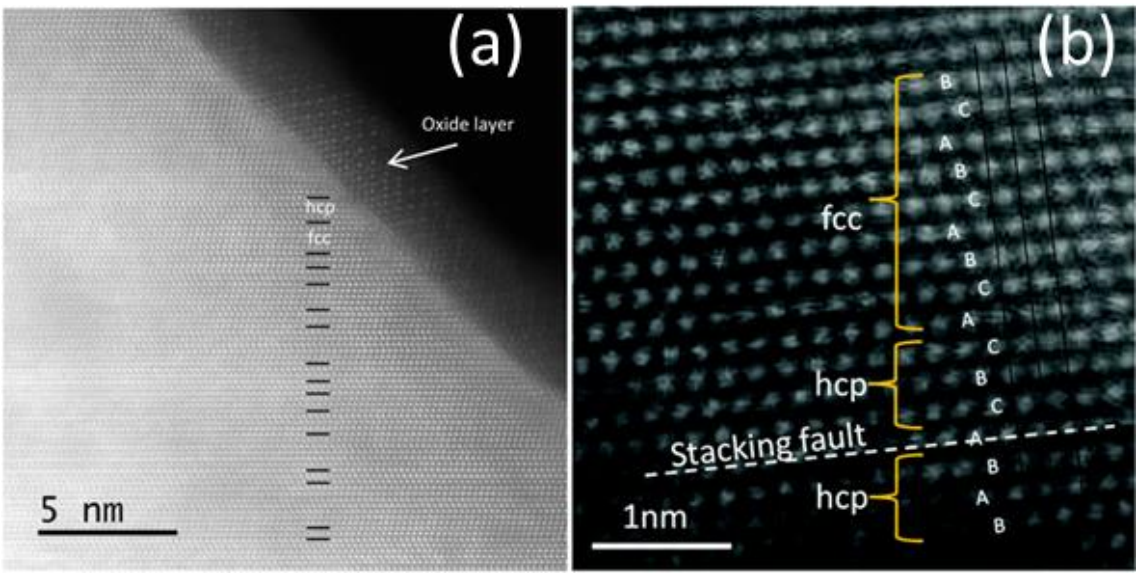

Figure 2.5. (a) High-resolution STEM-HAADF image of H_2 reduced Co FT catalyst. (b) STEM-HAADF image with fcc and hcp Co atomic stacking sequences. (Adapted from ref. [32] *© 2016 Royal Society of Chemistry.)*

In-situ Electron Microscopy

The activation of Co FT catalysts typically takes place at elevated temperatures where gas-solid interactions play a vital role in the evolution of active sites.[73] In addition to circumventing reoxidation of Co, EM studies of catalyst reduction under controlled atmospheres allow the visualisation of structural and chemical dynamics during these gas-solid interactions.[74] Dehghan *et al*.[19] have reported *in-situ* EM reduction of Co_3O_4 at 360 °C under a H_2 atmosphere. A mixture of fcc and hcp Co was obtained, with the smaller (7-20 nm) particles being primarily fcc, and the larger (20-30 nm) particles having mixed fcc and hcp Co phases.[19] However, the underlying relationship between Co particle size and crystallography is still not well understood. The authors found no transitional CoO during the reduction of Co_3O_4 at 360 °C.[19] This observation is not consistent with published reduction profiles and *in-situ* XRD studies of Co_3O_4 in H_2 at this temperature .[5,31] I*n-situ* EM results by Gai *et al.*[75] showed that the reduction of Co_3O_4 nanoparticles in H_2 does not always lead to a complete and direct reduction to metallic

Co (Figure 2.6). In this work, in contrast to a previous report[19], transitional CoO was observed at 400 °C during the *in-situ* EM reduction of Co_3O_4 in H_2 (Figure 2.6).[75] This observation is consistent with similar findings from *in-situ* XRD studies.[5,31]

The reduction of Co_3O_4 to metallic Co through transitional CoO has also been studied by monitoring the changes in Co valence state using *in-situ* Electron Energy Loss Spectroscopy (EELS).[76–80] The Co oxidation state can be estimated from the Co L_3/L_2 peak ratio, the energy loss separation between the Co $L_{3,2}$ edges, and the onset of the Co L_3 edge in the Co EELS fine structure.[81] Using this approach, Zhao *et al*.[78,79] have reported *in-situ* EELS studies of Co FT catalysts. It was found that as the temperature increased to 450 °C, the Co L_3/L_2 ratio and Co L_3-L_2 energy separation increased and the Co L_3 edge energy onset decreased with decreasing Co valence state.[78,79] However, in these reports the precursor Co_3O_4 is pre-reduced in H_2 at 450 °C for 10 hrs, and subsequently transferred to the microscope where it is further heated *in-situ* in the absence of gas. Thus interpreting this *in-situ* EELS study is complicated since the catalyst undergoes *ex-situ* H_2 reduction and *in-situ* reduction by thermal decomposition.

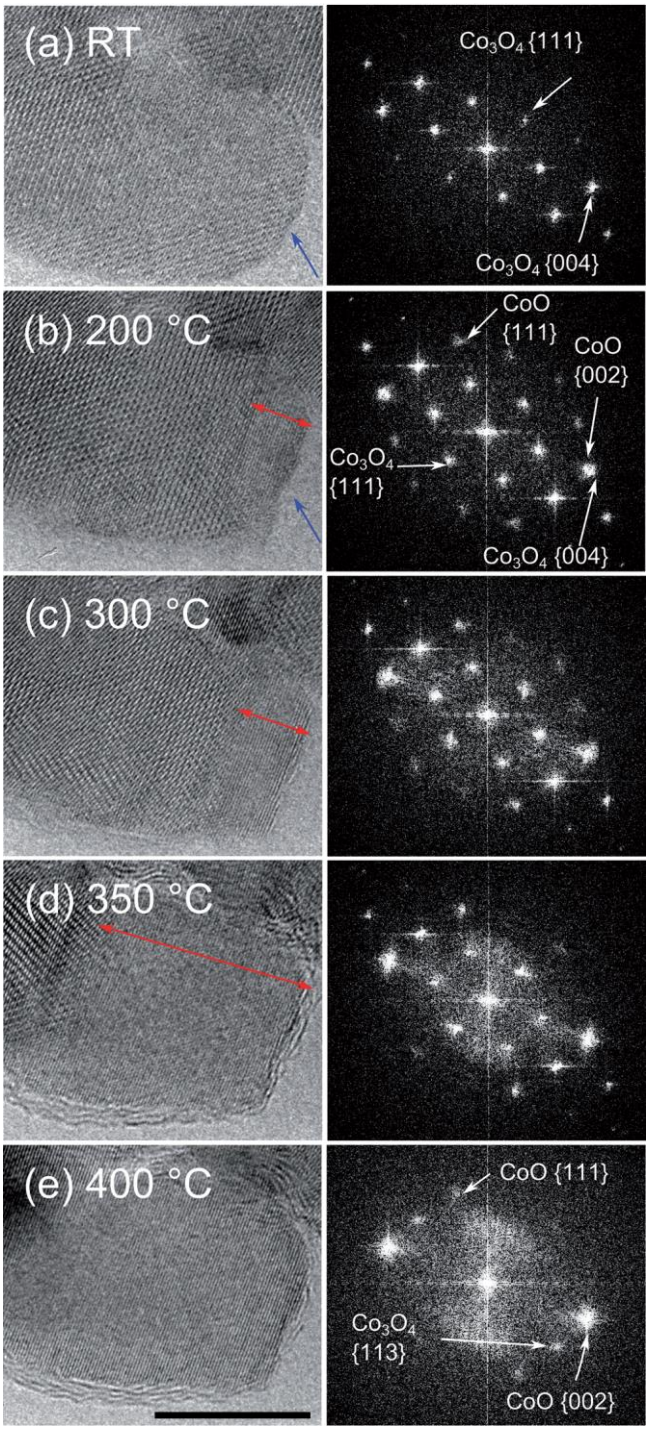

Figure 2.6. High-resolution TEM images and corresponding power spectra of the in-situ reduction of Co_3O_4 as a function of temperature. Scale bar is 10 nm. (Adapted from ref. [75] *© 2013 Wiley-VCH Verlag GmbH & Co.)*

Accurate *in-situ* EM studies of the activation of Co FT catalysts provide an experiment where the changes in the physical and chemical properties of the same catalyst particle can be

simultaneously analysed by imaging and spectroscopy, respectively, and correlated with the reduction conditions. For example, Xin *et al.*[76] observed that *in-situ* reduction of a Co FT catalyst in H_2 gas was accompanied by a change in the porosity of the catalyst particles. Specifically, increased coarsening of the catalyst particles was simultaneously observed with changes in the Co EELS fine structure which indicated a decrease in the Co valence state, when the temperature was increased from 300 to 600 °C in H_2. For this catalyst system, the authors noted that the optimum reduction temperature in H_2 was between 390-440 °C, despite achieving complete reduction at 600 °C during *in-situ* EM reduction. This choice was explained as a requirement to balance the maximum extent of reduction with minimum particle sintering since a significant (100%) size increase was observed beyond 450 °C.[76] This represents a common practice in FT catalyst activation to prioritise minimal sintering over the higher degree of reduction as sintering is one of the primary sources of catalyst deactivation during FT synthesis.[25]

In the last three years, there have been reports on the reactivity of metallic Co nanoparticles under syngas at elevated temperatures using *in-situ* EM.[30,82] Although these reports are focused on FT synthesis and not necessarily on catalyst activation, they provide critical insights into one of the side reactions which occurs in both the catalyst activation and the FT synthesis; the Bourduard reaction (eq. 2.7). This reaction defines the disproportionation of the CO present in syngas, which leads to the formation of carbon materials and subsequent encapsulation of the catalyst particles by carbonaceous materials. Dembélé *et al.*[30] have shown that the presence of H_2 in syngas helps to minimise and regulate the amount of carbon fibre growth through gaseous hydrocarbon formation and also leads to the decomposition of cobalt carbide at high temperatures.

In general, the current literature on *in-situ* EM of Co FT catalysts has focused on the activation of Co FT catalysts in H_2 at various temperatures, mainly because H_2 activation is older and

better studied.[15,23,76–80] In these reports, the activation process is studied using either EELS[76–80], high-resolution (S)TEM imaging[75] or both[76]; where the changes in Co valence state or morphology/atomic structure are followed as a function of reduction conditions under H_2, as discussed above. However, as discussed in Chapter 2, section 2.2, the Co FT catalysts activated in syngas have been reported to have a higher catalytic performance compared to H_2. Yet, to date, there is no literature on the activation of Co FT catalysts in syngas using *in-situ* EM or the comparison of the effect of activation gas composition between syngas and H_2 using *in-situ* EELS in conjunction with high-resolution (S)TEM ADF; making this D.Phil. thesis one of the most significant contributions to the field.

2.4 References

(1) Fischer, F.; Tropsch, H. *Berichte der Dtsch. Chem. Gesellschaft (A B Ser.* **1926**, *59* (4), 830–831.

(2) Vannice, M. *J. Catal.* **1975**, *37* (3), 449–461.

(3) Dry, M. E. In *Studies in Surface Science and Catalysis*; Elsevier Inc., 2004; Vol. 152, pp 533–600.

(4) Iglesia, E. *J. Catal.* **1993**, *143* (2), 345–368.

(5) Phaahlamohlaka, T. N.; Kumi, D. O.; Dlamini, M. W.; Forbes, R.; Jewell, L. L.; Billing, D. G.; Coville, N. J. *ACS Catal.* **2016**, acscatal.6b03102.

(6) Dry, M. E. *Catal. Today* **2002**, *71* (3), 227–241.

(7) Iglesia, E. *Appl. Catal. A Gen.* **1997**, *161* (1), 59–78.

(8) Khodakov, A. Y.; Chu, W.; Fongarland, P. *Chem. Rev.* **2007**, *107* (5), 1692–1744.

(9) Espinoza, R. L.; Steynberg, A. P.; Jager, B.; Vosloo, A. C. *Appl. Catal. A Gen.* **1999**, *186* (1–2), 13–26.

(10) Jager, B.; Espinoza, R. *Catal. Today* **1995**, *23* (1), 17–28.

(11) Davis, B. H. *Fuel Process. Technol.* **2001**, *71* (1–3), 157–166.

(12) Schanke, D.; Hilmen, A. M.; Bergene, E.; Kinnari, K.; Rytter, E.; Ådnanes, E.; Holmen, A. *Energy & Fuels* **1996**, *10* (4), 867–872.

(13) Braconnier, L.; Landrivon, E.; Clémençon, I.; Legens, C.; Diehl, F.; Schuurman, Y. *Catal. Today* **2013**, *215*, 18–23.

(14) de la Peña O'Shea, V. A.; Homs, N.; Fierro, J. L. G.; Ramírez de la Piscina, P. *Catal. Today* **2006**, *114* (4 SPEC. ISS.), 422–427.

(15) Khodakov, A. Y.; Lynch, J.; Bazin, D.; Rebours, B.; Zanier, N.; Moisson, B.; Chaumette, P. *J. Catal.* **1997**, *168* (1), 16–25.

(16) de la Peña O'Shea, V. A.; Campos-Martín, J. M.; Fierro, J. L. G. *Catal. Commun.* **2004**, *5* (10), 635–638.

(17) Gnanamani, M. K.; Jacobs, G.; Shafer, W. D.; Davis, B. H. *Catal. Today* **2013**, *215*, 13–17.

(18) Ducreux, O.; Rebours, B.; Lynch, J.; Roy-Auberger, M.; Bazin, D. *Oil Gas Sci. Technol. - Rev. l'IFP* **2009**, *64* (1), 49–62.

(19) Dehghan, R.; Hansen, T. W.; Wagner, J. B.; Holmen, A.; Rytter, E.; Borg, Ø.; Walmsley, J. C. *Catal. Letters* **2011**, *141* (6), 754–761.

(20) Mayer, N. A. A.; Cupid, D. M. M.; Adam, R.; Reif, A.; Rafaja, D.; Seifert, H. J. J. *Thermochim. Acta* **2017**, *652*, 109–118.

(21) Chase, M. W.; Curnutt, J. L.; Downey, J. R.; Mcdonald, R. A.; Syverud, A. N.; Valenzuela, E. A. *J. Phys. Chem. Ref. Data* **1982**, *11* (3), 695–940.

(22) Pankratz, L. B.; L. B. Pankratz. *Thermodynamic properties of elements and oxides*; Washington D.C., 1982.

(23) Paryjczak, T.; Rynkowski, J.; Karski, S. *J. Chromatogr. A* **1980**, *188* (1), 254–256.

(24) Ernst, B.; Bensaddik, A.; Hilaire, L.; Chaumette, P.; Kiennemann, A. *Catal. Today* **1998**, *39* (4), 329–341.

(25) Tsakoumis, N. E.; Rønning, M.; Borg, Ø.; Rytter, E.; Holmen, A. *Catal. Today* **2010**, *154* (3–4), 162–182.

(26) Tsakoumis, N. E.; Patanou, E.; Lögdberg, S.; Johnsen, R. E.; Myrstad, R.; van Beek, W.; Rytter, E.; Blekkan, E. A. *ACS Catal.* **2019**, *9* (1), 511–520.

(27) Phaahlamohlaka, T. N.; Dlamini, M. W.; Mogodi, M. W.; Kumi, D. O.; Jewell, L. L.; Billing, D. G.; Coville, N. J. *Appl. Catal. A Gen.* **2018**, *552*, 129–137.

(28) Aydin, C.; Lu, J.; Browning, N. D.; Gates, B. C. *Angew. Chemie* **2012**, *124* (24), 6031–6036.

(29) Moodley, D. J.; van de Loosdrecht, J.; Saib, A. M.; Overett, M. J.; Datye, A. K.; Niemantsverdriet, J. W. *Appl. Catal. A Gen.* **2009**, *354* (1–2), 102–110.

(30) Dembélé, K.; Bahri, M.; Melinte, G.; Hirlimann, C.; Berliet, A.; Maury, S.; Gay, A.-S.; Ersen, O. *ChemCatChem* **2018**, *10* (18), 4004–4009.

(31) Paterson, J.; Peacock, M.; Purves, R.; Ferguson, E.; Ojeda, M. *ChemCatChem* **2017**.

(32) du Plessis, H. E.; de Villiers, J. P. R.; Tuling, A.; Olivier, E. J. *Phys. Chem. Chem. Phys.* **2016**, *18* (43), 30183–30188.

(33) Fischer, N.; Van Steen, E.; Claeys, M. In *Catalysis Today*; Elsevier, 2011; Vol. 171, pp 174–179.

(34) Zhao, Y. H.; Su, H. Y.; Sun, K.; Liu, J.; Li, W. X. *Surf. Sci.* **2012**, *606* (5–6), 598–604.

(35) Liu, J.-X.; Su, H.-Y.; Sun, D.-P.; Zhang, B.-Y.; Li, W.-X. *J. Am. Chem. Soc.* **2013**, *135* (44), 16284–16287.

(36) Bernal, S.; Calvino, J. J.; Cauqui, M. A.; Gatica, J. M.; López Cartes, C.; Pérez Omil, J. A.; Pintado, J. M. *Catal. Today* **2003**, *77* (4), 385–406.

(37) Tauster, S. J.; Fung, S. C.; Baker, R. T. K.; Horsley, J. A. *Science (80-.).* **1981**, *211* (4487), 1121–1125.

(38) Jacobs, G.; Das, T. K.; Zhang, Y.; Li, J.; Racoillet, G.; Davis, B. H. *Appl. Catal. A Gen.* **2002**, *233*, 263–281.

(39) den Breejen, J. P.; Radstake, P. B.; Bezemer, G. L.; Bitter, J. H.; Frøseth, V.; Holmen, A.; de Jong, K. P. *J. Am. Chem. Soc.* **2009**, *131* (20), 7197–7203.

(40) Xiong, H.; Jewell, L. L.; Coville, N. J. *ACS Catal.* **2015**, *5* (4), 2640–2658.

(41) Yang, Y.; Jia, L.; Hou, B.; Li, D.; Wang, J.; Sun, Y. *ChemCatChem* **2014**, *6* (1), 319–327.

(42) Moreno-Castilla, C.; Carrasco-Marin, F. *J. Chem. Soc. Faraday Trans.* **1995**, *91* (19), 3519.

(43) Tavasoli, A.; Sadagiani, K.; Khorashe, F.; Seifkordi, A. A.; Rohani, A. A.; Nakhaeipour, A. *Fuel Process. Technol.* **2008**, *89* (5), 491–498.

(44) Xiong, H.; Motchelaho, M. A. M.; Moyo, M.; Jewell, L. L.; Coville, N. J. *J. Catal.* **2011**, *278* (1), 26–40.

(45) Li, S.; Pasc, A.; Fierro, V.; Celzard, A. *Journal of Materials Chemistry A*. Royal Society of Chemistry August 17, 2016, pp 12686–12713.

(46) Xia, Y. D.; Mokaya, R. *Adv. Mater.* **2004**, *16* (11), 886–891.

(47) Sawant, S. Y.; Somani, R. S.; Newalkar, B. L.; Choudary, N. V.; Bajaj, H. C. *Mater. Lett.* **2009**, *63* (27), 2339–2342.

(48) Dai, X. Y.; Zhang, X.; Meng, Y. F.; Shen, P. K. *Xinxing Tan Cailiao/New Carbon Mater.* **2011**, *26* (5), 389–395.

(49) Fu, J.; Xu, Q.; Chen, J.; Chen, Z.; Huang, X.; Tang, X. *Chem. Commun. (Camb).* **2010**, *46* (35), 6563–6565.

(50) Borg, Ø.; Dietzel, P. D. C.; Spjelkavik, A. I.; Tveten, E. Z.; Walmsley, J. C.; Diplas, S.; Eri, S.; Holmen, A.; Rytter, E. *J. Catal.* **2008**, *259* (2), 161–164.

(51) Bezemer, G. L.; Bitter, J. H.; Kuipers, H. P. C. E.; Oosterbeek, H.; Holewijn, J. E.; Xu, X.; Kapteijn, F.; Van Diilen, A. J.; De Jong, K. P.; Dillen, a J. Van; Jong, K. P. De. *Am. Chem. Soc.* **2006**, *128* (12), 3956–3964.

(52) Wang, Z.-J.; Skiles, S.; Yang, F.; Yan, Z.; Goodman, D. W. *Catal. Today* **2011**, *181*, 75–81.

(53) Yang, J.; Frøseth, V.; Chen, D.; Holmen, A. *Surf. Sci.* **2016**, *648*, 67–73.

(54) Saib, A. M.; Claeys, M.; van Steen, E. *Catal. Today* **2002**, *71* (3–4), 395–402.

(55) Prieto, G.; Martínez, A.; Concepción, P.; Moreno-Tost, R. *J. Catal.* **2009**, *266* (1), 129–144.

(56) Xiong, H.; Zhang, Y.; Wang, S.; Li, J. *Catal. Commun.* **2005**, *6* (8), 512–516.

(57) Fujita, T.; Guan, P.; McKenna, K.; Lang, X.; Hirata, A.; Zhang, L.; Tokunaga, T.; Arai,

S.; Yamamoto, Y.; Tanaka, N.; Ishikawa, Y.; Asao, N.; Yamamoto, Y.; Erlebacher, J.; Chen, M. *Nat. Mater.* **2012**, *11* (9), 775–780.

(58) Jacobs, G.; Ji, Y.; Davis, B. H.; Cronauer, D.; Kropf, A. J.; Marshall, C. L. *Appl. Catal. A Gen.* **2007**, *333* (2), 177–191.

(59) Gai, P. L.; Boyes, E. D. *J. Phys. Conf. Ser.* **2010**, *241* (6), 012055.

(60) Yu, R.; Hu, L. H.; Cheng, Z. Y.; Li, Y. D.; Ye, H. Q.; Zhu, J. *Phys. Rev. Lett.* **2010**, *105* (22), 226101.

(61) Zhang, Y.-C.; Pan, L.; Lu, J.; Song, J.; Li, Z.; Zhang, X.; Wang, L.; Zou, J.-J. *Appl. Surf. Sci.* **2017**, *401*, 241–247.

(62) Lu, J.; Song, J.; Niu, H.; Pan, L.; Zhang, X.; Wang, L.; Zou, J.-J. *Appl. Surf. Sci.* **2016**, *371*, 61–66.

(63) Jiang, D. E.; Dai, S. *Phys. Chem. Chem. Phys.* **2011**, *13* (3), 978–984.

(64) Xie, X.; Shen, W. *Nanoscale* **2009**, *1* (1), 50–60.

(65) Xie, X.; Li, Y.; Liu, Z. Q.; Haruta, M.; Shen, W. *Nature* **2009**, *458* (7239), 746–749.

(66) Xu, X.-L.; Chen, Z.-H.; Li, Y.; Chen, W.-K.; Li, J.-Q. *Surf. Sci.* **2009**, *603* (4), 653–658.

(67) Montoya, A.; Haynes, B. S. *Chem. Phys. Lett.* **2011**, *502* (1–3), 63–68.

(68) Shannon, M. D.; Lok, C. M.; Casci, J. L. *J. Catal.* **2007**, *249* (1), 41–51.

(69) Weststrate, C. J.; Hauman, M. M.; Moodley, D. J.; Saib, A. M.; Van Steen, E.; Niemantsverdriet, J. W. *Top. Catal.* **2011**, *54* (13–15), 811–816.

(70) Boyen, H.-G.; Kästle, G.; Zürn, K.; Herzog, T.; Weigl, F.; Ziemann, P.; Mayer, O.; Jerome, C.; Möller, M.; Spatz, J. P.; Garnier, M. G.; Oelhafen, P. *Adv. Funct. Mater.* **2003**, *13* (5), 359–364.

(71) Wang, Z.; Bi, H.; Wang, P.; Wang, M.; Liu, Z.; Shen, L.; Liu, X. *Phys. Chem. Chem. Phys.* **2015**, *17* (5), 3796–3801.

(72) Kirkendall; O., E. *Trans. AIME* **1942**, *147*, 104–110.

(73) Gnanamani, M. K.; Jacobs, G.; Keogh, R. A.; Shafer, W. D.; Sparks, D. E.; Hopps, S. D.; Thomas, G. A.; Davis, B. H. *Appl. Catal. A Gen.* **2015**, *499*, 39–46.

(74) Hansen, T. W.; Wagner, J. B. *ACS Catal.* **2014**, *4* (6), 1673–1685.

(75) Ward, M. R.; Boyes, E. D.; Gai, P. L. *ChemCatChem* **2013**, *5* (9), 2655–2661.

(76) Xin, H. L.; Pach, E. A.; Diaz, R. E.; Stach, E. A.; Salmeron, M.; Zheng, H. *ACS Nano* **2012**, *6* (5), 4241–4247.

(77) Wang, Z. L.; Yin, J. S.; Mo, W. D.; Zhang, Z. J. *J. Phys. Chem. B* **1997**, *101* (35), 6793–6798.

(78) Zhao, Y.; Feltes, T. E.; Regalbuto, J. R.; Meyer, R. J.; Klie, R. F. *J. Appl. Phys.* **2010**, *108* (6), 063704.

(79) Zhao, Y.; Feltes, T. E.; Regalbuto, J. R.; Meyer, R. J.; Klie, R. F. *Catal. Letters* **2011**, *141* (5), 641–648.

(80) Wang, Z. L. L.; Yin, J. S. S.; Jiang, Y. D. D. *Micron* **2000**, *31* (5), 571–580.

(81) Pearson, D. H.; Ahn, C. C.; Fultz, B. *Phys. Rev. B* **1993**, *47* (14), 8471–8478.

(82) Bremmer, G. M.; Zacharaki, E.; Sjåstad, A. O.; Navarro, V.; Frenken, J. W. M.; Kooyman, P. J. *Faraday Discuss.* **2017**, *197* (0), 337–351.

Chapter 3 : Theory and Experimental Design

3.1 The Transmission Electron Microscope

The wave properties of electrons (with a wavelength shorter than visible light) provides ways to overcome the resolution limit of optical microscopes.[1,2] The first electron microscope was constructed by Knoll and Ruska in 1931.[3] Developments, and improvements to electron optics and sources have been carried out over several decades leading to modern TEMs capable of atomic resolution (for a review see Hauenau *et al*.[4]). The basic principle of a TEM is that a beam of electrons is transmitted through a specimen wherein different signals can be detected from interactions with the specimen (Figure 3.1).

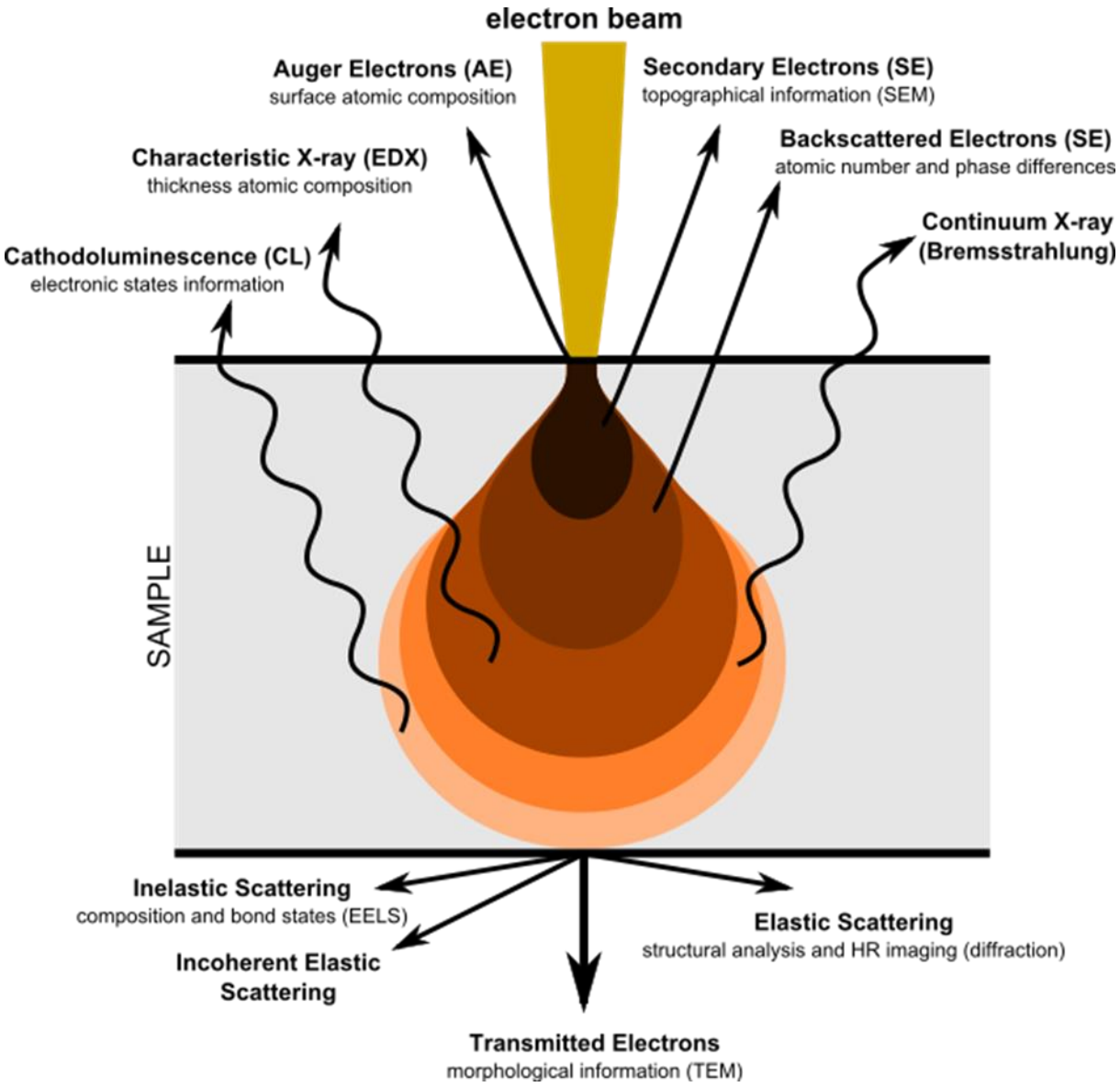

Figure 3.1. Signals generated when electrons interact with a specimen.

3.2 Imaging in the Transmission Electron Microscope

In a conventional Transmission Electron Microscope (TEM), a nearly parallel electron beam illuminates the specimen, and the objective lens focuses the transmitted and scattered electrons

onto the image plane.[5] The image is then magnified and projected onto a viewing screen or more recently onto a 2D detector. Different imaging modes can be selected in TEM using an objective aperture with variable size (Figure 3.2 (a)-(c)). A bright-field (BF) image is formed by selecting the unscattered electrons (Figure 3.2 (a)). A dark-field (DF) image is formed by selecting a specific diffracted beam (Figure 3.2 (b)). Lastly, the high-resolution phase-contrast TEM (HRTEM) images can be formed from the interaction of multiple diffracted beams with themselves and the direct beam (Figure 3.2 (a)).[5] This thesis focuses on the application of high-resolution phase-contrast and focal-series specimen exit wavefunction reconstruction. Hence, the theory of phase-contrast imaging and phase retrieval is briefly summarised. For a more detailed account of imaging theory in HRTEM, the reader is referred to specialist texts.[5–8]

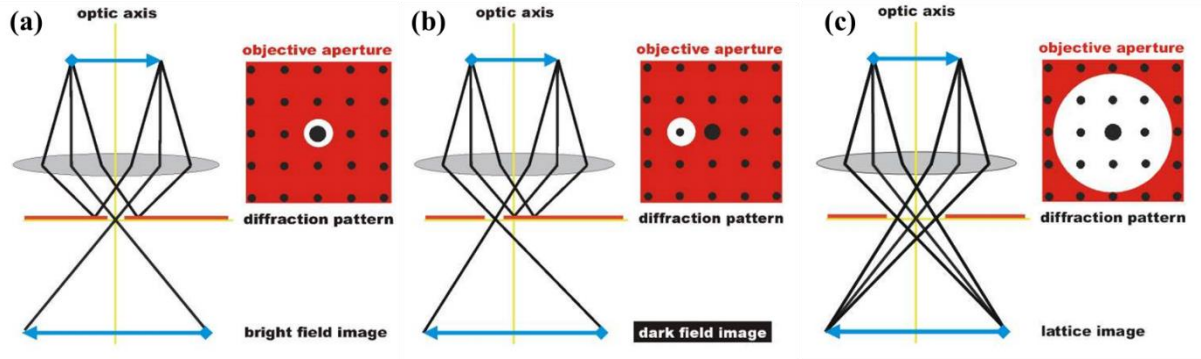

Figure 3.2. Ray diagrams of (a) bright-field imaging, (b) dark-field imaging, and (c) high-resolution phase-contrast imaging.

3.2.1 High-Resolution Imaging

Electron-Specimen Interactions

In high-resolution TEM (HRTEM) imaging, an approximately parallel electron plane wavefunction is transmitted through a specimen, as shown in Figure 3.3. During this process,

the specimen structure information is encoded in the phase and amplitude of the electron wave function at the specimen exit surface.

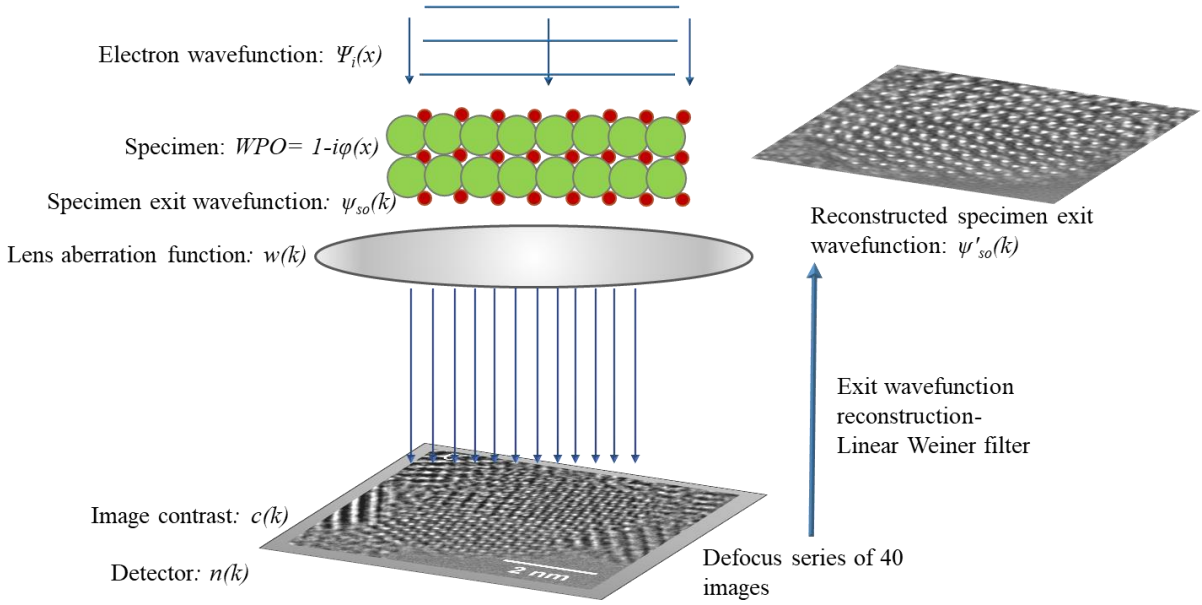

Figure 3.3. Schematic showing the process of high-resolution imaging and exit wavefunction reconstruction from a focal-series of high-resolution phase-contrast images.

The interaction between the incident electron beam and the atoms of the specimen is defined by the projected potential, $\phi(x,y,z)$, where x & y are position vectors in the sample plane, and z denotes the thickness which the electron travels through the specimen. This interaction modifies the phase and the amplitude of the incident electron wavefunction.[9] However, in the simplest case of a thin specimen, neglecting absorption but including multiple scattering, the electron-specimen interaction only alters the phase of the incident electron wavefunction.[7] Under this condition, the specimen is considered a *phase object*, and the specimen exit wavefunction, $\psi_{SO}(x,y)$, can be represented as;

$$\psi_{SO}(x,y) = \exp\{-i\sigma\varphi(x,y)\}, \qquad (3.1)$$

where σ denotes an interaction constant given by;

$$\sigma = 2\pi m_e e \frac{\lambda_r}{h^2}, \tag{3.2}$$

where e is the unit charge of an electron, h is Planck's constant, m_e and λ_r are the relativistically corrected electron mass and wavelength, and φ is the integrated projected potential along the beam direction. Thus, a *phase object* will induce $\sigma\varphi(x,y)$ phase shift on the incident electron wavefunction where φ is given by;

$$\varphi = \int \phi\,(x,y,z)dz, \tag{3.3}$$

For a sufficiently thin specimen consisting of mainly low atomic number elements, such that $|\sigma\varphi(x,y)| \ll 1$, the specimen can be considered as a *weak phase object* (WPO), and the specimen exit wavefunction, ψ_{so}, can be simplified expanding the exponential term in 3.1 and ignoring non-linear terms to[8];

$$\psi_{so}(x,y) \approx 1 - i\sigma\varphi(x,y) \tag{3.4}$$

Image Formation

Subsequently, post-specimen-electron interaction as the electron wave propagates to the image plane; the specimen exit wavefunction is further modified by the limiting objective lens aperture, the phase shifts introduced by the objective lens, and the effects of partial coherence (described later in this chapter).[7,10] Thus, the image wavefunction, $\psi_{si}(k)$, can be considered as a convolution of a point in the specimen with a function $w(k)$.[5,7,10]

$$\psi_{si}(k) = \psi_{so}(k) \otimes w(k) \tag{3.5}$$

The electron beam travels as a complex wave until it reaches the detector, where it is recorded as an image intensity distribution, with the image contrast being a combination of the detector

noise and the aberrated specimen electron wavefunction at the image plane. The recorded image intensity at the image plane is the square of the amplitude of the specimen electron wavefunction. It is by definition, the probability of the electron landing position on the recording device with a loss of phase information.

Contrast transfer, resolution and spherical aberration

In electron wave optics, the Fourier transform (FT) operation is used to relate real and reciprocal space. Here, lower case letters are used to denote functions in real space, while capital letters denote functions in reciprocal space. Taking the FT of eq. (3.5) simplifies the convolution to a product in reciprocal space as;

$$\Psi_{si}(k) = \Psi_{so}(k)W(K) \tag{3.6}$$

where *W(K)* is the FT of the point-spread function. This is generally referred to as the *phase contrast transfer function (PCTF)*, defines the transfer of spatial frequencies in the object exit wavefunction to the image intensity. Ignoring the effects of higher-order aberrations and partial coherence, the PCTF is mainly affected by defocus, Δf, and the coefficient of spherical aberration, C_s. Scherzer[11] defined an optimum defocus value, Δf_s, for which a maximum transfer of a broad bandpass of spatial frequencies, without fluctuation, can be attained (Figure 3.4). (In this definition of the Scherzer focus, the passband in the PCTF contains a local minimum = 0.7. The original definition, Scherzer avoids a local minimum in the passband at the cost of a slightly poorer point resolution $\Delta fs = (C_S\lambda)^{1/2}$).

$$\Delta fs = -1.2\ (C_S\lambda)^{1/2} \tag{3.7}$$

At the Scherzer defous, Δf_s, a broad bandpass of phase-contrast is transferred without phase reversal up to a spatial frequency, k_{max};

$$k_{max} = 1.6\ (C_S\lambda^3)^{-1/4} \tag{3.8}$$

The reciprocal of k_{max} then defines the point resolution (d_1) at the Scherzer defocus as;

$$d_1 = 0.625\ (C_S\lambda^3)^{1/4} \tag{3.9}$$

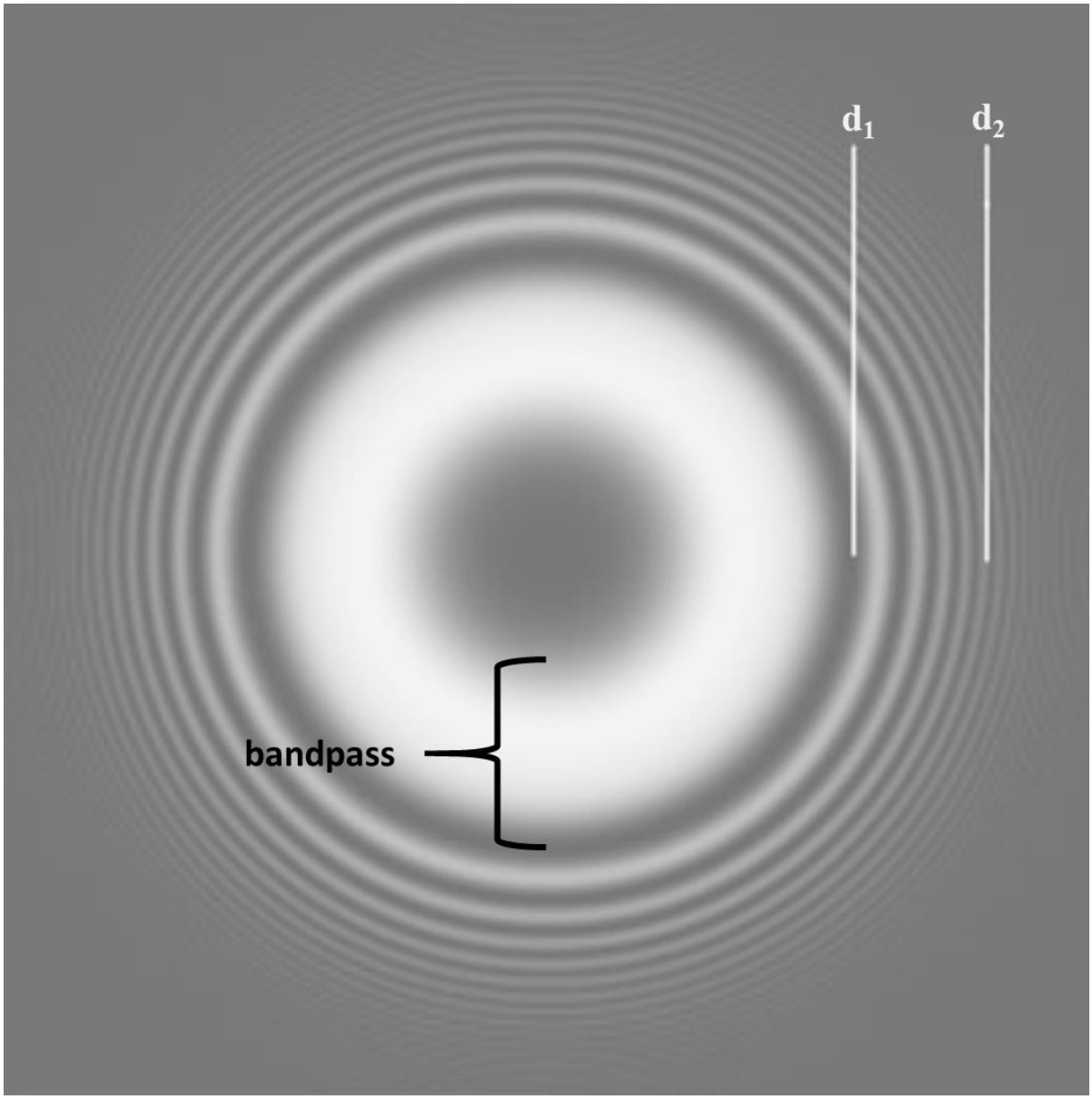

Figure 3.4. A two-dimensional phase-contrast transfer function for a modern 300 kV FEGTEM calculated at the Scherzer defocus (Δf = -34.4 nm, Cs= 0.6mm, ΔE= 0.8 eV, beam divergence= 0.1 mrad). d_1 and d_2, respectively illustrate the interpretable resolution and information limit. The bandpass illustrates the maximum transfer of spatial frequencies without phase reversal. (adapted from ref.[7] © 2019 Springer Nature Switzerland)

Under this condition, the HRTEM image of a thin specimen has a directly interpretable contrast which is proportional to the specimen projected potential, with the highest resolvable spatial frequency limited to d_1 (Figure 3.4). For higher spatial frequencies beyond d_1 (Figure 3.4), the PCTF oscillates. The effect of this is uninterpretable HRTEM images beyond this limit. The highest spatial frequency transferred from the specimen exit wavefunction to the image intensity is defined by the *information limit* of the microscope, d_2 (Figure 3.4). However, for all electron sources used in HRTEM imaging, the illumination is only partially coherent.[8,12] There are two components to this partial coherence: partial *spatial* coherence, due to the finite dimensions of the electron source, and partial *temporal* coherence, which is associated with the finite energy distribution of the source and fluctuations in both the accelerating voltage and the objective lens current.[12,13] The overall effect of this partial coherence of the source is to limit the information that can be extracted from high-resolution images. Thus, the *information limit* of a microscope is determined by the effects of *spatial* and *temporal* coherence in the illumination and by instabilities that act to reduce the transfer of higher spatial frequencies.[14,15]

From eq. (3.9), for a specific microscope, the accelerating voltage (wavelength) and (Sherzer) defocus, the PCTF is mainly affected by spherical aberration, C_s. For HRTEM imaging, the rays scattered by the specimen pass through the objective lens before being focused onto an image. At large distances from the optic axis of the microscope, electrons are prematurely focussed compared to electrons closer to the optic axis. This effect arises from spherical aberration (C_s), and it is mostly responsible for the 'blurring' of the fine details in an uncorrected TEM image, limiting the microscope resolving power.[11] Scherzer proposed a way to overcome C_s by incorporating a corrector for the objective lens consisting of multipole lenses.[16] These multipole lenses generate a negative value of C_s to counteract the finite positive C_s of the round electromagnetic objective lens, thus bringing all rays to focus at one point.[16]

Since then, attempts have been made to improve the theoretical point resolution of a TEM by aberration correction based on a hardware solution originally described by Rose in 1990.[17,18] The first aberration corrector was constructed and incorporated into a 200 kV FEG TEM[19,20], the point resolution improved from 0.24 nm to 0.13 nm. Subsequently, modern aberration-corrected TEM instruments routinely achieve sub 100pm which is sufficient to resolve the projected atomic structure of different materials in various projections.[21,22]

3.3 Focal-Series Exit Wavefunction Reconstruction

High-resolution TEM imaging records the intensity, and the resulting image contrast is sensitive to lens aberrations and defocus; making the quantitative interpretation of high-resolution TEM images problematic. This difficulty in the interpretation of HRTEM images can be overcome by computational reconstruction of the specimen exit wavefunction from a series of images acquired at different defoci.[23–31] There are also other image series acquisition geometries, such as tilt series, where a series of images is acquired with differently tilted illumination settings- this geometry is typically used to obtain resolution beyond the axial limitation of the microscope (i.e. super-resolution).[32,33] However, this thesis will focus only on the focal-series geometry since the aberration-corrected images in the focal-series already contain high-spatial frequency information sufficient to resolve O and Co atoms upon phase retrieval.

In this geometry, the image acquisition alters the PCTF by altering only one aberration - the defocus of the images. All other microscope parameters are typically determined beforehand and kept constant over the image series acquisition. For a specific acceleration voltage, the

limitation on the choice of starting focus, focal step, and the range of the focus values is mainly determined by the coefficient of spherical aberration. The combinations of the spherical aberration and the defoci should be chosen such that all spatial frequencies are strongly transferred by one or more images in the series. The number of images in an image series is no less than three.[34] Although there is no theoretical upper limit, the benefit of using more images to improve the reconstruction quality diminishes quickly, given that the reduction of non-linear image components and Poisson noise follows a square root dependence on the number of images.[35] Therefore, practical reconstructions are rarely performed with more than 64 images, which reduces the non-linear and noise components by a factor of 8. It should also be noted that adding more images also increases the risk of specimen damage; hence a compromise between signal-to-noise and damage is usually sought.

The goal of exit wavefunction reconstruction is to retrieve an estimate of the specimen wavefunction, $\psi'_{so}(k)$ *(Equation 3.10)*, by computational reconstruction at the specimen exit plane by applying a suitable restoring filter, $r_i(k)$, to a series of images at different defoci (i.e. differently aberrated images), thereby eliminating the contribution of the objective lens aberration function (Figure 3.5).[23–31]

$$\psi'_{so}(k) = \sum_i r_i(k) c_i(k) \qquad (3.10)$$

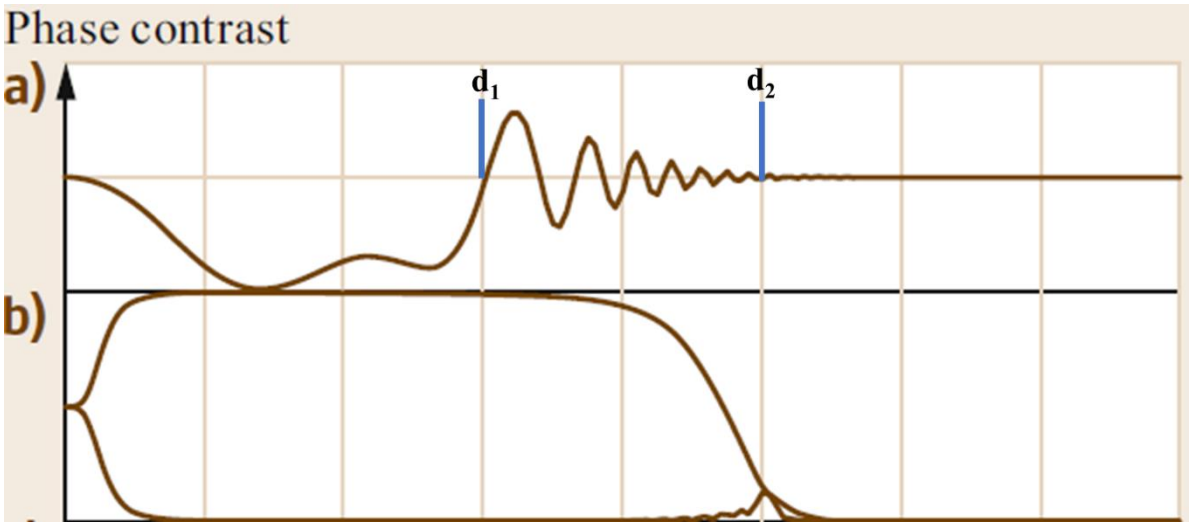

Figure 3.5. A comparison of contrast transfer functions for (a) an HRTEM image at the Scherzer defocus, and (b) a restored specimen exit wavefunction for a 21-member focal series with a defocus step between images of 5 nm. The data are plotted for a 300 kV FEGTEM (300 kV, Cs = 0.57nm, focal spread = 4 nm, beam divergence = 0.1mrad. The CTF in (a) has interpretable information, without contrast reversal, limited to the point resolution (d1). In contrast, the CTF in (b) has interpretable information, without contrast reversal, beyond d1, up to the information limit (d2). (adapted from ref.[7] © 2019 Springer Nature Switzerland).

3.3.1 Electron Dose Fractionation in Focal-Series Exit Wavefunction Reconstruction

It has been shown that the total electron dose used in a focal-series not only affects the signal-to-noise ratio of the restored phase but can also change the specimen during image acquisition due to radiation damage.[36] The electron dose (D) during image acquisition refers to the number of electrons incident on a specimen per unit area ($e/Å^2$). Mathematically, it is expressed by eq. (3.11), where j is the current density ($pA/Å^2$), t is the exposure time (s), and e is the electron charge. The same total electron dose can also cause different degrees of damage to a specimen dependent on the electron dose rate.[37,38] The dose rate can be manipulated by varying the exposure time, t or the beam current, I to give a high flux low exposure time (high dose rate)

or low flux prolonged exposure time (low dose rate), respectively. For a detailed account of electron dose induced damage mechanisms, see the works by Egerton.[37,38]

$$D = \frac{jt}{e} \tag{3.11}$$

Electron dose control

There are several ways to control the electron dose on a specimen during focal-series image acquisition.[37] One method involves adjusting the exposure time and keeping all other microscope parameters fixed. The shorter the exposure time, the lower electron dose, while longer exposure time results in a higher dose. However, the success of this method is reliant on insignificant specimen drift either from residual stage movement or specimen charging effects. An alternative way of controlling the electron dose varies the beam current by means of changing the extraction voltage in the gun and keeping all other imaging conditions constant.

Arguably the simplest method of controlling the electron dose is by regulating the beam current density using the condenser lens to spread (lower dose) or focus (higher dose) the illumination. This method was selected for this study since it is easier to control (and reproduce) the electron dose by noting the exact condenser lens values at a fixed magnification, exposure time, and voltage. However, this method may result in illumination of the specimen regions beyond the detector field of view, thus, making it hard to establish which parts of the specimen have not been exposed to the electron beam. For extreme adjustments, it may also vary the convergence angle, which affects the contrast transfer function. However, a possible solution to the former may be to use specimen regions that are sufficiently distant from one another for acquiring different datasets in order to reduce the possibility of unintended pre-exposure to electrons.

Electron dose measurement

A quantitative study of the effects of the electron beam on a given material requires an accurate measurement of the applied electron dose during the experiment. For accurate electron dose measurement, the beam current has to be known. The incident beam current can be measured using either a Faraday cup or the fluorescent screen (if a Faraday cup is not installed) in the absence of any specimen that can obstruct the electron beam. When using the Faraday cup, the electron beam has to be focused and positioned at the centre of the Faraday cup, ensuring that the entire focussed beam passes into the faraday cup, from which the current *i*, can be directly recorded on a picoammeter. Alternatively, in the absence of a Faraday cup, the beam can be spread to fully cover the fluorescent screen, which measures the current density (pA/Å^2) (there is usually a calibration offset between the faraday cup and the fluorescent screen which needs to be determined for accurate current density measurement). Thus, the beam current (pA) value can be determined from the current density (pA/Å^2) if the area (Å^2) of the fluorescent screen is known (the diameter of a TEM fluorescent screen used was 160 mm). Once the current (*i*) is known, the total pixel counts (*c*) can be determined from an image acquired with a pre-set exposure time (*t*). These parameters can now be used to determine the gain (counts/primary electron), *g*, of the detector as:

$$g = \frac{c}{it/e} \tag{3.12}$$

Since there is a linear relationship between the number of electrons detected by the digital detector and the recorded digital pixel counts for a given accelerating voltage,[39] the gain of a detector is a constant for a given accelerating voltage. Thus, the electron dose can always be determined post-experiment from the mean count (*C*) in the image if the sampling interval (in Å), *S*, on the detector, is known and the exposure time is the same as that used to calculate the gain (*g*).

$$D = \frac{C}{g \times S^2} \quad (3.13)$$

3.3.2 Experimental Focal-Series Exit Wavefunction Reconstruction

The precursor catalyst

The hollow carbon spheres (HCSs) supported Co_3O_4 precursor catalyst was obtained from the University of the Witwatersrand. The catalyst synthesis procedure is summarised below. For a detailed account of the synthesis procedure, the reader is encouraged to see works by the Coville group.[40] This catalyst was chosen in this study because the catalytic performance Co FT catalyst is well understood[41], and the well-studied[42] inert support will not influence the activation procedure, as discussed in Chapter 2, section 2.2.2. In a typical procedure, Co_3O_4 nanoparticles were synthesised by a surfactant-free method using cobalt acetate as a precursor salt, benzyl alcohol as the solvent, and ammonia solution as the precipitating agent at 160 ℃.[43] Subsequently, HCSs were prepared by coating the spherical polystyrene (PSS) template with a resorcinol-formaldehyde (RF) polymer to form a composite (PSSs@RF). Template removal and carbonisation was performed following a one-step procedure inside a horizontal quartz tube by initially heating the composite under N_2 flow (50 ml/min) at 350 ℃ for 1 hr to decompose and remove the polystyrene template, followed by thermal annealing the HCSs at 600 ℃ for 2 hrs under the N_2 atmosphere. To prepare the catalyst, pre-synthesised nanoparticles were loaded on the surface of HCSs using ethanol as the dispersing solvent in an ultrasonicator.

Focal-series image acquisition and analysis

Focal-series of AC-TEM images of the precursor catalyst were acquired on a cold-field emission source double-corrected JEOL ARM-300F at 300kV fitted with a Gatan OneView camera. A through-focal-series of 40 images with a focal step of 10 Å were acquired using a 0.4 s exposure time at ×1.5M magnification. The gain of the Gatan OneView camera at 300 kV was calculated using eq. 3.12 and was found to be 36.31 counts/primary electron. This value was subsequently used to calculate the electron dose (eq. 3.13) for all the sets of focal-series of images acquired at different settings of the condenser lens (CL3) presented in Chapter 4. The complex specimen exit wavefunction was reconstructed a posteriori using a linear Weiner filter in the Focal and Tilt Series Reconstruction (FTSR) plugin in Gatan DigitalMicrograph.[25] All atomic models were generated using the CrystalMaker software. Multislice simulations of the phase of the specimen exit wavefunctions were performed by Mr Arthur Moya using the multislice algorithm[44–46] implemented in the MULTEM[47] code.

3.4 Imaging in Scanning Transmission Electron Microscope

Although a scanning electron microscope was constructed at about the same time as the TEM, Scanning Transmission Electron Microscopy (STEM) only became operational in the late 1960s due to the work of Crewe and co-workers.[48] In this configuration, a beam of electrons is focused into a fine probe at the surface of a thin specimen by the objective lens, and scanning coils are used to scan this probe over the specimen.[48] Most commonly, an annular dark field (ADF) detector is used to collect and integrate electrons to high angle, which provides a signal sensitive to the atomic number (Z-contrast) of the atoms in the specimen.[49]

In contrast to HRTEM imaging, an ADF image is formed incoherently using high angle scattering.[49] The incoherent imaging model describes the integrated intensity as the convolution of the probe function with the specimen object function as a function of a two-dimensional probe position on the specimen.[50] This makes ADF contrast simpler to interpret than HRTEM phase-contrast, which is more sensitive to specimen thickness and objective lens aberrations. The lens aberrations determine the probe function, and the introduction of aberration correctors in STEM made it possible to achieve atomic resolution routinely.[18,51–53] A particular advantage of STEM over TEM, is that the geometry of the STEM detection allows for simultaneous acquisition of ADF, X-ray and energy loss signals, thus providing simultaneous structural and chemical information from the same particle.

3.5 Electron Energy Loss Spectroscopy (EELS)

Electron energy loss spectroscopy (EELS) is a characterisation technique based on the analysis of the distribution of the energy lost by the incident electrons after interaction with the specimen.[54–56] Unlike related X-ray spectroscopic techniques[57], EELS can provide information about the thickness of the specimen, the chemical composition, valence states, and optical properties at a local scale- making EELS a particularly powerful analytical tool.[56]

3.5.1 The Electron Energy Loss Spectrum

The EELS spectrum represents a range of electron energy losses from 0 up to typically 3 keV. Figure 3.6 shows a typical non-background-subtracted EELS spectrum.[5] There are several significant features/regions in the spectrum, the most dominant being the zero-loss peak (ZLP).

This represents the elastically scattered electrons with the width of the ZLP reflecting the energy width of the electron source and the resolution of the spectrometer.

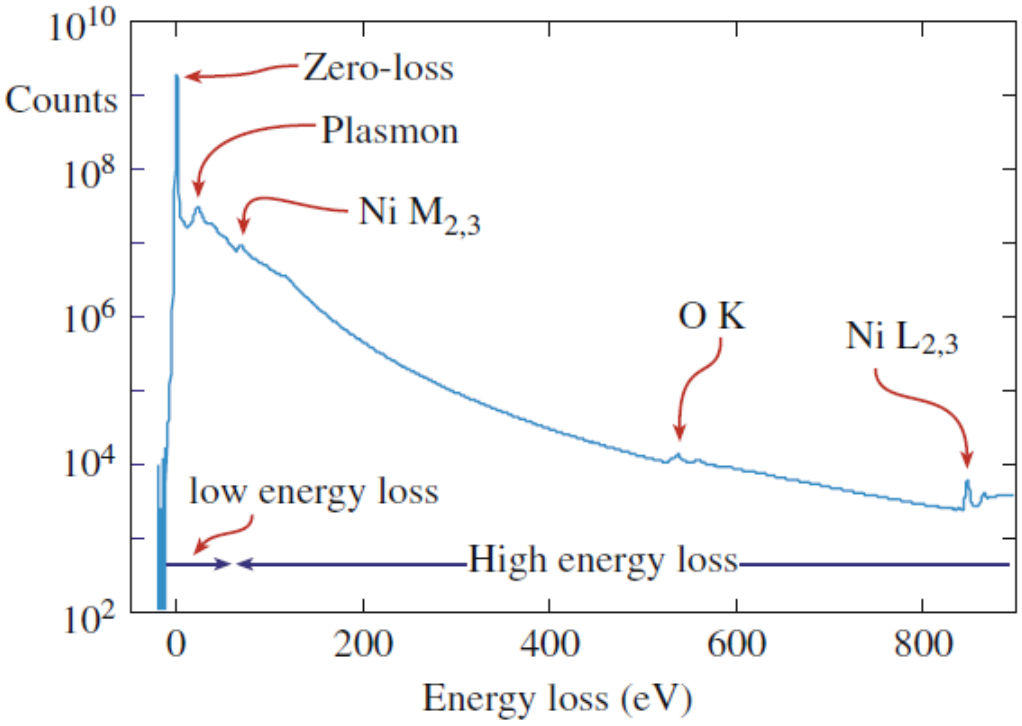

Figure 3.6. An example of an EELS spectrum. (Adapted from Ref. [5] *© 2009 Springer Science & Business Media, LLC)*

The remaining EELS spectrum can be divided into two regions; the low energy loss (valence-loss) below 50 eV, and the higher energy loss (core-loss) above 50 eV. The low-loss region features a plasmon peak resulting from inelastic scattering of incident electrons by valence electrons, causing resonance of the valence band electrons in the specimen. The core-loss region of the spectrum comprises various ionisation edges arising from the excitation of core electrons into unoccupied states. These give information about the density of states and chemical composition in the specimen.[58] This thesis will focus on the core-loss ionisation edges of oxygen (O-K) and cobalt (Co-$L_{3,2}$).

3.5.2 Electron Matter Interactions in EELS

Multiple possible interactions occur when high energy electrons interact with a specimen (as shown earlier in Figure 3.1).[5] Typically, incident electrons interact with the specimen atoms through electrostatic (Coulomb) forces. As a result of this interaction, some of the electrons are scattered; the direction of their momentum is changed, and in some cases, they transfer an appreciable amount of energy to the specimen. This classifies these interactions into *elastic* and *inelastic* scattering.[55,56]

Elastic scattering

Elastic scattering is caused by the interaction of incident electrons with the electrostatic field of atomic nuclei. The atomic electrons are involved only to the extent that they terminate the nuclear field and therefore determine its range and magnitude. Since the nucleus is some thousands of times more massive than an electron, the energy transfer involved in elastic scattering is usually negligible.[56] In EELS, the elastically scattered electrons make up the ZLP. For elastic scattering, the main property of interest is the angular distribution of the elastically scattered electrons. The differential cross-section, which describes the probability of scattering per unit solid angle, for elastic scattering in a non-crystalline material shows that for the typical incident electron energy (i.e. accelerating voltage) range used (60–300 keV), the angular distribution of elastic scattering increases with increasing specimen atomic number, Z, and decreases with increased accelerating voltage.[59] In crystalline specimens, the electrons are elastically scattered over a similar angular range for specific Z and accelerating voltage; however, the scattering is confined to discrete angles defined generally by the Laue equations.[55]

Inelastic scattering

Inelastic scattering occurs for core-shell electrons and valence electrons. For core-shell electron excitation, the incident electron collides with a core-shell electron with enough energy to cause an electronic excitation. Because of the total conservation of energy, the accelerated electron loses an equal amount of energy and is scattered at smaller angles than elastically scattered electrons. The relaxation of the excited atoms is accompanied by the transition of another core-electron of lower binding energy to the 'hole' from where the first electron was removed. The energy associated with this transition is released in the form of X-rays or Auger emission.[8]

Outer-shell electrons are weakly bound to the atoms in a solid. Hence the incident electrons can either eject a valence electron in which light is released during relaxation of the atom which can be measured by cathodoluminescence, or it can induce a collective oscillation of the valence electron density known as a plasmon resonance. Plasmons can be described as quasiparticles arising from the quantisation of the plasmon resonance, whose energy lies in the range 5–30 eV and can be used to determine the bandgap of semiconductors.[6,55]

Multiple scattering

From Poisson statistics, the probability of an electron to undergo multiple scattering events increases with specimen thickness. For relatively thick specimens, the transmitted electron is inelastically scattered by the valence electrons, in addition to core-shell electrons. The consequence of this is a broad double-scattering peak producing a post-edge hump, thus changing the ionisation edge shape and making it hard to analyse the fine structure.

3.5.3 Experimental EELS

Ex-situ STEM-EELS

Specimen preparation: Reduction of Co_3O_4

The hollow carbon spheres supported Co_3O_4 nanoparticles were loaded in a quartz tube and reduced at 350 °C in a tube furnace under a 100 mL/(min·g) flow of H_2 gas or syngas (CO/H_2 = 0.5) at atmospheric pressure for 20 hrs. The reduced catalyst was stored in an argon gas-filled glovebox before analysis, and all STEM specimens were prepared in the glovebox. The specimen was mounted on a single tilt holder and transferred to the microscope in air.

Spectrum imaging

The reduced Co FT catalysts were studied in a probe corrected JEOL ARM200F at the electron Physical Science Imaging Centre (ePSIC) operated at 200 kV with a Gatan GIF Quantum 965 ER spectrometer. A probe current of 13 pA, convergence semi-angle of 14 mrad, ADF inner and outer detector angles of 77.43–241.21 mrad, and a spectrometer collection angle of 39.6 mrad were used for simultaneous acquisition of both EELS and ADF signals. High-resolution ADF images were acquired using the same probe current. Additional STEM-EELS and ADF data were acquired on a second probe-corrected JEOL ARM200F at the David Cockayne Centre for Electron Microscopy under the same conditions. Low-loss valence and core-loss spectra were acquired simultaneously using the DualEELS mode.

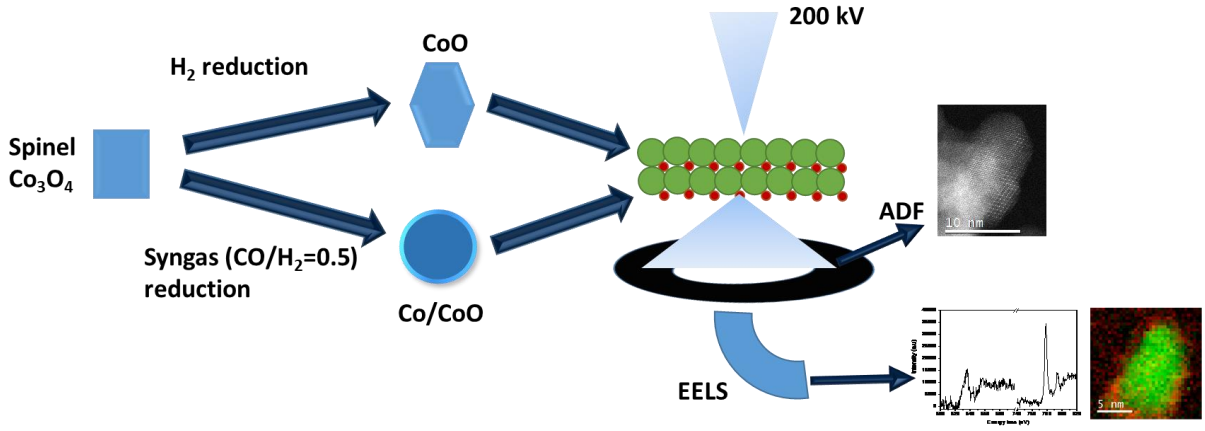

Figure 3.7. Schematic showing ex-situ activation and characterisation of cobalt FT catalyst.

In-situ STEM-EELS

MEMS nano-reactor and specimen holder

Micro-electro-mechanical system (MEMS) based nano-reactors are multifunctional specimen carrier devices, analogous to traditional TEM Cu grids, for variable temperature and gas-solid TEM experiments.[60–63] Each nano-reactor consist of two chips sandwiched together to form an airtight sealed reaction chamber capable of sustaining pressures up to 1.5 bar (Figure 3.8 (a)). The (bottom) heating chip onto which the specimen is deposited, is based on a double-spiral shaped Molybdenum micro-heater embedded in an electron transparent Si_3N_4 membrane capable of reaching temperatures up to 1300 °C (Figure 3.8 (b)). After depositing the specimen on the bottom chip, the nano-reactor is assembled, as shown in Figure 3.9, and tested for leak tightness using pressurised He. The nano-reactor is considered leak-tight when the leak rate is less than 1×10^{-9} mbar.L/s.[60]

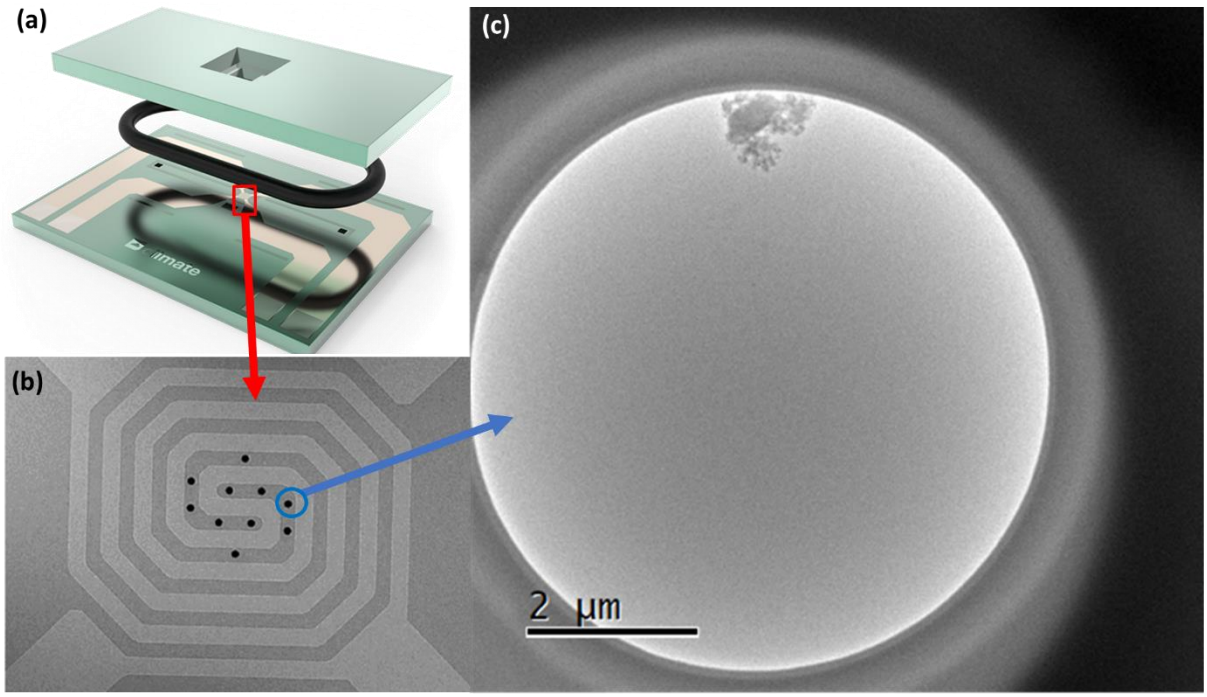

Figure 3.8. (a) DENS solution Climate nano-reactor top and bottom chips.[60] *(b) SEM image of the double-spiral heating MEMS with 10 Si_3N_4 electron transparent windows.*[60] *(c) STEM-ADF image of a specimen mounted over the transparent window. ((a) and (b) adapted from Ref.* [60]*. © 2016, IEEE).*

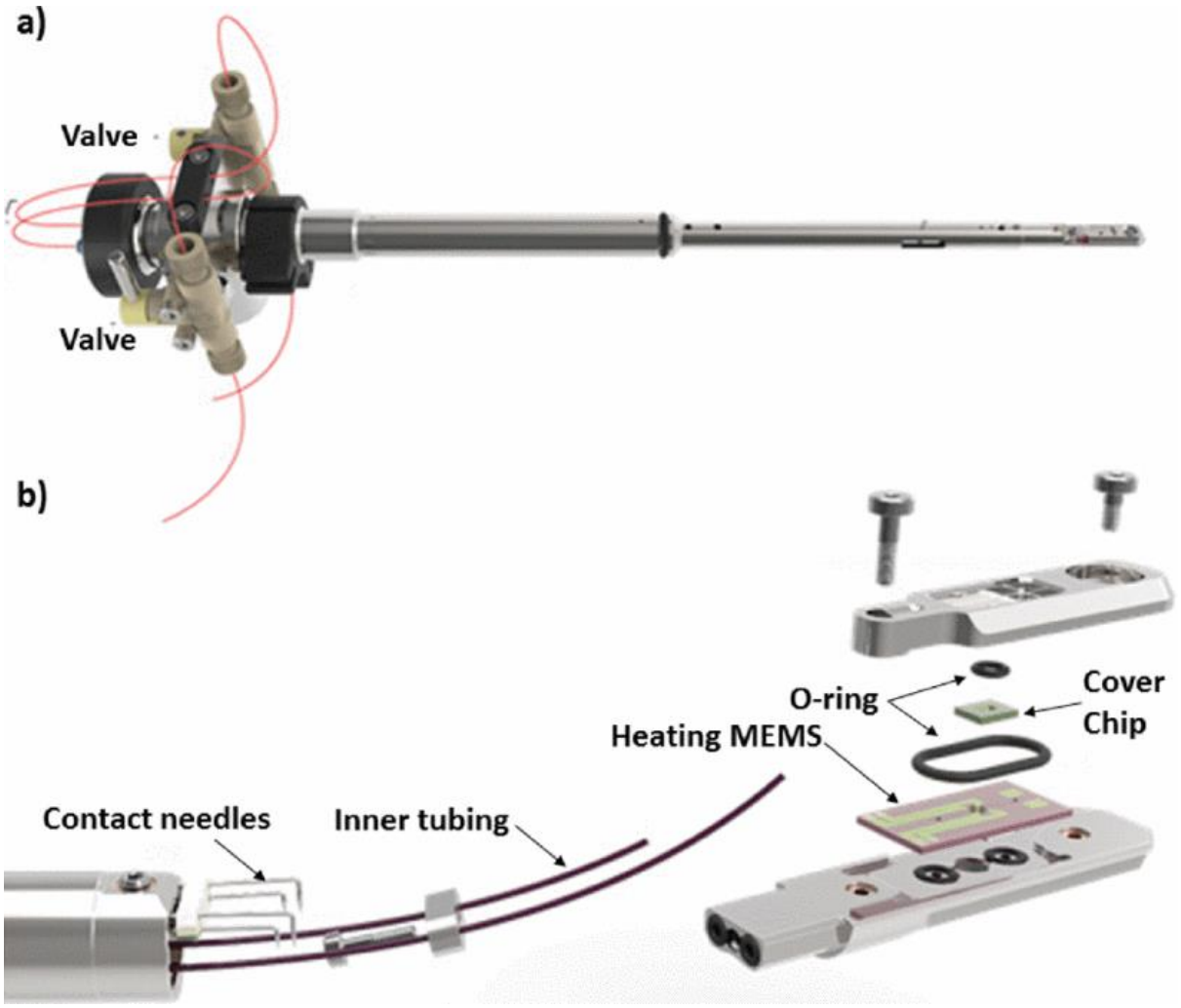

Figure 3.9. (a) DENS solution Climate nano-reactor specimen holder. (b) Enlarged components of the in-situ holder in assembly order. (Adapted from Ref. [60]*. © 2016, IEEE).*

In-situ spectrum imaging

In-situ reduction was performed in an aberration-corrected analytical scanning transmission electron microscope (JEOL ARM200F) at 200 kV with the same microscope conditions as for *ex-situ* analysis. A DENS solutions Climate *in-situ* Nano-reactor gas supply system capable of real-time dynamic mixing of 3 gasses over a temperature range from room temperature to 1300 °C was used. The gas supply system provided a 0.2 ml/min flow of H_2 at a pressure of 500 mbar for hydrogen activation, or a 0.2 ml/min flow of syngas (CO/H_2=0.5) at a pressure of 500

mbar for syngas activation. The temperature was ramped from room temperature to 150 °C to remove contaminants and further ramped to 350 C at 10 °C/min under a reducing environment. The temperature was then held at 350 °C for 2 hr for catalyst activation.

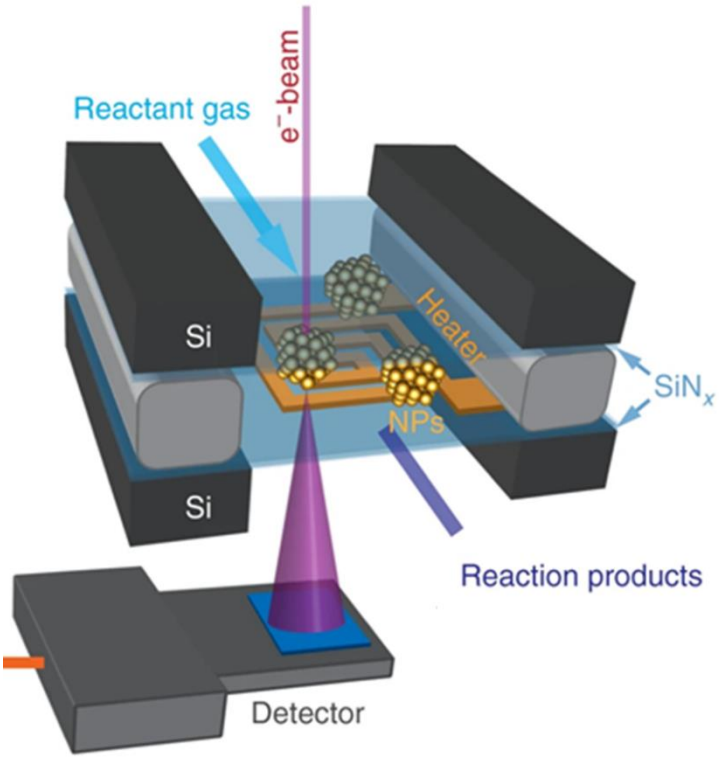

Figure 3.10. Schematic showing the in-situ activation and characterisation of cobalt FT catalyst using the MEMS nano-reactor. (Adapted from ref. [64]*. © 2020 Springer Nature Limited)*

Beam effects

The electron beam affects *in-situ* gas-solid experiments through ionisation of gaseous species which may alter the chemistry under study.[65] In order to minimise electron beam effects, all images and spectrum images were acquired using a probe current of 13 pA, which is significantly lower than typical STEM imaging probe currents of 50-100 pA.[66,67] According to previous reports, probe currents of ~ 20 pA or less are suitable for high-temperature gas-solid *in-situ* experiments.[68–70] In addition, scattering from the Si_3N_4 windows (~30 nm thick) reduces

the beam intensity, further reducing the possibility of electron beam effects.[68–70] Finally, the electron beam was blanked except during imaging, thereby ensuring that the specimen is not exposed to the electron beam while undergoing reduction. To validate this approach high-resolution STEM-ADF images acquired before (Figure 3.11 (a)) and after (Figure 3.11 (b)) spectrum imaging using a 13 pA probe current did not show any visible beam-induced surface structural or morphological modifications of the *ex-situ* reduced Co FT catalysts. Similarly, the corresponding EELS spectra show no changes in the fine structure of successively acquired EELS profiles (Figure 3.11 (c)), indicating that no oxidation/reduction takes place during spectrum imaging.

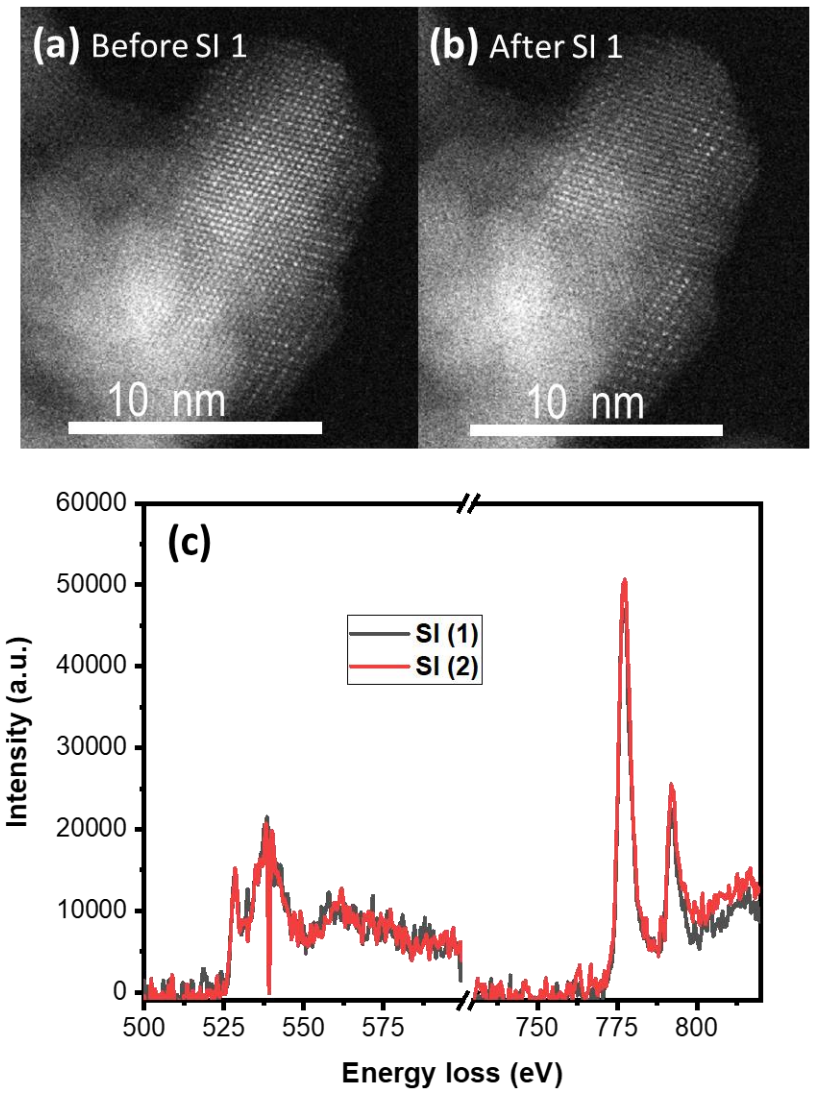

Figure 3.11. STEM-ADF images (a) before, and (b) after spectrum imaging. (c) Corresponding EELS spectra. SI 1 was acquired after image (a), and SI 2 acquired after image (b).

EELS data processing and quantification

The extraction of edge signals and elemental mapping was carried out using the Gatan Microscopy Suite® (GMS) 3 software, as shown in Figure 3.12. In this process, the background subtraction is modelled as a *power-law* as proposed by Egerton.[71,72] This is a function commonly used to remove the unwanted background from a core-loss edge by extrapolating a pre-edge fitting region (Figure 3.12 red curve). To extrapolate the background below a core-

loss edge, the portion of the pre-edge background to be modelled is defined and extrapolated by selecting a rectangular ROI over the desired range. Typically, a range starting 40-50 eV before the edge threshold and 25 eV in width is satisfactory.[73] This is automated in the GMS 3 software user interface.

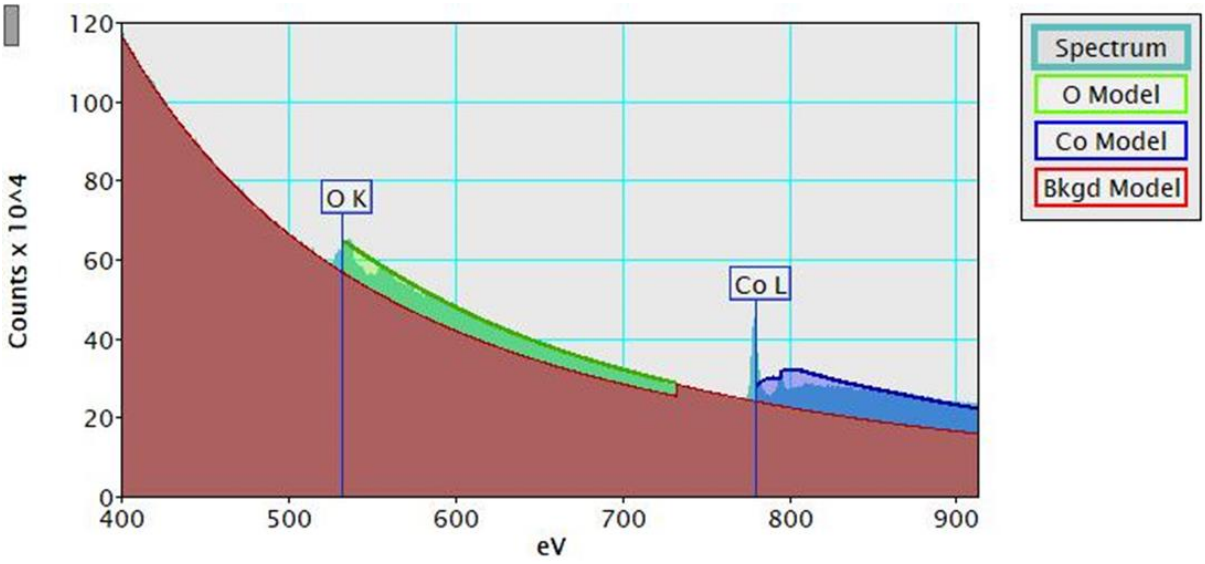

Figure 3.12. Illustrative elemental quantification of O-K and Co-L edges in the GMS 3 software.

Multiple scattering results in model edges shifting to higher intensities than the actual data, which then overestimates the quantification. The effect of multiple scattering is commonly removed by *Fourier-ratio deconvolution* of the background-subtracted extracted core-loss edge signal to obtain a reliable quantification.[56,74,75] In this approach, the single scattering distribution is calculated from the inverse Fourier transform (FT) of the deconvolution of the FT of the core-loss spectrum from the FT of the corresponding low-loss spectrum.[56] This is automated in the GMS 3 software user interface. Alternative deconvolution methods (*Fourier-log*) are preferred only for low-loss EELS, which is not of interest in this study. For a detailed comparison of the two deconvolution methods, see Egerton.[56]

The Co oxidation state before and after activation was estimated by comparison of the Co L_3/L_2 edge ratio, the position of the Co-L_3 edge, the Co L_3–L_2 peak-to-peak energy separation, and the O-K edge fine structure from EELS measurements of standard specimens with known Co oxidation states compared to those from activated catalysts. The values of the Co-$L_{3,2}$ intensities and energy losses were extracted and plotted from raw spectra using *ParticleSpy* script (https://github.com/ePSIC-DLS/ParticleSpy) developed by Dr. T. Slater.

3.6 References

(1) Ruska, E. *J. Ultrastruct. Mol. Struct. Res.* **1986**, *95* (1–3), 3–28.

(2) Freundlich, M. M. *Science*. 1963, pp 185–188.

(3) Knoll, M.; Ruska, E. *Zeitschrift für Phys.* **1932**, *78* (5–6), 318–339.

(4) Haguenau, F.; Hawkes, P. W.; Hutchison, J. L.; Satiat–Jeunemaître, B.; Simon, G. T.; Williams, D. B. *Microsc. Microanal.* **2003**, *9* (02), 96–138.

(5) Carter, C. B.; Williams, D. B. *Transmission Electron Microscopy*, 1st ed.; Carter, C. B., Williams, D. B., Eds.; Springer International Publishing: Cham, 2016.

(6) Brydson, R. *Aberration-Corrected Analytical Transmission Electron Microscopy*; Brydson, R., Ed.; John Wiley & Sons, Ltd: Chichester, UK, 2011.

(7) Kirkland, A. I.; Chang, S. L.-Y.; Hutchison, J. L. In *Springer Handbok of Microscopy*; Hawkes, P. W., Spence, J. C. H., Eds.; Springer Nature Switzerland AG: Switzerland, 2019; pp 3–38.

(8) Reimer, L.; Helmut, K. *Transmission Electron Microscopy*; Springer Series in Optical Sciences; Springer New York: New York, NY, 2008; Vol. 36.

(9) Cowley, J. M.; Pogany, A. P. *Acta Crystallogr. Sect. A Cryst. Physics, Diffraction, Theor. Gen. Crystallogr.* **1968**, *24* (1), 109–116.

(10) Kirkland, A. I.; Meyer, R. R. *Microsc. Microanal.* **2004**, *10* (04), 401–413.

(11) Scherzer, O. *J. Appl. Phys.* **1949**, *20* (1), 20–29.

(12) Hopkins, H. H. *Proc. R. Soc. London. Ser. A. Math. Phys. Sci.* **1951**, *208* (1093), 263–277.

(13) Barthel, J.; Thust, A. *Ultramicroscopy* **2013**, *134*, 6–17.

(14) Wade, R. H.; Frank, J. *Optik (Stuttg).* **1977**, *49* (1), 81–92.

(15) Frank, J. *Optik (Stuttg).* **1973**, *38* (1), 519–536.

(16) Scherzer, O. *Optik (Stuttg).* **1947**, *2*, 114–132.

(17) Rose, H. *Optik (Stuttg).* **1990**, *85*, 19–24.

(18) Rose, H. H. *J. Electron Microsc. (Tokyo).* **2009**, *58* (3), 77–85.

(19) Haider, M.; Rose, H.; Uhlemann, S.; Kabius, B.; Urban, K. *J. Electron Microsc. (Tokyo).* **1998**, *47* (5), 395–405.

(20) Haider, M.; Rose, H.; Uhlemann, S.; Schwan, E.; Kabius, B.; Urban, K. *Ultramicroscopy* **1998**, *75* (1), 53–60.

(21) Nellist, P. D. D.; Kirkland, A. I. I. *Philos. Mag.* **2010**, *90* (35–36), 4751–4767.

(22) Sawada, H.; Shimura, N.; Satoh, K.; Okunishi, E.; Morishita, S.; Sasaki, T.; Jimbo, Y.; Kohno, Y.; Hosokawa, F.; Naruse, T.; Hamochi, M.; Sato, T.; Terasaki, K.; Suzuki, T.; Terao, M.; Waki, S.; Nakamichi, T.; Takano, A.; Kondo, Y.; Kaneyama, T. *51 JEOL News* **2014**, *49* (1).

(23) Schiske, P. *Proc. Eur. Conf. Electron Microsc.* **1968**, 145–146.

(24) Saxton, W. O. *Ultramicroscopy* **1994**, *55* (2), 171–181.

(25) Meyer, R. . R.; Kirkland, A. . I.; Saxton, W. . O. *Ultramicroscopy* **2002**, *92* (2), 89–109.

(26) Coene, W.; Janssen, G.; Op de Beeck, M.; Van Dyck, D. *Phys. Rev. Lett.* **1992**, *69* (26), 3743–3746.

(27) Coene, W. M. J.; Thust, A.; Op De Beeck, M.; Van Dyck, D. *Ultramicroscopy* **1996**, *64* (1–4), 109–135.

(28) Zandbergen, H. W.; Tang, D.; Jansen, J.; Cava, R. J. *Ultramicroscopy* **1996**, *64*, 231–247.

(29) Van Dyck, D.; Op De Beek, M.; Coene, W. *Optik (Stuttgart)*. 1993, pp 103–107.

(30) Thust, A.; Coene, W. M. J.; Op de Beeck, M.; Van Dyck, D. *Ultramicroscopy* **1996**, *64* (1–4), 211–230.

(31) Thust, A.; Overwijk, M. H. F.; Coene, W. M. J.; Lentzen, M. *Ultramicroscopy* **1996**, *64* (1–4), 249–264.

(32) Kirkland, A. I.; Saxton, W. O.; Chau, K.-L.; Tsuno, K.; Kawasaki, M. *Ultramicroscopy* **1995**, *57* (4), 355–374.

(33) Kirkland, A. I.; Saxton, W. O.; Chand, G. *J. Electron Microsc. (Tokyo).* **1997**, *46* (1), 11–22.

(34) Ishizuka, K.; Allman, B. *Microsc. Today* **2005**, 22–24.

(35) Saxton, W. O. *Ultramicroscopy* **1994**, *55* (2), 171–181.

(36) Huang, C. Ultra high resolution imaging of radiation-sensitive materials, D.Phil. Thesis, University of Oxford, 2016.

(37) Egerton, R. F. *Ultramicroscopy* **2013**, *127*, 100–108.

(38) Egerton, R. F. *Microsc. Res. Tech.* **2012**, *75* (11), 1550–1556.

(39) De Ruijter, W. J.; Weiss, J. K. *Rev. Sci. Instrum.* **1992**, *63* (10), 4314–4321.

(40) Phaahlamohlaka, T. N.; Kumi, D. O.; Dlamini, M. W.; Forbes, R.; Jewell, L. L.; Billing, D. G.; Coville, N. J. *ACS Catal.* **2016**, acscatal.6b03102.

(41) Khodakov, A. Y.; Chu, W.; Fongarland, P. *Chem. Rev.* **2007**, *107* (5), 1692–1744.

(42) Li, S.; Pasc, A.; Fierro, V.; Celzard, A. *Journal of Materials Chemistry A*. Royal Society of Chemistry August 17, 2016, pp 12686–12713.

(43) Shi, N.; Cheng, W.; Zhou, H.; Fan, T.; Niederberger, M. *Chem. Commun.* **2015**, *51* (7), 1338–1340.

(44) Kirkland, E. J. *Advanced Computing in Electron Microscopy*; Springer US: Boston, MA, 2010; Vol. 40.

(45) Cowley, J. M.; Moodie, A. F. *Acta Cryst* **1957**, *10*.

(46) Goodman, P.; Moodie, A. F. *Acta Crystallogr. Sect. A* **1974**, *30* (2), 280–290.

(47) Lobato, I.; Van Dyck, D. *Ultramicroscopy* **2015**, *156*, 9–17.

(48) Crewe, A. V; Wall, J.; Welter, L. M. *J. Appl. Phys.* **1968**, *39* (13), 5861–5868.

(49) Nellist, P. D.; Pennycook, S. J. *Adv. Imaging Electron Phys.* **2000**, *113* (C), 147–203.

(50) Pennycook, S. J.; Jesson, D. E. *Phys. Rev. Lett.* **1990**, *64* (8), 938–941.

(51) Krivanek, O. L.; Corbin, G. J.; Dellby, N.; Elston, B. F.; Keyse, R. J.; Murfitt, M. F.; Own, C. S.; Szilagyi, Z. S.; Woodruff, J. W. *Ultramicroscopy* **2008**, *108* (3), 179–195.

(52) Krivanek, O. L. L.; Dellby, N.; Lupini, A. R. R. *Towards sub-Å electron beams*; North-

Holland, 1999; Vol. 78, pp 1–11.

(53) Batson, P. E.; Dellby, N.; Krivanek, O. L. *Nature* **2002**, *418* (6898), 617–620.

(54) Backx, C.; de Groot, C. P. M.; Biloen, P. *Appl. Surf. Sci.* **1980**, *6* (3–4), 256–272.

(55) Egerton, R. F. *Reports Prog. Phys.* **2009**, *72* (1), 016502.

(56) Egerton, R. F. *Electron Energy-Loss Spectroscopy in the Electron Microscope*, 3rd ed.; Springer US: Boston, MA, 2011.

(57) Sadeqzadeh, M.; Karaca, H.; Safonova, O. V.; Fongarland, P.; Chambrey, S.; Roussel, P.; Griboval-Constant, A.; Lacroix, M.; Curulla-Ferré, D.; Luck, F.; Khodakov, A. Y. *Catal. Today* **2011**, *164* (1), 62–67.

(58) Keast, V. J. *Mater. Charact.* **2012**, *73*, 1–7.

(59) Lenz, F. *Zeitschrift für Naturforsch. A* **1954**, *9* (3), 185–204.

(60) Perez-Garza, H. H.; Morsink, D.; Xu, J.; Sholkina, M.; Pivak, Y.; Pen, M.; Van Weperen, S.; Xu, Q. In *2016 IEEE 11th Annual International Conference on Nano/Micro Engineered and Molecular Systems, NEMS 2016*; Institute of Electrical and Electronics Engineers Inc., 2016; pp 85–90.

(61) Creemer, J. F.; Helveg, S.; Hoveling, G. H.; Ullmann, S.; Kooyman, P. J.; Molenbroeke, A. M.; Zandbergen, H. W.; Sarro, P. M. In *Proceedings of the IEEE International Conference on Micro Electro Mechanical Systems (MEMS)*; 2009; pp 76–79.

(62) Prasad, M.; Arya, D. S.; Khanna, V. K. *J. Micro/Nanolithography, MEMS, MOEMS* **2015**, *14* (2), 025003.

(63) Zandbergen, H. *Microsc. Microanal.* **2012**, *18* (S2), 1114–1115.

(64) Chee, S. W.; Arce-Ramos, J. M.; Li, W.; Genest, A.; Mirsaidov, U. *Nat. Commun.* **2020**,

11 (1).

(65) Noh, K. W.; Liu, Y.; Sun, L.; Dillon, S. J. *Ultramicroscopy* **2012**, *116*, 34–38.

(66) Batson, P. E. *Ultramicroscopy* **2006**, *106* (11-12 SPEC. ISS.), 1104–1114.

(67) Krivanek, O. L.; Dellby, N.; Murfitt, M. F.; Chisholm, M. F.; Pennycook, T. J.; Suenaga, K.; Nicolosi, V. *Ultramicroscopy* **2010**, *110* (8), 935–945.

(68) Avanesian, T.; Dai, S.; Kale, M. J.; Graham, G. W.; Pan, X.; Christopher, P. *J. Am. Chem. Soc.* **2017**, *139* (12), 4551–4558.

(69) Zhang, S.; Plessow, P. N.; Willis, J. J.; Dai, S.; Xu, M.; Graham, G. W.; Cargnello, M.; Abild-Pedersen, F.; Pan, X. *Nano Lett.* **2016**, *16* (7), 4528–4534.

(70) Zhang, S.; Chen, C.; Cargnello, M.; Fornasiero, P.; Gorte, R. J.; Graham, G. W.; Pan, X. *Nat. Commun.* **2015**, *6*, 1–6.

(71) Egerton, R. F. *Philos. Mag.* **1975**, *31* (1), 199–215.

(72) Egerton, R. F. *Ultramicroscopy* **1979**, *4* (2), 169–179.

(73) Liu, D.-R.; Brown, L. M. *J. Microsc.* **1987**, *147* (1), 37–49.

(74) Johnson, D. W.; Spence, J. C. H. *J. Phys. D. Appl. Phys.* **1974**, *7* (6), 771–780.

(75) Verbeeck, J.; Van Aert, S. *Ultramicroscopy* **2004**, *101* (2–4), 207–224.

Chapter 4 : Characterisation of Co_3O_4 Precursor Catalyst

4.1 Introduction

The production of active metallic Co typically occurs before Fischer-Tropsch (FT) synthesis in the reactor by reduction of spinel cobalt oxide (Co_3O_4), as described in Chapter 2, section 2.2.[1] It is, therefore, essential to characterise the precursor Co_3O_4 before activation to understand the changes in the morphology and surface atomic structure after activation. Co_3O_4 has a *normal*-spinel crystal structure with an oxygen face centred cubic (fcc) lattice.[2] The Co^{2+} and Co^{3+} cations occupy one-eighth of the tetrahedral interstitial sites and half of the octahedral sites per unit cell, respectively.[2]

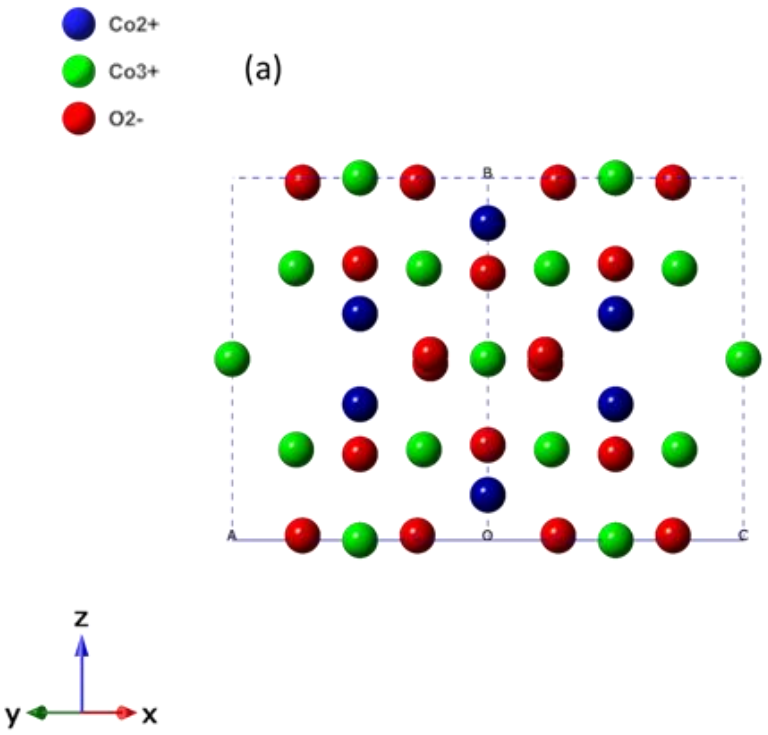

Figure 4.1. Atomic model of Co_3O_4 unit cell viewed along a <110> projection.

The intricacy of this spinel structure offers multiple possible surface terminations depending on the type of exposed surfaces and the shape of the crystal.[3] The structural arrangement of the Co_3O_4 surface terminations is critical to the activation of the Co catalyst because it may or not facilitate the adsorption of reducing gas (CO from syngas or H_2) molecules. Specifically, DFT studies indicate that CO molecules preferentially adsorb on surfaces with a high concentration of octahedral Co, while H_2 prefers surfaces with Co–O bridge sites.[4,5] Additionally, DFT calculations indicate that the presence of surface lattice O makes a significant contribution to lowering the adsorption energy of CO on the active sites of Co_3O_4, improving the reactivity of Co_3O_4.[6] However, this has not been explored experimentally, in detail due to the difficulty in resolving weakly scattering O atomic columns at the Co_3O_4 surface terminations using conventional TEM imaging. It is, therefore, useful to apply a characterisation technique with

sensitivity to both heavy (Co) and light (O) atoms with high spatial resolution in the characterisation of Co_3O_4 surface terminations.

Focal series Exit Wavefunction Reconstruction (EWR) is an established imaging technique used to determine the atomic structure of materials from a series of TEM images acquired at a different defoci where both heavy and light atoms can be resolved (see Chapter 3, section 3.3).[7,8] For metal oxide nanoparticles, it is essential to control the electron dose as it has been shown that the total electron dose used in the focal series acquisition has an impact on the phase of the restored exit wave function, affecting the signal-to-noise ratio (S/N) of the light atoms and changing the specimen due to beam-induced damage.[9,10]

In this chapter, the electron beam dose required to recover the phase of the Co_3O_4 specimen exit wavefunction from both the Co and O atomic columns with minimum beam-induced damage is determined. At this electron dose, the structure of alternative surface terminations of Co_3O_4 is examined, and their potential reactivity towards the adsorption and dissociation of reducing gas molecules (CO from syngas and H_2) is discussed.

4.2 Experimental

All the experimental details related to the specimen synthesis, imaging conditions, multislice simulations, and EWR are outlined in Chapter 3 section 3.3.2.

4.3 Results and Discussion

4.3.1 Morphology of the Co_3O_4 Precursor

The morphology of the Co_3O_4 precursor catalyst was investigated using conventional bright-field TEM, and a typical image is shown in Figure 4.2. The Co_3O_4 nanoparticles with a 6.4 nm average size are supported on the surface of hollow carbon spheres (HCSs) with a 200 nm diameter and a 25 nm shell thickness. The average particle size (diameter) distributions in this chapter were measured from the longest side of the cubic particles (i.e. diagonal) by hand on high-contrast particles on several TEM and ADF-STEM images using *ImageJ* software. The histogram plots and the statistics (*SD*– standard deviation, *N*– number of particles, *ave. size*– mean, *error*– SD/√n) were derived from *Origin* software using the measurements from *ImageJ*. The bottom inserts to Figure 4.2 shows well-dispersed nanoparticles, and their height relative to the support surface makes them protrude into the vacuum when viewed in 2D projection, and as such are suitable for single-particle high-resolution imaging.

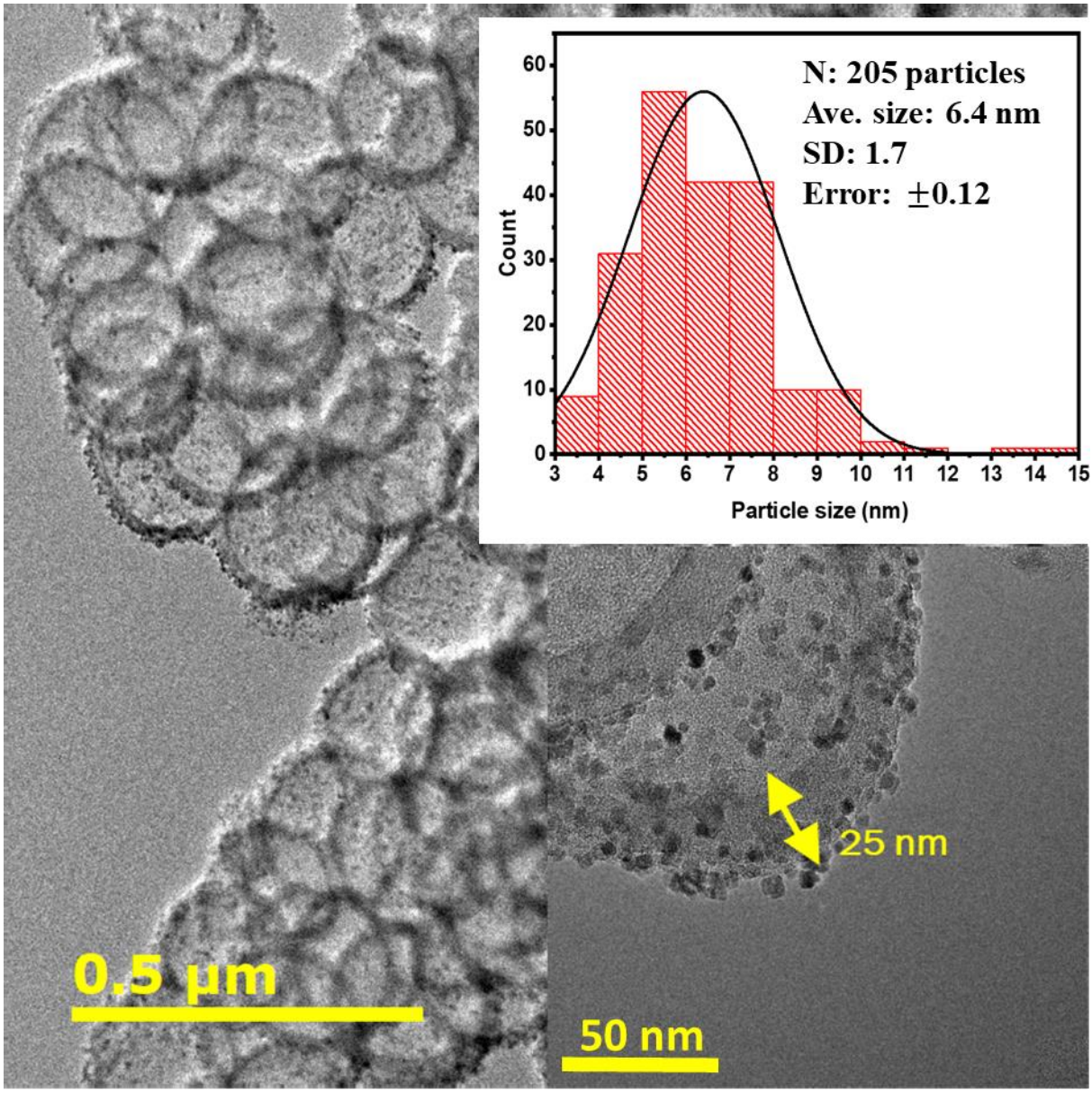

Figure 4.2. Bright-field image of as-prepared supported Co_3O_4 on hollow carbon spheres. The inserts show the Co_3O_4 average particle size distribution (top), the 25 nm support shell thickness, and the well-dispersed nanoparticles protruding into the vacuum (bottom).

4.3.2 Effect of Electron Dose on the Phase of the Exit wavefunction Reconstruction

Studies of the effect of electron dose on the restored phase of the Co_3O_4 EWR were carried for particles near a <110> projection because the *normal*-spinel structure has separated, single element occupied atomic columns of O, octahedral and tetrahedral Co atoms along this axis (Figure 4.3). For ***normal*** bulk spinel Co_3O_4, Co is *always* in either the 3+ and 2+ oxidation state at the octahedral and tetrahedral positions, respectively.[2] However, the exact oxidation state of Co may be different at the surface due to polarity charge compensation[11] (i.e. A phenomenon common on oxides were electrostatic instabilities arise in an instance where a surface termination has a non-zero dipole moment which can only be cancelled by the introduction of compensating charges on the outer planes, for a detailed account of polar oxide surfaces see Noguera[11]). As a result, this chapter focuses on methods for resolving the positions of Co and O atomic columns and not on their exact valence state. Importantly, the single element occupancy in projection makes it possible to distinguish the phase shifts of O from those of Co atomic columns.

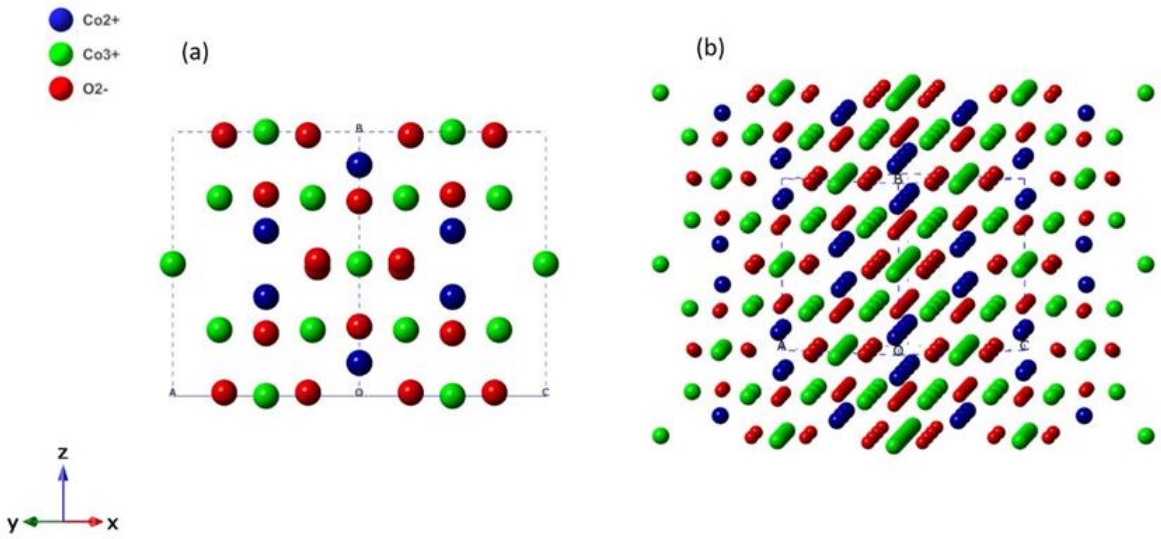

Figure 4.3. (a) Atomic model of a <110> projected Co_3O_4 unit cell. (b) Tilted model of a <110> projection highlighting single element occupancies in projection.

Figures 4.4 (a)-(d) shows the effect of electron dose on the phase of the restored exit wavefunction of Co_3O_4. The electron dose values indicated in Figure 4.4 correspond to the dose used to acquire a single image in a series of 40 images. When electron doses of 117 and 256 e/Å^2 per frame (Figure 4.4 (a) & (b)) were used, only the octahedral Co atomic columns on the (111) plane were resolved, but not the O columns. The corresponding cumulative electron dose, which is found by multiplying the electron dose per frame by the number of frames in the focal series, gives a total value of 4680 e/Å^2 and 10240 e/Å^2 for figures 4.4 (a) & (b), respectively. Comparing these values to those in the literature, where a minimum value of ~10850 e/Å^2 is reported for the detection of light atoms in Co_3O_4,[10] the O atomic columns in Figures 4.4 (a) & (b) may not be resolved because the used cumulative electron dose is lower than the required minimum threshold.[10]

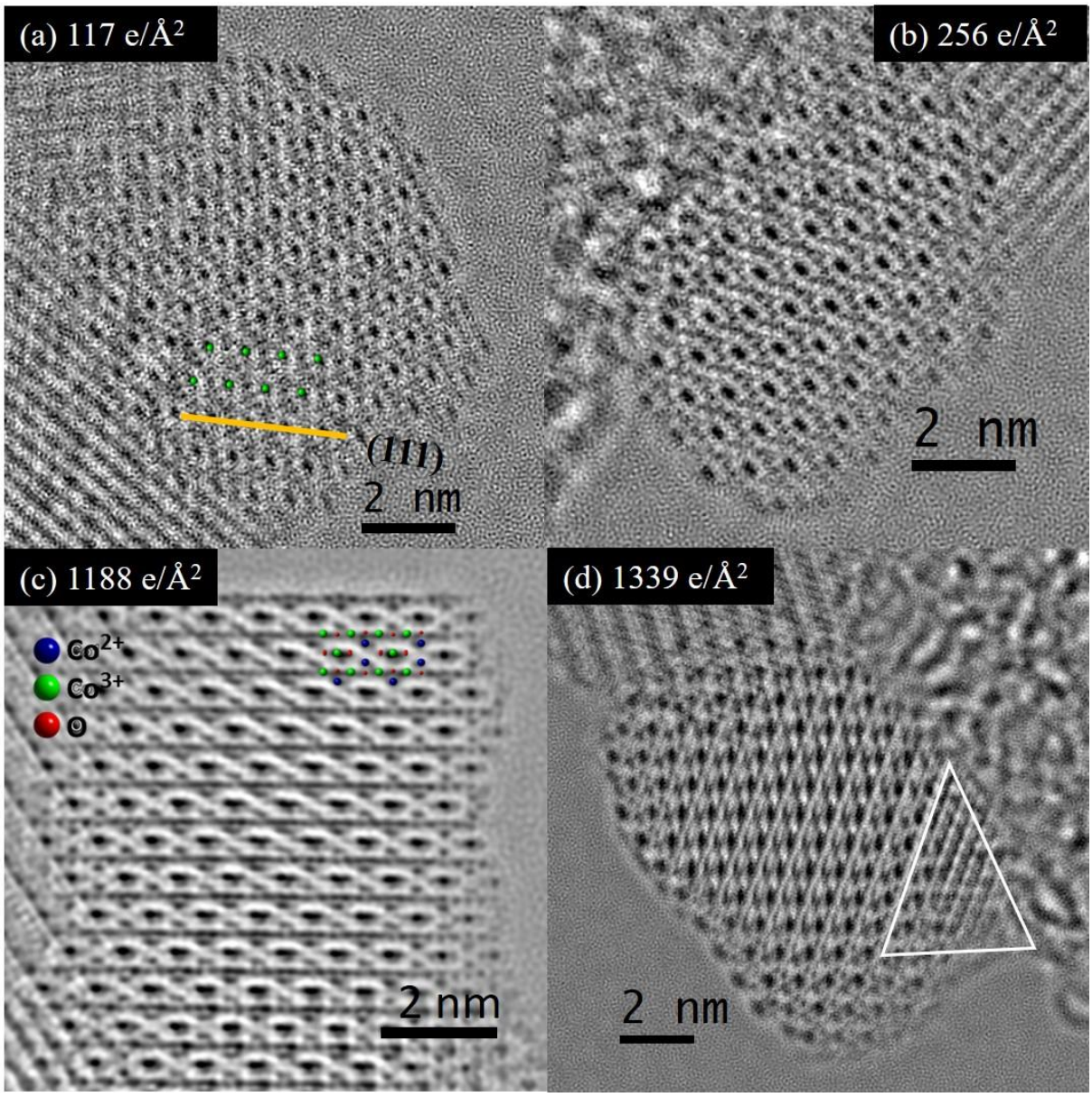

Figure 4.4. (a)-(d). The effect of electron dose (e/Å^2 per frame) on the phase of the restored exit wavefunction of Co_3O_4 along a <110> direction. Overlaid atomic models show the positions of different elements in the projected <110> structure. The white triangle in (d) shows the beam-induced structural rearrangement.

Increasing the electron dose to 1188 e/Å^2 per frame (Figure 4.4 (c)) over a 40 image series gave a phase of the restored specimen exit wavefunction that can be directly related to the Co_3O_4 atomic structure (see overlaid atomic model) with both Co and O atomic columns resolved without visible beam-induced damage. As a result, this electron dose satisfies the required

conditions (i.e. minimising specimen damage while maximising O signal) for characterisation of Co_3O_4 surface terminations in this study. A higher dose of 1339 e/Å^2 per frame (Figure 4.4 (d)) resulted in beam-induced structural rearrangement (the white triangle insert in Figure 4.4 (d)). As discussed in Chapter 3, section 3.3.1, the accumulation of excess electrons on the surface of the nanoparticle during focal-series acquisition results in beam-induced particle rotation and rearrangement of the atoms in projection, such that the final atomic structure of restored phase does not match the initial atomic structure of a <110> projection of Co_3O_4 (as in Figure 4.4). This is confirmed by the power spectrum (Figure 4.5) of the reconstructed region in question showing a typical pattern of a <111> zone axis, which does not correspond to a <110> projection of Co_3O_4 under study. In agreement, density functional theory (DFT) studies have shown that a <110> projection preferentially transforms into a <111> projection through relaxation to stabilise the particle[12], as observed for the particle shown in Figure 4.5 when subjected to a dose of 1339 e/Å^2 per frame.

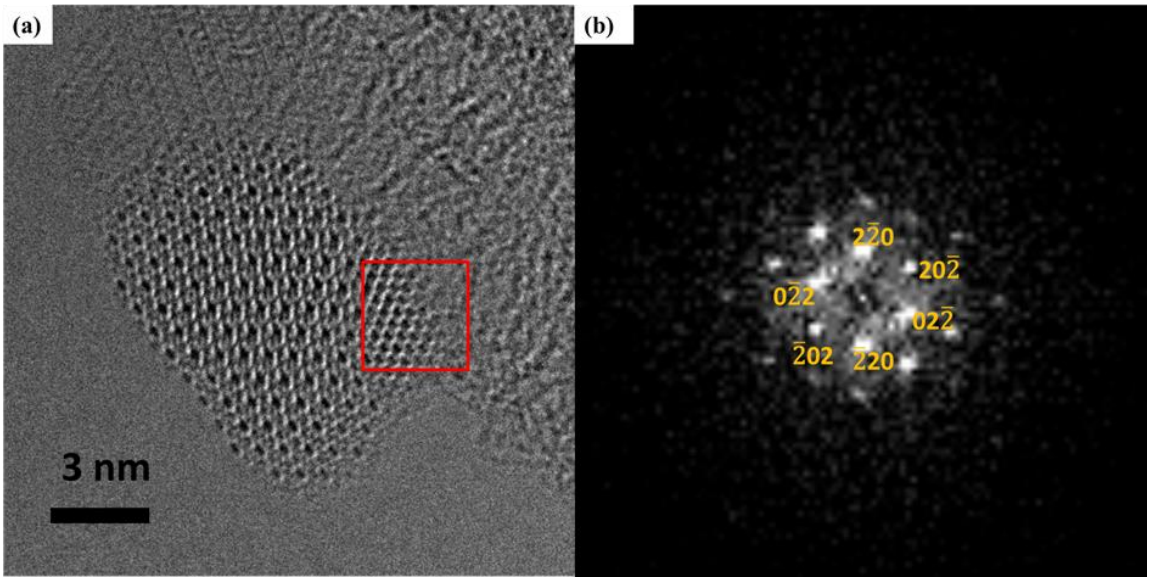

Figure 4.5. (a) Single frame (no 38 in the series) from a focal series of 40 images acquired at a dose of 1339 e/Å^2 per frame showing a structural reconstruction from <110> to <111> in the marked red square. (b) Extracted power spectrum showing a <111> pattern with labelled {022} reflections.

4.3.3 The Atomic Structure of Co_3O_4 Surfaces

After determining a suitable (i.e. for minimum beam damage with sufficient signal from the O columns) electron dose for focal series acquisition, the 1188 e/Å^2 per frame electron dose was used to image the local atomic structure and surface terminations of Co_3O_4 viewed along different projections (Figures 4.7 & 4.10). Care was taken to avoid unnecessarily prolonged beam exposure from tilting the specimen onto a zone axis and instead particles that were already suitably oriented were imaged. Consequently, some particles were not exactly aligned to a zone axis, resulting in a 'blurred' centre of the particle in the phase (Figure 4.6 (a)) and truncated power spectrum (Figure 4.6 (b)). The effect of specimen tilt becomes apparent in thicker regions (i.e. bulk) of the particle, and less so on the surfaces of the particle (which is the area of interest in this study), because the angular distance between the normal (i.e. imaging direction, Z) and the tilted column increases with the length of the tilted column, as observed in Figure 4.3 (b).

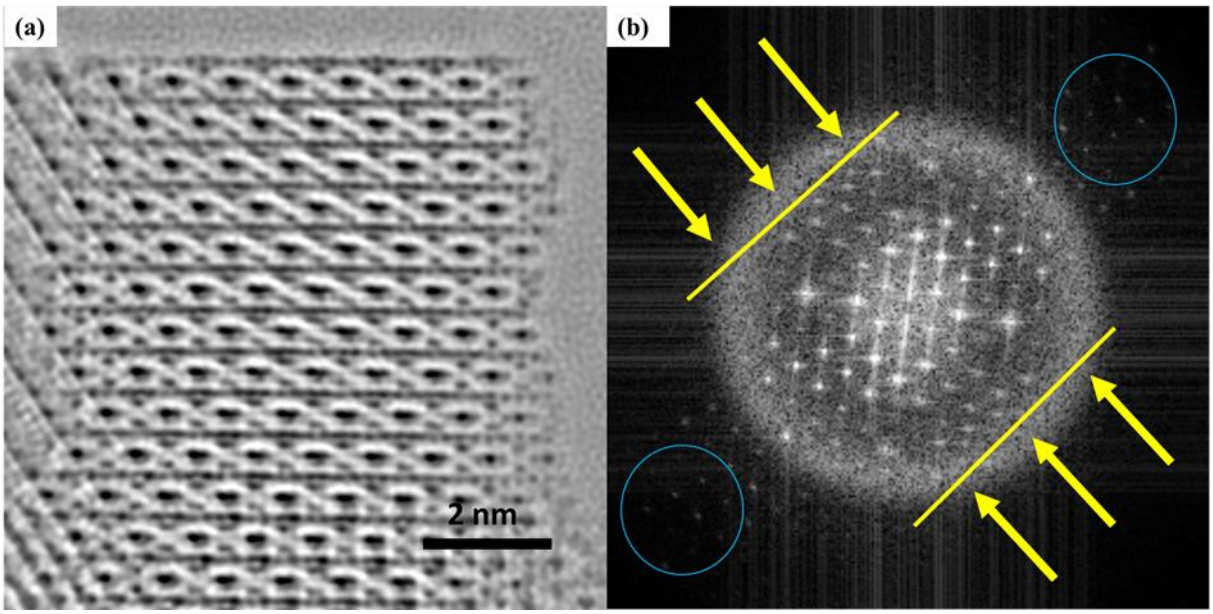

Figure 4.6. (a) *The phase of the restored exit wavefunction of a Co_3O_4 nanoparticle viewed near a <110> zone axis, and (b) its power spectrum. The truncated power spectrum (yellow arrows in (b)) is indicative of specimen tilt, which results in the blurred centre in the phase (a).*

Figure 4.7 (a) shows the phase of the restored exit wavefunction of Co_3O_4 viewed near a <110> zone axis. The bulk (or near-surface) atomic structure qualitatively matches the multislice simulated <110> atomic structure (Figure 4.7 (a) insert), with a projected planar (111) spacing of 4.9 Å between the octahedral Co atomic columns and a projected atomic distance of 1.1 Å between the tetrahedral Co and O atomic columns on a {100} surface, with an 8% total standard error, derived from the statistical, systematic and magnification errors using the Pythagorean theorem (eq. 4.3). The statistical error was determined from the standard deviation (σ) of the average of a number (n) of measured projected atomic distances extracted from line profiles of surface terminating layers, as in equation 4.1. The systematic error was derived from the variation in the average projected atomic distance due to the change in a single projected distance measurement by +/- 1 pixel in the line profile and also calculated using equation 4.1. The magnification error was estimated by taking a line profile in the bulk of the same

nanoparticle imaged at two different magnifications and comparing each to the known projected atomic distance using equation 4.2. The ratio of the line profiles of the same atomic columns at two different magnifications gave a 99.7% correlation, confirming that there is no significant change in the measured projected distances with a change in magnification.

$$Error = \frac{\sigma}{\sqrt{n}} \tag{4.1}$$

$$Mag.\ error = \frac{|known\ value - measured\ at\ mag\ x\ |}{known\ value} \tag{4.2}$$

$$\%\ Total\ standard\ error = 100 \times \sqrt{Stat^2 + Syst^2 + Mag^2} \tag{4.3}$$

The nanoparticle (Figure 4.7 (a)) has two observable surfaces, exposed in a vacuum: an atomically flat {100} and a rough/defective {110} surface. According to DFT[13] calculations, the {100} surfaces are either terminated by $Co^{o}O–Co^{t}$ or $Co^{t}–Co^{o}O$ (the first part of the hyphen denotes the terminating atomic layer and the second is the following atomic layer in the surface. Co^{o} and Co^{t} denote octahedral and tetrahedral Co atomic columns, respectively). The $Co^{o}O–Co^{t}$ termination is reportedly more thermodynamically stable than the $Co^{t}–Co^{o}O$.[13] In this work, a {100} surface is terminated by a facet composed of a horizontally alternating octahedral Co and O atomic layers ($Co^{o}O–Co^{t}$), (Figure 4.7 (a)). Experimental observation of the thermodynamically stable {100} surface termination confirms that the observed surfaces are free of beam-induced specimen alterations.

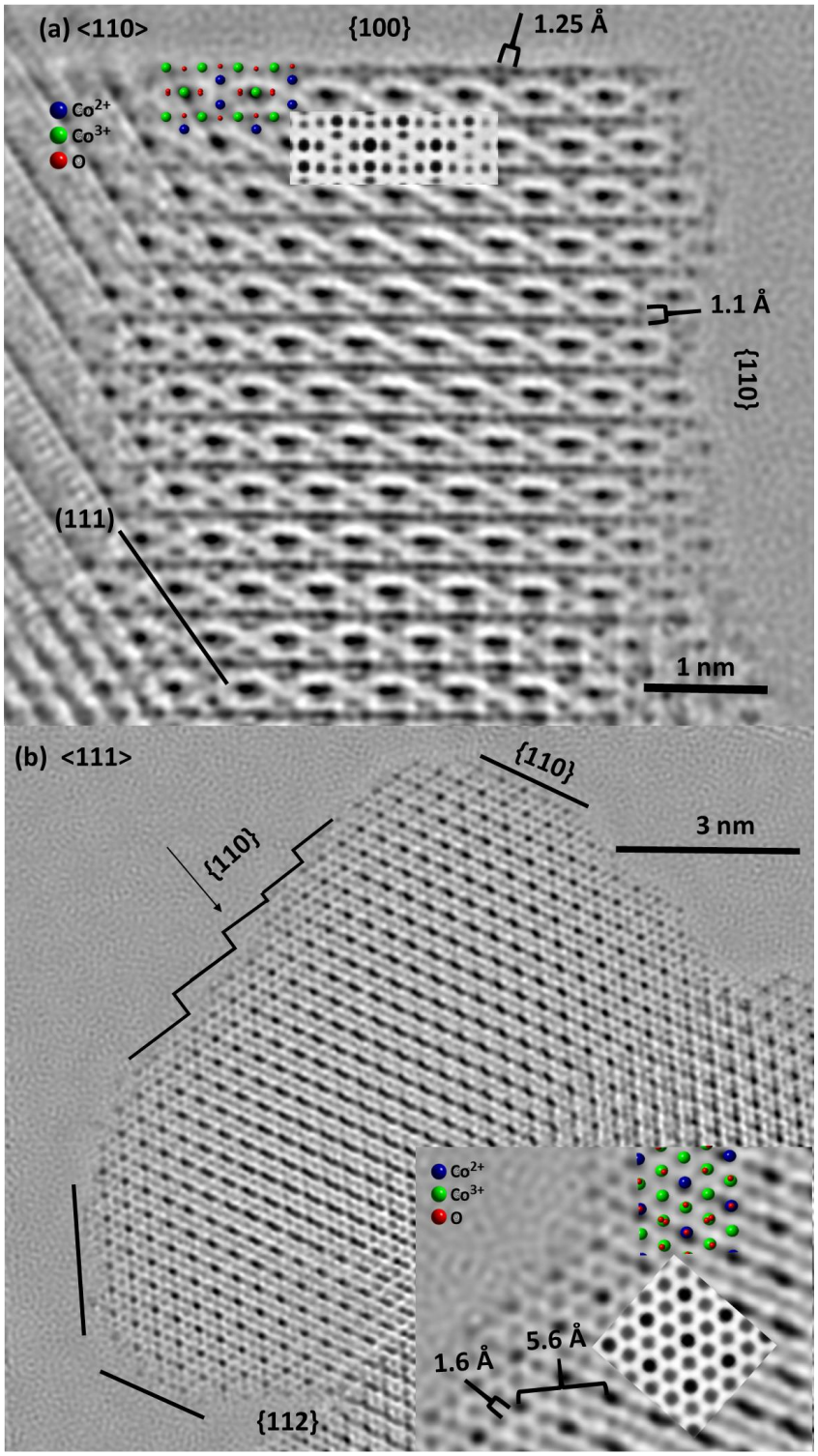

Figure 4.7. The phase of the restored exit wavefunction of Co_3O_4 projected from (a) <110> and (b) <111> zone axes.

The measured projected atomic distance of 1.25 Å (± 0.1 Å) between the octahedral Co and O atomic columns of the {100} surface termination (Figure 4.7) is smaller than the bulk (1.43 Å). The difference is considered significant because it is above the error margin. This difference in the projected distance may be a result of the relaxation of the structure at the surfaces, which is typically accompanied by a reduction in Co–O bond length and ionic charge compensation (i.e. a change in the density of states at the surface relative to the bulk).[11,13] This phenomenon is commonly observed in metal oxides in which electrostatic instabilities arise in an instance where a surface termination has a non-zero dipole moment which can only be cancelled by the introduction of compensating charges on the outer planes, accompanied by changes in the bond lengths at the surface termination.[11] This surface restructuring has been observed both theoretically using DFT[13] calculations, and experimentally[2] in negative spherical aberration-corrected imaging of Co_3O_4. The presence of lattice O at the surface termination has been shown to positively affect the reactivity of Co_3O_4 surfaces towards CO and H_2. For example, Jiang and Dai's[6] DFT calculations showed that a CO molecule adsorbs more efficiently on both octahedral Co and O, forming a Co–C–O triangular structure which makes CO dissociation easier. Thus the {100} surface termination in Figure 4.8 (a) would be an ideal candidate active site for reactions proceeding by CO dissociation such as Co_3O_4 activation in syngas.

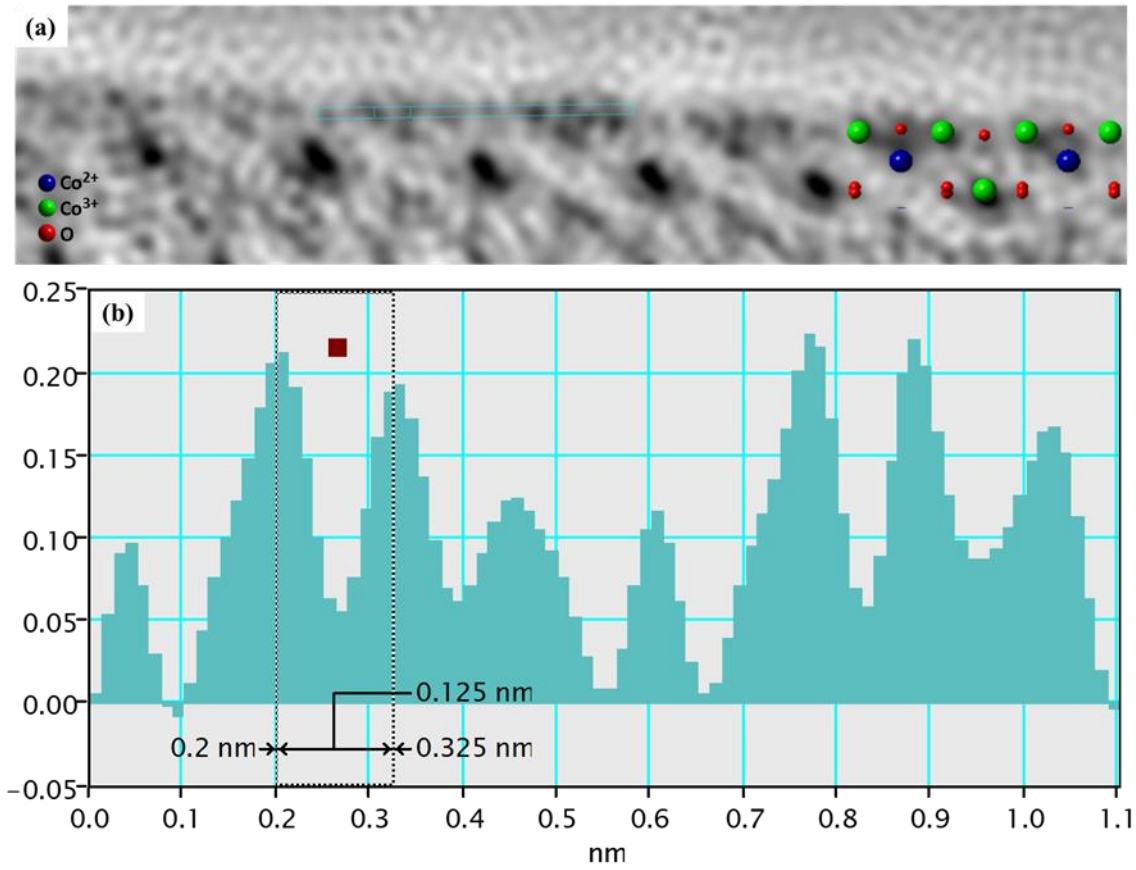

Figure 4.8. (a) An enlarged restored phase of the {100} surface of Co_3O_4 from Figure 4.7 (a) showing the surface termination. (b) An example of a line profile of the terminating atomic layer showing the measured projected atomic distance between the octahedral Co and O atomic columns. The standard error in the measured projected atomic distance is 8%.

The second surface in Figure 4.7 (a) is a {110} surface. DFT studies show that this surface is either terminated by $Co^tCo^oO–Co^oO$ or $Co^oO–Co^tCo^oO$ atomic layers, conventionally termed Type A & B,[3] with the latter being thermodynamically preferred.[13] In contrast, the {110} surface (Figure 4.9) has a rough surface termination comprising mainly of atomic columns of O and some octahedral Co projected in a vacuum (indicated by red arrows in Figure 4.9). This surface roughness is likely to have resulted from specimen preparation as there is no evidence that the electron beam dose used does induce structural damage.

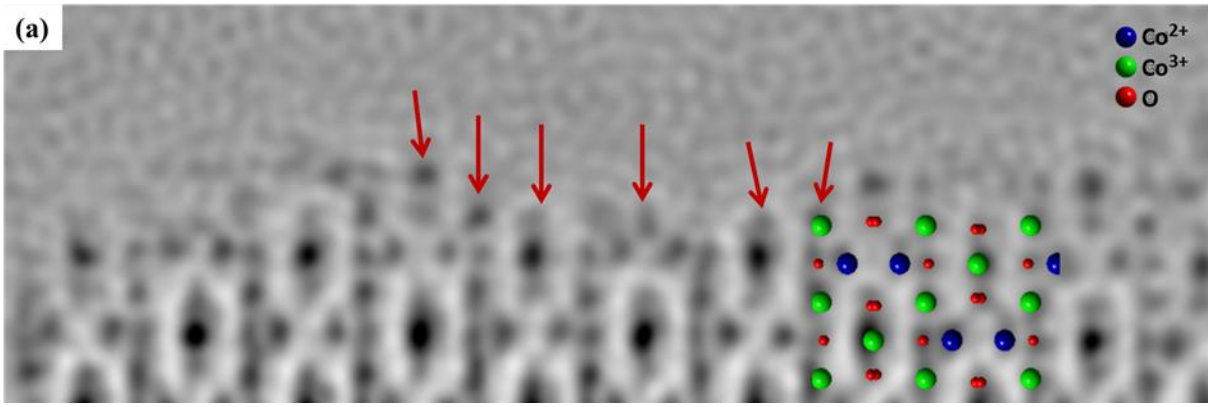

Figure 4.9. An enlarged restored phase of a rough {110} surface of the Co_3O_4 nanoparticle in Figure 4.7. The O and octahedral Co projected in vacuum are indicated by the red arrows. The atomic model of a <110> projection is overlaid.

Defective Co_3O_4 surfaces, such as the {110} surface in Figure 4.9, are known to have different reactivity compared to flat/perfect surfaces due to differences in surface energy and atomic configurations at the surface.[4,5,14] Specifically, Zhang *et al*.[4] showed that the adsorption energy of H_2 on a defective Co_3O_4 {110} surface (-0.47 eV) is much lower than on a perfect {110} surface (-0.18 eV) using DFT calculations. Similar reactivity trends between defective and perfect surfaces have been reported elsewhere.[5,14] Hence, it is possible that the defective nature of the {110} surface may enhance the reactivity of Co_3O_4 during Fischer-Tropsch catalyst activation.

Additional equivalent {110} surfaces were viewed from a different projection on another Co_3O_4 nanoparticle showing a potentially different termination from Figure 4.9. Figure 4.7 (b) shows the recovered phase of a Co_3O_4 particle viewed along a <111> direction. The local atomic structure was found to have a projected planar distance of 5.6 Å between the tetrahedral

Co atomic columns on {112} planes, and an interatomic distance of 1.62 Å (± 0.13 Å) between the octahedral and tetrahedral Co atomic columns on {110} planes (insert in Figure 4.7 (b)).

A <111> projection in the experimental phase near the particle surface qualitatively matches a multislice simulation (Figure 4.7 (b) insert). The atomic model shows that all the atomic columns in projection have mixed occupancy; thus, the O atomic columns cannot be resolved from the Co columns in projection. The nanoparticle (Figure 4.7 (b)) is enclosed with a majority of equivalent {110} surfaces, and a smaller {112} surface. The {110} surfaces have a Type B ($Co^{o}O–Co^{t}Co^{o}O$) surface termination and one-stepped surface. This surface defect is likely formed during specimen synthesis rather than being electron beam-induced, as described earlier in the discussion. The measured projected interatomic distance between the octahedral Co atomic columns at the {110} surface termination (1.62 Å, (± 0.13 Å)) was found to be the same as in bulk (1.62 Å), indicating no significant surface relaxation. This is consistent with DFT calculations which predict that the surface terminations of densely packed atomic layers do not undergo any surface rearrangement.[13]

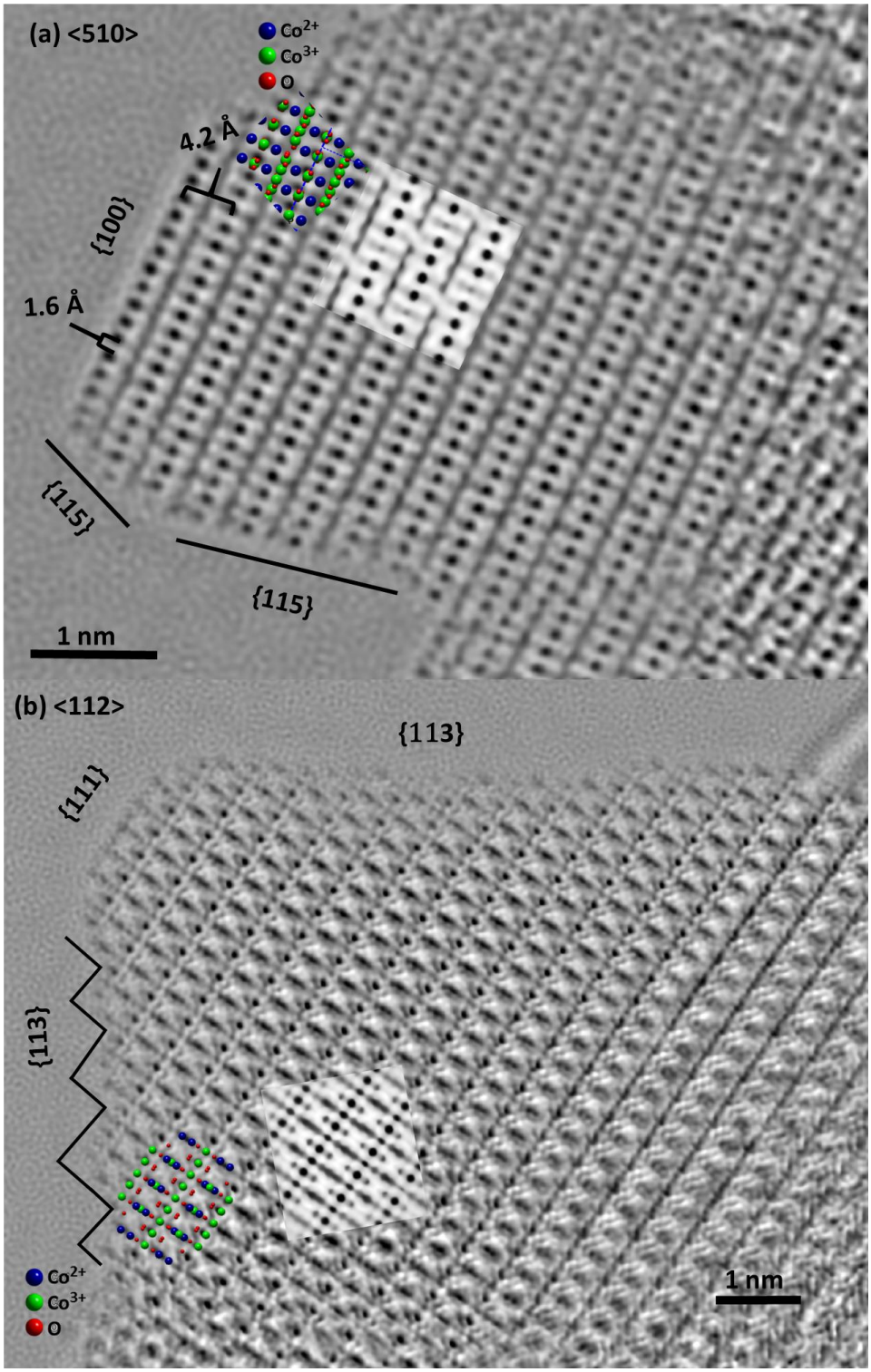

Figure 4.10. The phase of the restored exit wavefunction of Co_3O_4 projected from the (a) <510> and (b) <112> zone axes.

Similarly, densely packed surface termination was also observed on a {100} surface of a different nanoparticle viewed along a <510> zone axis (Figure 4.10 (a)). High index zone axes like this are not unusual in spinel structures since a single unit cell consists of 56 ions, providing a multitude of possible high symmetry projections. The measured projected interatomic spacing of 1.62 Å (± 0.13 Å) between adjacent octahedral Co atomic columns (Figure 4.11), the same as in bulk (1.62 Å). However, in contrast to the equivalent {100} surface termination viewed along a <110> zone axis (Figure 4.8), with a projected 1.25 Å (± 0.1 Å) distance between O and octahedral Co atomic columns, the orientation of the $Co^{o}O–Co^{t}$ {100} termination in a <510> projection (Figure 4.11) has alternating O and Co atomic columns in the Z direction (mixed occupancy in projection, see the overlaid atomic model in Figure 4.11). This accounts for the different measured projected atomic spacing. However, the reactivity of the surface towards CO or H_2 does not differ because both surfaces contain the same surface terminating atoms.

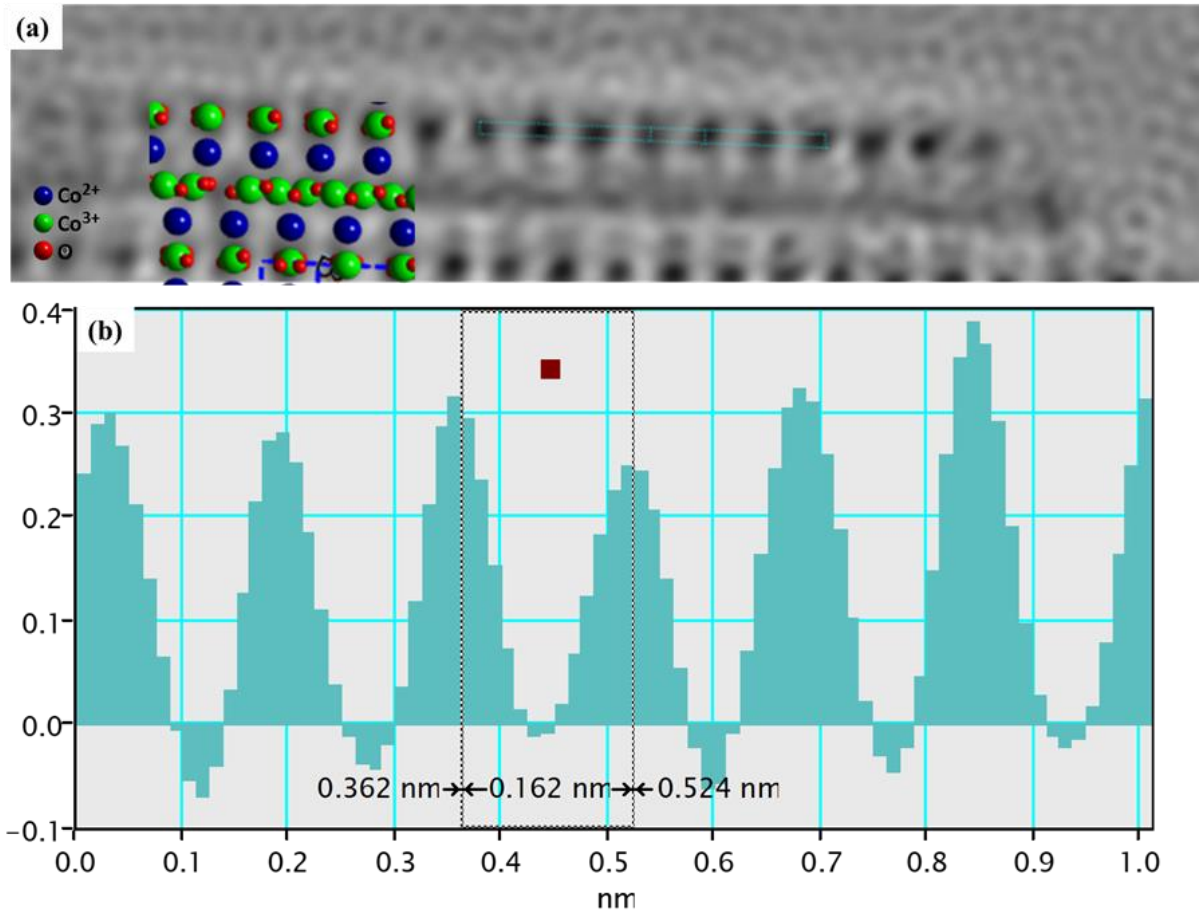

Figure 4.11. (a) An enlarged restored phase of a {100} surface termination of Co_3O_4 viewed along a <510> zone axis. (b) Line profile of the projected atomic distance of the atomic columns in the terminating layer. The measurement has an estimated standard error of 8%.

The equivalent {115} surfaces observed in Figure 4.10 (a) are both terminated by a densely packed layer of $Co^tCo^oO–Co^oO$. Such high index surfaces with intricate and dense atomic packing are rarely studied experimentally due to their thermodynamic instability.[13] As a result, there is a lack of experimental and theoretical studies of such surfaces. Similarly, the restored phase of a Co_3O_4 nanoparticle viewed in a <112> projection (Figure 4.10 (b)) has three surfaces; equivalent {113} surfaces with one defective, and a {111} surface.

Table 4.1. Summary of the common Co_3O_4 surface terminations compared against DFT terminations from literature.

Surface	Termination	
	This study	**Literature: DFT**
{100}	$Co^oO–Co^t$	$Co^t–Co^oO$ or $Co^oO–Co^t$ Ref.[13]
	$Co^oO–Co^t$	
{110}	Rough	Type A ($Co^tCo^oO–Co^oO$)
	Stepped	or Type B ($Co^oO–Co^tCo^tO$) Ref.[3,13]
	Type B	
	Type B	
	Type B	
{111}	$O–Co^t$	$O–Co^t$, $O–Co^o$, $Co^t–Co^o$, $Co^t–O$, $Co^o–Co^t$, $Co^o–O$ Ref.[13]

A qualitative comparison of multislice simulations and atomic model structures with experiments has enabled the identification of the atomic structure and terminations of Co_3O_4 surfaces (inserts in Figure 4.10 (b)). In this study, the {111} surface is $O–Co^t$ terminated. This termination is one of the six possible terminations of a {111} surface.[13] Spinel Co_3O_4 {111} surfaces are known experimentally to have lower reactivity towards CO compared to {100} and {110} surfaces.[15] Thus it would be expected that this surface termination would not improve the reactivity of the Co_3O_4 in the activation of Co FT catalyst under syngas. However, the presence of lattice O in this termination ($O–Co^t$) may be essential in facilitating the adsorption and dissociation of CO on the {111} surface, as described earlier.[6] The other surfaces observed on the Co_3O_4 nanoparticle (Figure 4.10 (b)) are the equivalent {113} surfaces, where one surface is terminated with an octahedral Co atomic later ($Co^o–OCo^t$) while the other surface is stepped. Flat and defective Co_3O_4 {113} surfaces have been previously observed experimentally[16]; however, there are limited reports on different possible surface terminations of {113} surfaces and their reactivity using DFT calculations. However, it is

generally reported that defective surfaces are more reactive than perfect surfaces.[4,5] A summary of the surface terminations of commonly observed and highly reactive Co_3O_4 surfaces is tabulated in Table 4.1.

4.4 Conclusions

In this chapter, the electron dose per frame of a focal series, required to restore the object wavefunction where both oxygen and cobalt atomic columns are resolved without visible beam-induced damage, was found to be 1188 e/Å^2. This dose was used to image and determine the theoretically known surface atomic active sites for CO, and H_2 adsorption from the restored phase of the Co_3O_4 EWR viewed along different projections. Contraction of the Co^o–O projected distance relative to the bulk due to surface relaxation was observed on a {100} surface viewed from the <110> projection. Of the Co_3O_4 surface terminations studied in this work, the {100} and {110} surfaces would have the highest reactivity towards CO due to the availability of surface lattice O atoms to form a triangular Co–C–O, and octahedral Co atoms. In contrast, the {115}, {112} and surfaces would be more reactive towards H_2 due to the Co–O bridge site at the surface terminations. Additionally, it would be expected that the defective surfaces ({110} and {113}) examined would be more reactive than perfect surfaces. Imaging the Co_3O_4 active surfaces is the first step towards studying the activation of Co_3O_4 under different gases in the next chapter.

4.5 References

(1) Khodakov, A. Y.; Chu, W.; Fongarland, P. *Chem. Rev.* **2007**, *107* (5), 1692–1744.

(2) Yu, R.; Hu, L. H.; Cheng, Z. Y.; Li, Y. D.; Ye, H. Q.; Zhu, J. *Phys. Rev. Lett.* **2010**, *105* (22), 226101.

(3) Xu, X.-L.; Chen, Z.-H.; Li, Y.; Chen, W.-K.; Li, J.-Q. *Surf. Sci.* **2009**, *603* (4), 653–658.

(4) Zhang, Y.-C.; Pan, L.; Lu, J.; Song, J.; Li, Z.; Zhang, X.; Wang, L.; Zou, J.-J. *Appl. Surf. Sci.* **2017**, *401*, 241–247.

(5) Lu, J.; Song, J.; Niu, H.; Pan, L.; Zhang, X.; Wang, L.; Zou, J.-J. *Appl. Surf. Sci.* **2016**, *371*, 61–66.

(6) Jiang, D. E.; Dai, S. *Phys. Chem. Chem. Phys.* **2011**, *13* (3), 978–984.

(7) Meyer, R. . R.; Kirkland, A. . I.; Saxton, W. . O. *Ultramicroscopy* **2002**, *92* (2), 89–109.

(8) Kirkland, A. I.; Meyer, R. R. *Microsc. Microanal.* **2004**, *10* (04), 401–413.

(9) Huang, C. Ultra high resolution imaging of radiation-sensitive materials, D.Phil. Thesis, University of Oxford, 2016.

(10) Kisielowski, C.; Frei, H.; Specht, P.; Sharp, I. D.; Haber, J. A.; Helveg, S. *Adv. Struct. Chem. Imaging* **2017**, *2* (1).

(11) Noguera, C. *J. Phys. Condens. Matter* **2000**, *12* (31), R367–R410.

(12) Zasada, F.; Piskorz, W.; Stelmachowski, P.; Kotarba, A.; Paul, J.-F. F.; Płociński, T.; Kurzydłowski, K. J.; Sojka, Z. *J. Phys. Chem. C* **2011**, *115* (14), 6423–6432.

(13) Montoya, A.; Haynes, B. S. *Chem. Phys. Lett.* **2011**, *502* (1–3), 63–68.

(14) Somorjai, G. A. *The Flexible Surface. Correlation between Reactivity and Restructuring Ability*; 1991; Vol. 7.

(15) Xie, X.; Li, Y.; Liu, Z. Q.; Haruta, M.; Shen, W. *Nature* **2009**, *458* (7239), 746–749.

(16) Zhou, H.; Kang, M.; Wu, D.; Lv, B. *CrystEngComm* **2016**, *18* (29), 5456–5462.

Chapter 5 : Activation of Co Fischer-Tropsch Catalysts under H_2 vs Syngas

5.1 Introduction

The atomic structure of the active surfaces of the Co_3O_4 Fischer-Tropsch (FT) precursor catalyst is described in the previous chapter (4). This chapter examines the reactivity of Co_3O_4 under different reducing gases for FT catalyst activation. As detailed in the literature review (Chapter 2, section 2.2), the effect of the reducing gas composition on the activation of Co_3O_4 has attracted substantial interest over the past decade.[1–4] This arises from the discovery that activating the catalyst under H_2 results in lower catalytic performance as opposed to activation with syngas.[1–5] However, the reason behind the difference in the catalytic performance between these two cases is not well understood but is generally ascribed to the Co crystallographic phase and valence state formed during activation.[2] Experimentally, the rapid oxidation of metallic Co in atmospheric air makes the characterisation of its physicochemical properties a challenge. As noted in chapter 3, section 3.5, electron energy loss spectroscopy (EELS) can be used to obtain information about the valence state of Co,[6] in which variations in the number of *d* electrons alter the L_3/L_2 peak intensity ratio of the Co-$L_{3,2}$ edge, the $L_{3,2}$ peak-to-peak energy separation, and the position of the L_3 peak, as well as the O-K pre-peak.[7–9] When carried out in conjunction with EELS, aberration-corrected scanning transmission electron microscopy (STEM) provides direct structural and chemical information at high spatial resolution. This chapter expands previous studies[10,11] of Co activation in FT synthesis by comparing, for the first time, catalyst activation under two different gaseous environments using both *ex-situ* and *in-situ* high-

resolution STEM-ADF and EELS to determine the most effective routes for the activation of Co where maximum reduction is achieved. In this chapter, *in-situ* studies provide a realistic picture of the effect of catalyst activation conditions without atmospheric air. At the same time, *ex-situ* analysis is required for understanding catalyst activation at near industrial-scale conditions (i.e. high pressures, flow rates & catalyst mass). The words '*activation*' and '*reduction*' in this chapter will be used interchangeably since the activation of catalyst in this context refers to the process of reduction.

5.2 Experimental

The *ex-situ* and *in-situ* activation reaction and characterisation of Co FT catalyst, including all imaging conditions, were performed as detailed in Chapter 3, section 3.5.3.

5.3 Results and Discussion

5.3.1 Thermodynamics of the Reduction of Co_3O_4

The reduction of Co_3O_4 to Co with H_2 follows a different reaction pathway to reduction with syngas due to the presence of CO in the syngas mixture. Temperature-programmed reduction (TPR) studies have shown that the reduction of Co_3O_4 with H_2 (eq. (1) in Table 5.1) is a two-step process comprising the conversion of Co_3O_4 to CoO (eq. (2), Table 5.1), followed by the conversion of CoO to Co (eq. (3), Table 5.1).[12] The former takes places between 250-350 °C, and the latter occurs between 500-600 °C.[12] This two-step mechanism arises because the direct conversion of Co_3O_4 to Co in H_2 is a very endergonic reaction (802.26 kJ/mol).[13,14]

In contrast, the reaction of Co_3O_4 with syngas is thermodynamically favoured compared to the reduction in H_2, and also involves several reaction steps with significantly lower free energies compared to H_2 activation (Table 5.1).[13,14] The first reaction (eq. (4)) is the formation of CoO (-29.4 kJ/mol), followed by the formation of Co_2C (eq. (5)) (13.9 kJ/mol), which finally decomposes to metallic Co (-16 kJ/mol) (eq. (6)). The advantage of syngas over H_2 activation is that the decomposition of Co_2C into Co (-16 kJ/mol, eq. (6)) occurs at a lower temperature (200-250 °C)[3] compared to the decomposition of CoO into Co (651.57 kJ/mol, eq. (3)) at 500-600 °C[12]. This allows the reduction of spinel Co_3O_4 to active metallic Co at lower temperatures (250-350 °C), which is essential in catalysis because it minimises particle sintering.[15] Additionally, syngas activation is often accompanied by a side-reaction (eq. (7), Table 5.1) in which carbon materials are formed from the disproportionation of CO.[16] However, the amount of carbon can be controlled by temperature since the equilibrium of this reaction shifts to the left with increasing temperature, to a point where the forward reaction becomes non-spontaneous above ~600 °C.[17]

Table 5.1. Thermodynamics of the reduction of Co_3O_4 with H_2 and syngas[13,14]

Hydrogen activation	ΔG^0_{298} (kJ/mol)	Syngas activation	ΔG^0_{298} (kJ/mol)
(1) $Co_3O_4(s)+4H_2(g)\leftrightarrow 3Co(s)+4H_2O(g)$	802.26	(4) $Co_3O_4(s)+CO(g)\leftrightarrow 3CoO(s)+CO_2(g)$	-29.4
(2) $Co_3O_4(s)+H_2(g)\leftrightarrow 3CoO(s)+H_2O(g)$	150.69	(5) $2CoO(s)+4CO(g)\leftrightarrow Co_2C(s)+3CO_2(g)$	13.9
(3) $3CoO(s)+3H_2(g)\leftrightarrow 3Co(s)+3H_2O(g)$	651.57	(6) $Co_2C(s)+2H_2(g)\leftrightarrow 2Co(s)+CH_4(g)$	-16
		(7) $2CO(g)\leftrightarrow CO_2(g)+C(s)$	-120.1

5.3.2 *Ex-situ* Activation of Co Fischer-Tropsch Synthesis Catalysts

As described in the previous section, there is a growth of carbon materials during catalyst activation depending on the gas, and this may modify the morphology of the catalyst system. In addition, the integrity (i.e. shape and strength) of the hollow carbon spheres (HCSs) support may be compromised during catalyst activation from the gasification of atomic carbon from the support into methane.[18] This results in the depletion of the support and subsequent particle sintering. Hence, it is essential to analyse the overall morphology of the catalyst system post-activation. Herein the overall morphology of activated catalyst system was investigated for the case of 350 °C *ex-situ* H_2 and syngas activation and compared to that of the starting Co_3O_4 precursor catalyst (Figure 5.1). It can be seen that the structure of the support HCSs remains mostly intact after 20 hrs of reduction at 350 °C (typical activation parameters for industrial FT Co catalyst guided by TPR of Co_3O_4[15]), for both the H_2 and syngas. This is positive because it indicates that the support withstands the activation conditions, which is essential in maintaining optimum catalytic performance.[19]

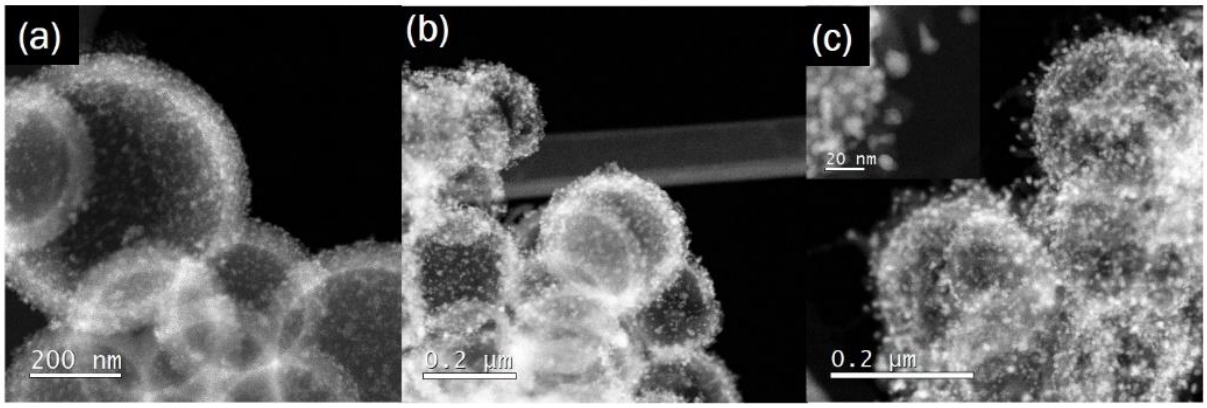

Figure 5.1. STEM-ADF images of FT catalyst morphology (a) before, and after 350 °C ex-situ activation in (b) H_2 and (c) syngas. For imaging conditions, refer to Chapter 3, section 3.5.3.

It is also observed that the syngas activated catalyst is encapsulated within carbon nanofibers (see insert in Figure 5.1 (c)) which are not found in the H_2 activated catalyst (Figure 5.1 (b)). This is expected from considerations of eq. (7) in Table 5.1, which indicates that the disproportionation of CO should take place in syngas and not in H_2. This side reaction may be advantageous to FT as it promotes the *in-situ* formation of a sinter resistant catalyst, where the active particles are held within the carbon fibres during FT synthesis.[16,20,21] Sinter resistance is vital in FT synthesis because the reaction typically runs over hundreds of hours in the catalytic reactor. However, it has also been suggested that the encapsulation of Co particles with carbon could lead to a deactivation of catalyst active sites through surface coverage with carbon and Co_2C formation at the catalyst surface.[22] However, this is typically observed in the reaction of Co_3O_4 with pure CO.[22] Additionally, carbon is known to have a weak metal-support interaction, and improved catalytic activity has been observed in syngas activated catalysts.[1–5]

In addition to changes in morphology, the oxidation state of Co also changes during the reduction process. Thus, the reducibility of these catalysts was investigated using EELS. Figure

5.2 compares the EELS spectra and elemental maps of single particles of as-prepared precursor Co_3O_4, H_2 reduced, and syngas reduced FT catalysts. The EELS spectra exhibit the typical O-K edge and Co-$L_{3,2}$ edge fine structure expected for cobalt oxide materials.[23,24] The former has two peaks, labelled α & β in Figure 5.2 (a). Peak α at ~530 eV corresponds to electronic transitions from O 1s states to hybridised O 2p−Co 3d states. Peak β at ~543 eV is typically a broad peak due to an unresolved shoulder and has been attributed to transitions from the O 1s state to O 2p−Co 3d, and O 2p−Co 3sp states.[9] The Co-$L_{3,2}$ edge fine structure consists of two white lines; the Co-L_3 peak (~778 eV), and the Co-L_2 peak (~794 eV) corresponding to transitions from $2p_{3/2}$ and $2p_{1/2}$ to unoccupied 3d states.[7]

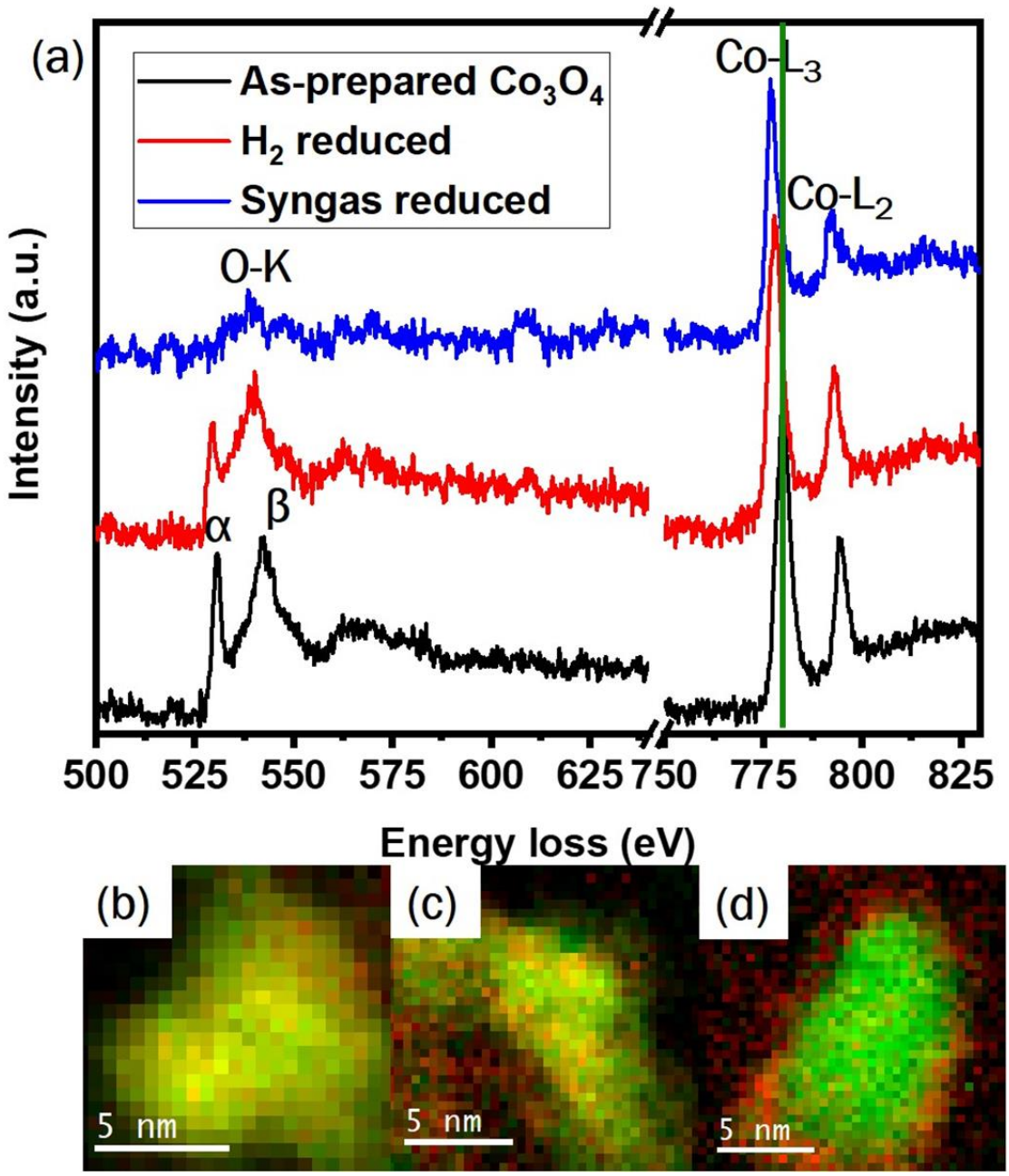

Figure 5.2. (a) The EELS spectra of as-prepared Co_3O_4 (black), H_2 (red), and syngas(blue) activated catalyst at 350 °C. (b), (c), and (d) are EELS elemental maps of as-prepared Co_3O_4, H_2 reduced, and syngas reduced Co respectively. Spectrum images were acquired using a 0.25 eV/ch dispersion with a pixel dwell time of 0.1 s and pixel size of 0.52 nm/pix, 0.4 nm/pix, and 0.42 nm/pix, respectively. Red and green regions represent the integrated O-K edge and Co-$L_{3,2}$ edge signals, respectively. A detailed experimental procedure is outlined in Chapter 3, section 3.5.3.

A visual evaluation of all the three EELS spectra in Figure 5.2 (a) reveals that the position of the Co-L_3 edge (~778 eV) is shifted to lower energy losses by at least ~3 eV in the activated catalysts' spectrum compared to the precursor Co_3O_4 spectrum. According to the previous reports[7], this is indicative of a decrease in the oxidation state of Co. This is positive as it indicates that both activation routes in Table 5.1 result in a reduction in the Co oxidation state as required. A decrease in the relative intensity of the O-K edge α peak (~530 eV) is also indicative of a reduced Co oxidation state.[9] Such a decrease in the relative intensity of the O-K edge α peak (~530 eV) can be observed on the activated catalysts' EELS O-K edge fine structure (Figure 5.2) when compared to the precursor Co_3O_4. However, the two activation methods (H_2 and syngas) need to be compared since the features of the EELS spectra (Figure 5.2 (a) H_2 and syngas reduced) of their catalyst particles are different, indicating different degrees of reduction.

For comparison between *ex-situ* H_2 and syngas activated catalysts, additional spectra were collected from different particles of the 350 °C reduced catalysts, and these are shown in Figure 5.3 (a). It is clear that features in the O-K edge fine structure (~ 530- 545 eV) from the H_2 activated catalyst (blue spectra) are more clearly defined showing a better-resolved α peak (~530 eV), and a stronger β peak (~543 eV) compared to syngas activated catalyst spectra (orange spectra). More specifically, the absence of the O-K edge α peak (~530 eV) and the overall diminished O-K edge signal from the syngas activated catalyst EELS spectra suggest that the catalyst is more reduced to a near metallic state compared to H_2 activated catalyst. This suggestion is confirmed by the more intense Co signal (green) in the elemental map from a syngas activated catalyst particle (Figure 5.2 (d)), compared to a more diffuse Co signal in the elemental map from a H_2 activated catalyst particle (Figure 5.2 (c)). This suggests better reducibility in syngas than in H_2. The reason(s) behind this will be discussed in relation to Table 5.1 subsequently.

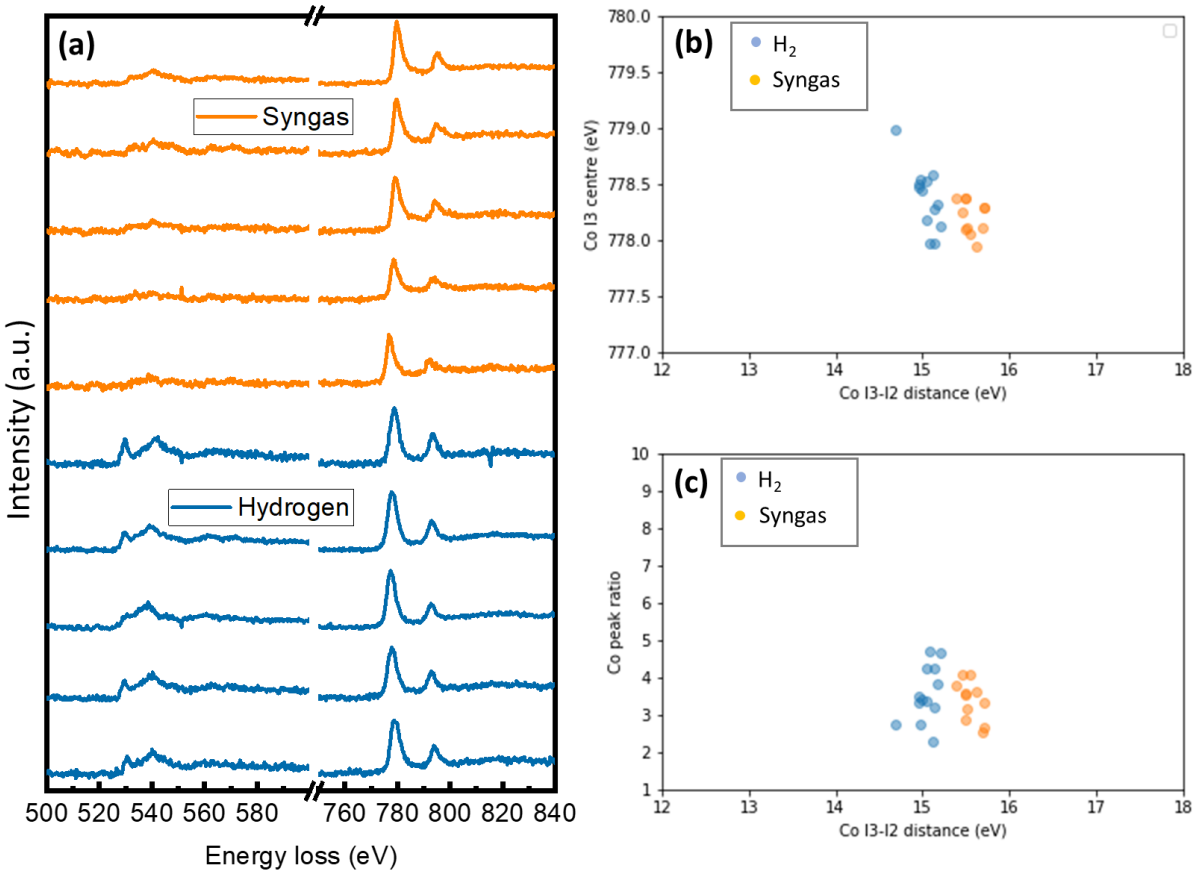

Figure 5.3. (a) The EELS spectra of 350 °C ex-situ syngas (orange spectra) and H_2 (blue spectra) activated catalyst particles. Each spectrum corresponds to a single particle of a H_2 (blue) or syngas (orange) activated catalyst. (b) & (c) Are the scatter plots of the Co L_3/L_2 intensity ratio vs Co L_3-L_2 distance and Co L_3 position vs Co L_3-L_2 distance, respectively, determined using ParticleSpy from single particle spectra of H_2 (blue) or syngas (orange) activated catalysts. Spectrum images were acquired using a 0.25 eV/ch dispersion with a pixel dwell time of 0.1 s.

For quantitative comparisons, the Co L_3/L_2 peak intensity ratio, Co L_3–L_2 peak-to-peak energy separation, and the Co-L_3 peak position values were extracted and plotted from multiple spectra (raw data) of H_2 and syngas activated catalysts using *ParticleSpy* script as described in Chapter 3, section 3.5.3, and are shown in Figure 5.3 (b) & (c). These three parameters (i.e. L_3/L_2, L_3-L_2 & L_3) are used together for improved quantification instead of using only the Co

L_3/L_2 ration as in the literature[25] because intensity measurements can suffer from errors due to inconsistent subtraction of the continuum background under the Co-L_2 peak.[26] The use of *ParticleSpy* script to extract the values from raw data eliminates human error arising from inconsistent background subtraction and peak intensity measurements. However, accurate peak fitting and data measurement using this script depends on the quality of the raw data (Figure 5.4) and in particular, noisy data, leads to less accurate peak fitting because the algorithm cannot distinguish signal from noise, as in Figure 5.4 (b), resulting in outliers in the scatter plots.

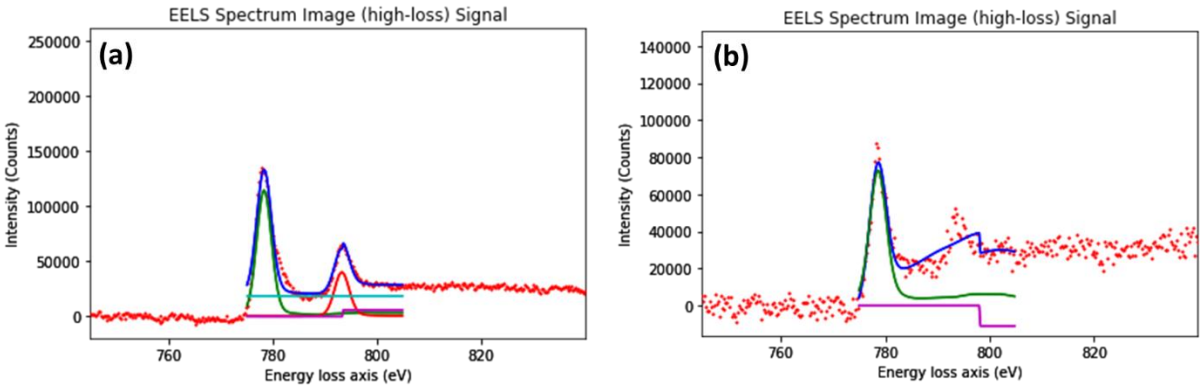

Figure 5.4. Example of an (a) acceptable peak fitting compared to (b) inaccurate peak fitting due to noisy EELS data on the ParticleSpy user interface. The dotted red curve is the raw data, the navy-blue curve is the Co-$L_{3,2}$ fit, cyan, and purple curves account for the continuum background. The green curve is the Co L_3 peak position. The red curve is the continuum background-subtracted Co L_2 edge.

It can be seen from the clear separation in the distribution of the data points on the scatter plots (Figure 5.3 (b) & (c)) that H_2 and syngas activated catalysts have different Co valence states. Specifically, the Co L_3–L_2 peak-to-peak energy separation for the H_2 activated catalyst EELS spectra (ave. 15.07 $\pm$0.02 eV) is smaller than the syngas activated Co L_3–L_2 peak-to-peak energy separation (ave. 15.7 $\pm$0.03 eV). Additionally, the Co-L_3 peak position on the syngas

activated catalyst EELS is slightly shifted to lower energy losses (ave. 778.0 ±0.07 eV) compared to the H_2 activated catalyst EELS spectra (ave. 778.3 ±0.06 eV) (Figure 5.3 (b)). According to the previous reports[7], this increase in the Co L_3–L_2 peak-to-peak energy separation accompanied by a shift in the Co-L_3 edge to lower energy losses is indicative of an increase in the number of *d* electrons (i.e. increasing reduction). This is also consistent with the observed Co L_3/L_2 ratio distributions where the average distribution of the EELS Co L_3/L_2 peak intensity ratio for H_2 activated catalyst is ~ 3.9 ±0.18 while that of syngas activated catalyst is 3.4 ±0.16.

For quantitative comparison, the EELS spectra from standard Co samples (Figure 5.5 & Table 5.2) with known oxidation states were acquired and compared to the experimental data from the catalyst samples. However, a metallic Co standard sample was not measured since Co readily oxidises in air and is thus unavailable as a pure (i.e. unoxidised/unpassivated) commercial sample. Instead, the data were compared with literature values for metallic Co reduced *in-situ*.[6] It has been shown that the linear relationship between the number of *d* electrons and Co-$L_{3,2}$ edge parameters (i.e. L_3/L_2, L_3-L_2 & L_3) is only valid for metal oxides.[6,27] For example, the literature reported values for L_3/L_2 ratios for Co, CoO, and Co_3O_4 are 3.15, 4.51, and 2.42, respectively.[6] The Co-L_3/L_2 intensity ratio of the standard CoO sample (4.51) in Table 5.2 was found to be closest to that of the H_2 activated catalyst Co-L_3/L_2 intensity ratio (3.9 ±0.18), suggesting that these catalyst particles are mostly Co^{2+}. In contrast, the Co-L_3/L_2 intensity ratio of the syngas activated catalyst (3.4±0.16) is closer to the ratio (3.15) observed from *in-situ* reduced metallic Co.[6] The difference (~0.4) in the measured average Co L_3/L_2 ratio of the catalysts from the standard Co L_3/L_2 ratios might result from mixed Co valence states from surface re-oxidation of the catalyst particles in the air.

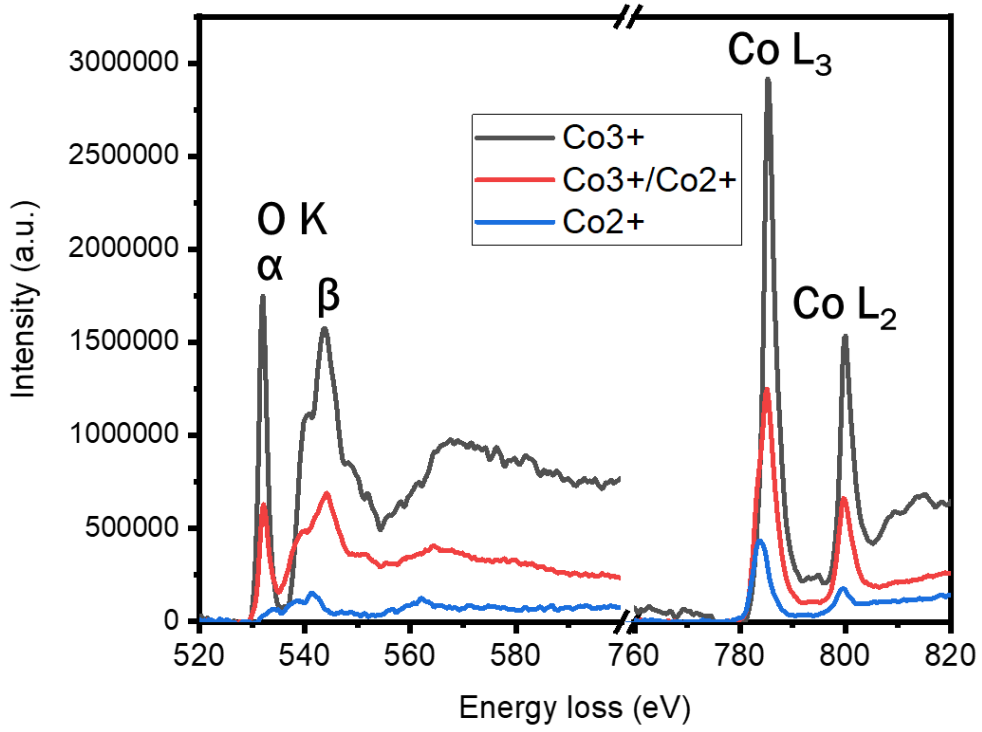

Figure 5.5.The EELS spectra of Co standards of known oxidation states.

Table 5.2. Data obtained from the EELS spectra of Co standards with known oxidation states in Figure 5.5.

Spectra	L_3/L_2	L_3–L_2 (eV)	Co–L_3 (eV)
Co^{3+}	2.29	14.5	780.3
Co^{3+}/Co^{2+}	2.40	14.75	779.6
Co^{2+}	4.51	15.75	778.4

In addition to EELS, high-resolution STEM-ADF imaging was performed to investigate the differences in the atomic structure of the syngas and H_2 activated catalysts associated with the observed differences in Co oxidation states. Figures 5.6 (a)-(e) show high-resolution STEM-ADF images of syngas (a)-(c) and H_2 (d) & (e) activated catalysts. Some of the catalyst

nanoparticles reduced at 350 °C in syngas have a twin boundary consistent with <111> fcc metallic Co (see power spectrum insert in Figure 5.6 (a)).

The crystal structure of the twin boundary follows the stacking sequence of a reversed {111} surface (i.e. ABC**A**CBA) due to the symmetrically mirrored <111> fcc Co grains (Figure 5.6 (b)). More specifically, the doubled {022} reflections (labelled in a yellow box and circle in Figure 5.6 (b) insert) in the power spectrum result from two overlapping single-crystals of <111> fcc Co mirrored at a 138.5° twin boundary angle (Figure 5.6 (b)). Previous reports[28–30], indicate that these are typical features of 111-type twin boundaries found in fcc transition metals. Twin boundaries are essential defects in catalysis since they typically have higher adsorption energies in comparison to flat facets and are stable during chemical reactions.[31,32] For example, it has been shown that CO molecules adsorb more strongly on an fcc twin boundary compared to a flat crystal plane.[31]

Other syngas activated catalyst particles have a core-shell structure, with a metallic Co core and a metal oxide shell (Figure 5.6 (c)), consistent with a surface re-oxidation of metallic Co. In contrast, a catalyst activated in H_2 at 350 °C show faceted hexagonal particles (Figure 5.6 (d) & (e)). Examination of the power spectrum (Figure 5.6 (d) insert) and the measured 2.6 Å interplanar spacing consistent with {111} planes in CoO is consistent with a typical <110> rock-salt structure that is characteristic of CoO particles enclosed with {111} facets (Figure 5.6 (d)). These are typically less active for FT synthesis since they contain Co atoms in the 2+ state and not active metallic Co atoms.

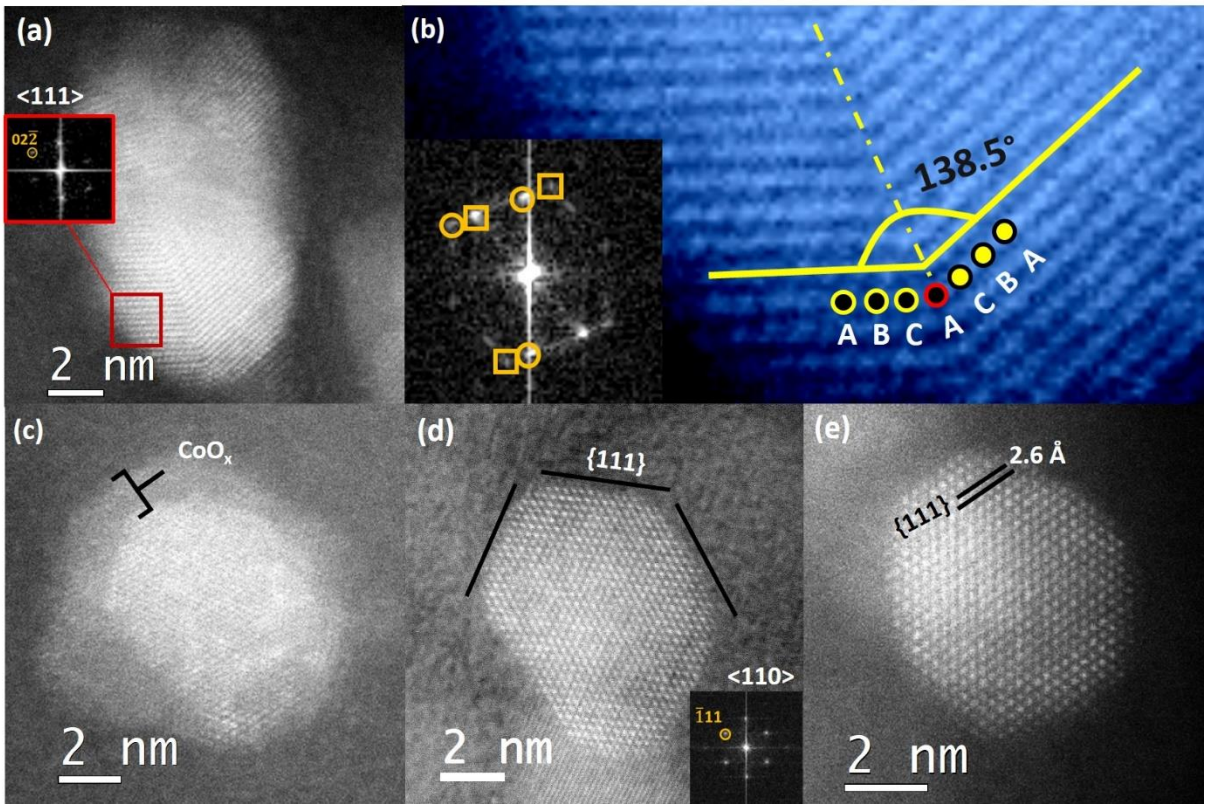

*Figure 5.6. High-resolution STEM ADF images of (a)-(c) 350 °C syngas activated Co FT catalyst particles, and (d)-(e) H_2 activated catalyst particles. (b) Magnified, false-colour STEM-ADF image of the twin boundary of the particle in (a) showing the 138.5° boundary angle and the atomic stacking sequence of a reversed {111} surface (i.e. ABC**A**CBA). Inserts in (a), (b) & (d) show the power spectrum of <111> fcc Co, the doubled {022} reflections (labelled in a yellow box and circle) in the power spectrum resulting from two overlapping single-crystals of <111> fcc Co mirrored at a 138.5° twin boundary angle, and <110> CoO projection, respectively.*

Further considering Table 5.1, it is necessary to reconcile the above differences in the Co oxidation states and crystal structure of catalysts activated in H_2 and syngas with the reactions of these gases with Co_3O_4. Firstly, all reactions of syngas with Co_3O_4 to obtain metallic Co are more energetically favoured than H_2 reactions with Co_3O_4. Secondly, the presence of CO in syngas seem to play a critical role in the conversion of Co_3O_4 to metallic Co. Specifically, the synergistic combination of CO and H_2 in syngas results in the formation of Co_2C from CO (Eq. (5) Table 5.1), which spontaneously (-16 kJ/mol) decomposes into metallic Co in H_2 (Eq. (6)

Table 5.1). This synergistic effect is not found in H_2 activation. As a result, better reducibility is achieved with syngas than H_2, and previous studies have also shown that the reduction of Co_3O_4 in H_2 does not achieve full reduction at 350 °C.[3,10] Meanwhile, other studies on the activation of spinel Co_3O_4 under sequential CO and H_2 treatment have shown that activation involves the formation of cobalt carbide (Co_2C), which subsequently decomposes to metallic Co in H_2 at 220 °C.[2,33] Hence, the presence of CO in syngas for activation of Co FT catalyst is crucial in achieving full reduction at 350 °C.

However, the activated catalysts still suffer from re-oxidation in the air during specimen loading and transfer to the microscope. This reaction is spontaneous (-802.26 kJ/mol, reverse reaction eq. (1), Table 5.1). It may occur rapidly as evidenced by the presence of an O-K edge in the syngas activated catalyst EELS spectra (Figure 5.3 (a)) and the oxide shell on the catalyst particle (Figure 5.6 (c)). In contrast, the absence of an oxide shell around the H_2 activated catalyst particles (Figure 5.6 (d) & (e)) suggest that CoO is not as sensitive to oxidation compared to metallic Co. This is expected since the free energy for the oxidation of Co (eq. (1), Table 5.1) is five-times higher than that for the oxidation of CoO (eq. (2), Table 5.1). The primary issue with this re-oxidation is that it prevents accurate quantification of Co valence state because the resulting Co EELS fine structure parameters (i.e. L_3/L_2, L_3-L_2 & L_3) used for quantification may be a combination of the surface oxidised Co and core Co, as discussed earlier.

To understand this surface re-oxidation better, elemental maps of syngas and H_2 activated catalyst particles as presented earlier Figure 5.2 (c) & (d) were used to compare the distribution of O and Co signals on the activated catalyst particles (Figures 5.7 (a)-(d) & 5.8 (a)-(d)). The EELS spectra were integrated from the core and shell of the catalyst particles for evaluating the re-oxidation by comparing their O-K edge fine structure features (Figures 5.7 (e) & 5.8 (e)).

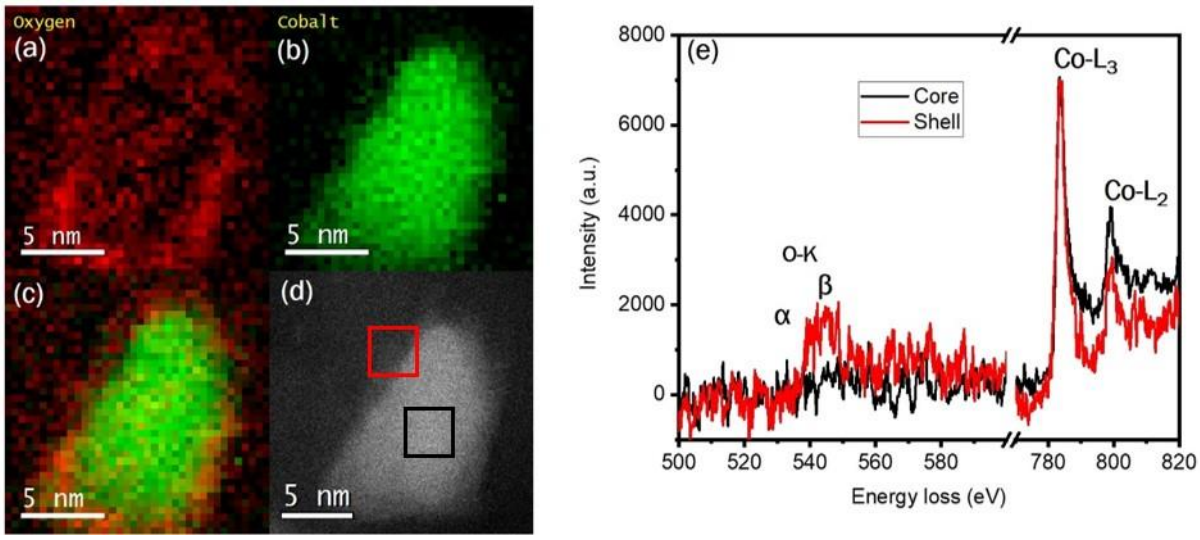

Figure 5.7. The EELS elemental maps and spectra of syngas reduced Co FT catalyst. (a) O–K edge signal, (b) Co–$L_{3,2}$ edge signal, (c) composite O–K and Co–$L_{3,2}$ signal, and (d) STEM-ADF survey image. (e) Particle core and shell EELS spectra. The spectrum image was acquired using a 0.25 eV/ch dispersion with a pixel dwell time of 0.1 s and pixel size 0.42 nm/pix. The core (black square) and shell (red square) EELS spectra were integrated over 72 and 144 pixels, respectively.

For syngas reduction at 350 °C, both O (Figure 5.7 (a)) and the Co (Figure 5.7 (b)) signals are spatially localised, with the Co signal concentrated in the bulk of the catalyst and the oxygen only present at the surface (Figure 5.7 (c)). The latter confirms that re-oxidation of Co occurs at the surface of the catalyst particles. Given that the full conversion of Co_3O_4 to metallic Co under syngas activation is thermodynamically favoured (Table 5.1), and expected to occur at lower temperatures than 350 °C, [23,24,34,35] the residual O at the surface is most likely due to a re-oxidation of the catalyst following exposure to atmospheric air for example during specimen loading into the microscope. Further evidence of particle surface re-oxidation is provided by the absence of O-K edge features (~530-545 eV) in the EELS spectrum (Figure 5.7 (e), black curve) integrated over 72 pixels from the particle core (i.e. the region labelled in a black square

in Figure 5.7 (d)). In contrast, the EELS spectrum integrated over 144 pixels from the particle shell (region labelled in a red square in Figure 5.7 (d)) show the presence of O–K edge fine features (peak β at ~543 eV) consistent with CoO due to the absence of the pre-peak 'α' at ~530 eV. Hence, the overall valence state distribution in this catalyst would include surface Co^{2+}, which does not result from syngas activation.

In the case of H_2 activation at 350 °C, the O (Figure 5.8 (a)) and Co (Figure 5.8 (b)) signals are more evenly distributed, as displayed in the composite elemental map (Figure 5.8 (c)), compared to syngas (Figure 5.7 (c)). The even distribution of the signals suggests that O is coordinated to Co in a majority CoO state. In addition, as was discussed earlier relation to Table 5.1 H_2 activation at 350 °C does not fully convert Co_3O_4 to metallic Co but leads to CoO. It is therefore not straightforward to distinguish the O signal due to re-oxidation from the O signal due to incomplete reduction in this case. However, the O–K edge fine structure of the EELS spectra extracted from the core and shell (integrated over 30 and 56 pixels from the regions labelled in black and red squares in Figure 5.8 (d), respectively) of the nanoparticle (Figure 5.8 (e)) have similar features, except that the pre-peak 'α' (~530 eV) in the 'shell' spectrum is more relatively intense, resembling that from Co in spinel form. This indicates a higher Co oxidation state at the particle surface relative to the core, most like due to re-oxidation during specimen transfer.

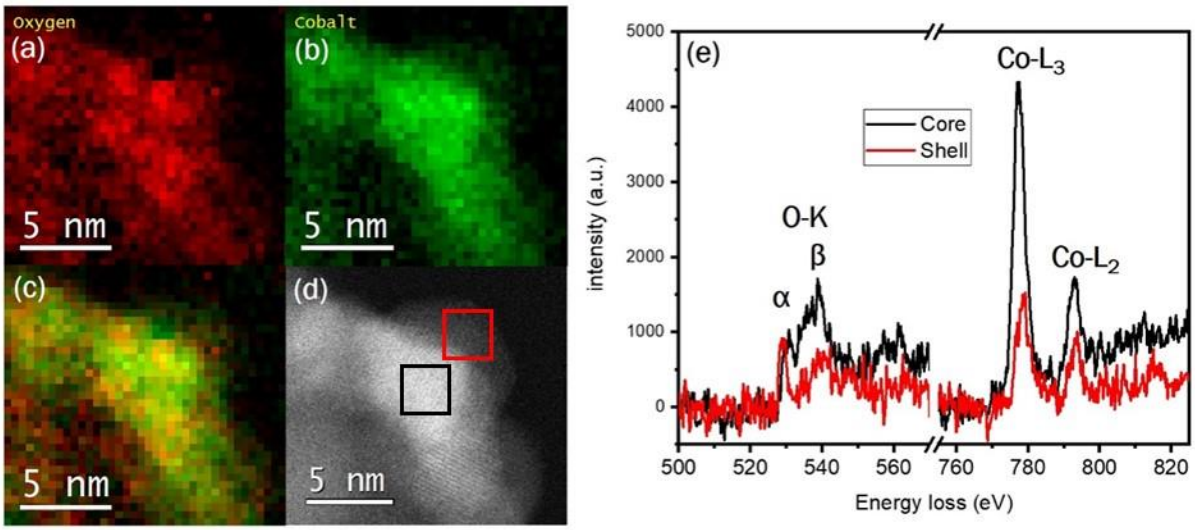

Figure 5.8. The EELS elemental maps and spectra of H_2 reduced Co FT catalyst. (a) O–K edge signal, (b) Co–$L_{3,2}$ edge signal, (c) composite O–K and Co–$L_{3,2}$ signal, and (d) STEM-ADF survey image. (e) Particle core and shell EELS spectra. The spectrum image was acquired using a 0.25 eV/ch dispersion with a pixel dwell time of 0.1 s and pixel size 0.4 nm/pix. The core (black square) and shell (red square) EELS spectra were integrated over 30 and 56 pixels, respectively.

In order to deconvolve the O signal due to re-oxidation from that due to incomplete reduction, the activation temperature was increased to 600 °C to drive the conversion of CoO to Co (eq. (3), Table 5.1). In that way, the O signal due to incomplete reduction would be eliminated, as, according to TPR[12], this is the temperature required to obtain metallic Co in H_2. The relevant EELS data is shown in Figure 5.9 (a)-(c). The catalyst activated under H_2 is now almost entirely reduced, with the average distribution of the Co-L_3 edge (~778.5 eV), the L_3-L_2 peak-to-peak energy separation (~15.2 eV), and the Co-L_3/L_2 intensity ratio (~3.5) on the scatter plots (Figure 5.9 (b) & (c)) comparable to that of syngas activated catalyst (~778.1 eV, ~15.0 eV, ~3.0, respectively). The outliers (data points at ~783 eV) in Figure 5.9 (c) are as a result of inaccurate Co-L_3 peak fitting in *ParticleSpy* due to noisy data, as discussed earlier (Figure 5.4). The values of the Co-L_3/L_2 intensity ratio closely resembles previously reported metallic Co

L_3/L_2 intensity ratio.[6] However, the presence of the β peak (~543 eV) on the O-K edge fine structure of both H_2 and syngas activated catalysts (Figure 5.9 (a)) indicates the presence of Co^{2+} on the catalyst particles. This Co^{2+} is due to the re-oxidation of Co to CoO during sample transfer to the microscope, because thermodynamically, only metallic Co is expected at 600 °C.

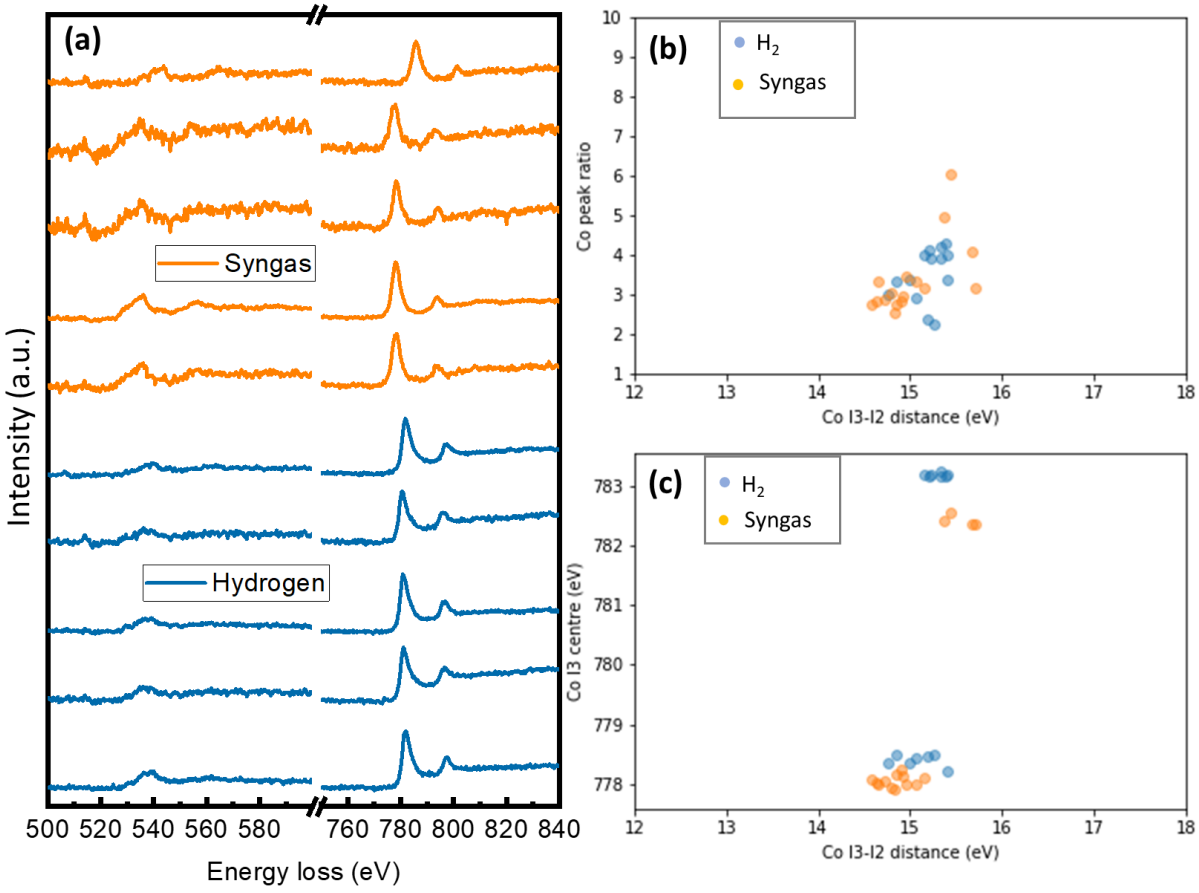

Figure 5.9. (a) The EELS spectra of 600 °C ex-situ syngas (orange spectra) and H_2 (blue spectra) activated catalyst particles. Each spectrum corresponds to a single particle of a H_2 (blue) or syngas (orange) activated catalyst. (b) & (c) Are the scatter plots of the Co L_3/L_2 intensity ratio vs Co L_3-L_2 distance and Co L_3 position vs Co L_3-L_2 distance, respectively, determined using ParticleSpy from single particle spectra of H_2 (blue) or syngas (orange) activated catalysts. Spectrum images were acquired using a 0.25 eV/ch dispersion with a pixel dwell time of 0.1 s.

The re-oxidised particle shell is visible in the high-resolution STEM-ADF images of both H_2 and syngas activated catalysts (Figure 5.10). However, some syngas activated catalyst particles also have a graphitic carbon shell (labelled by the orange arrow in Figure 5.10 (b)) from the high-temperature graphitisation of the carbon fibres formed from the disproportionation of CO at a lower temperature during ramping to 600 °C. This is the most likely scenario because the disproportionation of CO becomes non-spontaneous above ~600 °C.[17] Both the H_2 and syngas activated catalyst particles (Figure 5.10 (a) & (c)) exhibit a typical <110> fcc Co structure confirmed by the power spectra and a 2.1 Å interplanar spacing between the {111} planes. High-resolution imaging also revealed the presence of stacking faults on {111} planes (yellow box in Figure 5.10 (c)) in the H_2 activated catalyst particle as commonly observed in fcc metals after high-temperature treatment.[28–30] These are confirmed by double reflections/streaking in the power spectrum (see insert in Figure 5.10 (c)). It is hence clear that in order to achieve a complete reduction of the Co FT catalyst, the catalyst must be activated at high temperatures if the gas is H_2 or at lower temperatures if the gas is syngas. However, activation at 600 °C is not suitable for industrial FT catalysis due to particle sintering at high temperatures (Figure 5.11), which leads to loss of active surface area and lower activity.

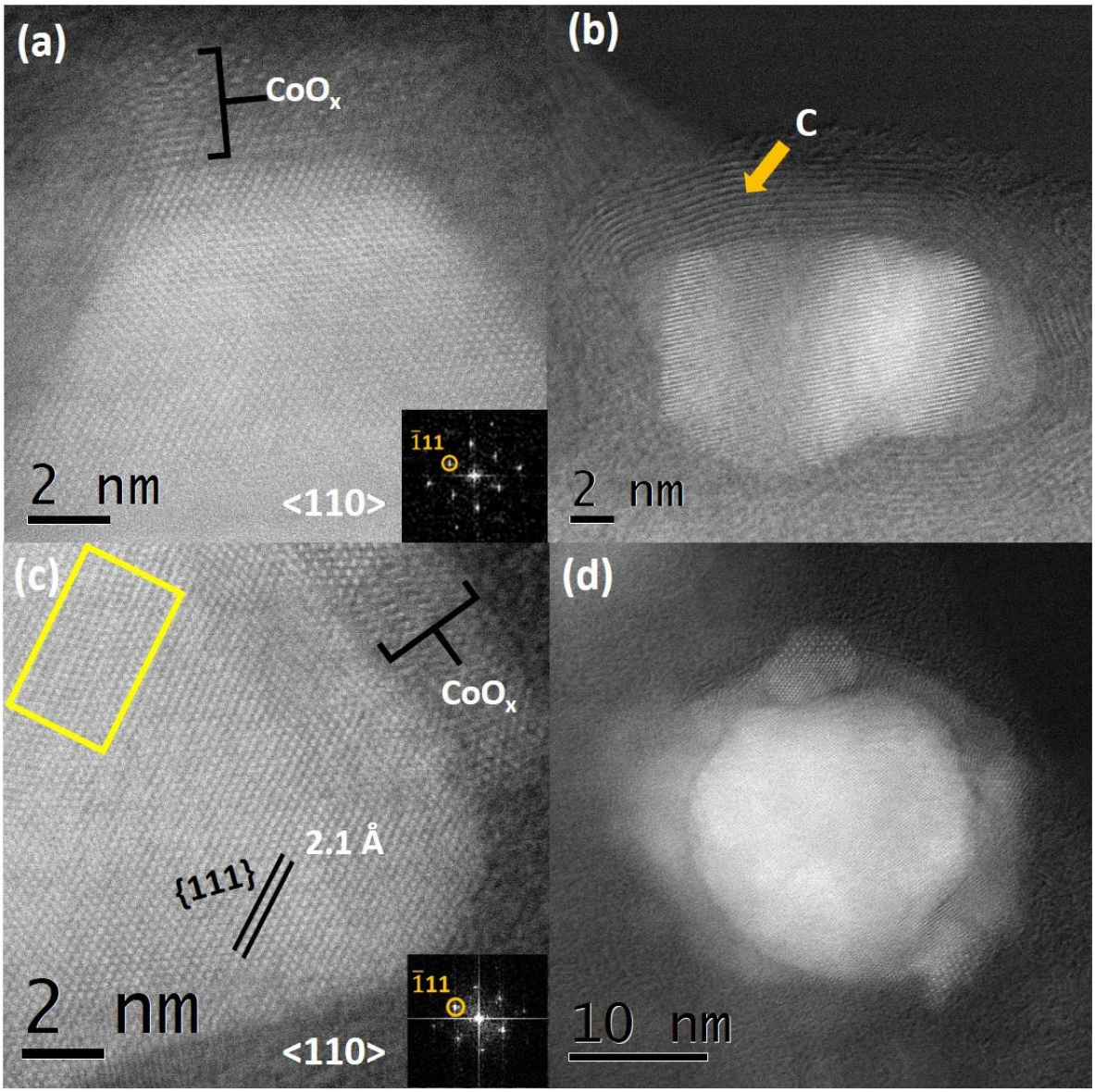

Figure 5.10. High-resolution STEM-ADF images of 600 °C ex-situ (a)-(b) syngas and (c)-(d) H_2 activated catalyst particles. Inserts in (a) & (c) are power spectra of <110> fcc Co.

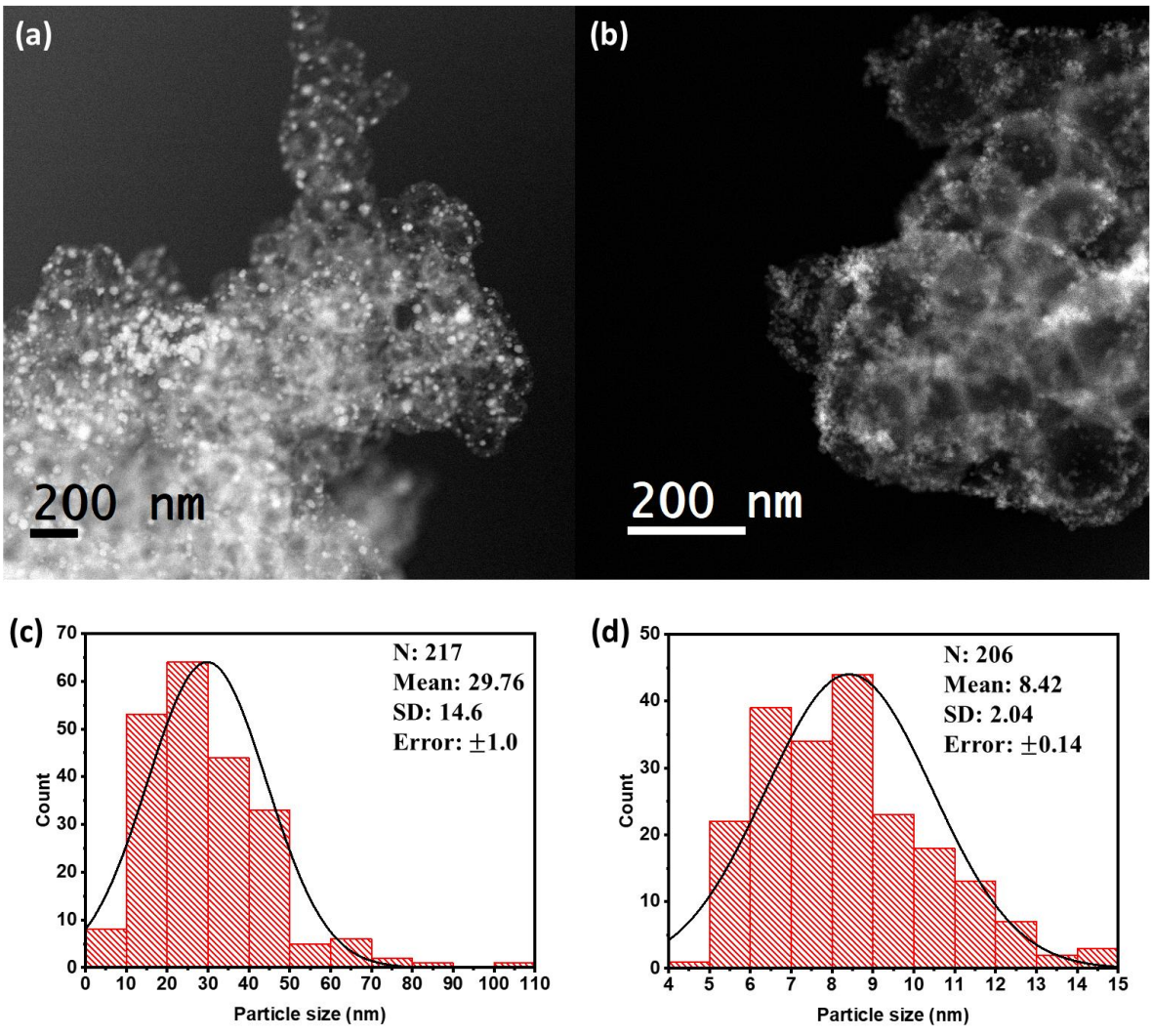

Figure 5.11. STEM-ADF images of 600 °C ex-situ (a) H_2 and (b) syngas activated Co FT catalysts, and their respective average particle size distribution, (c) H_2 and (d) syngas.

5.3.3 *In-situ* Activation of Co Fischer-Tropsch Catalysts

Increasing the reduction temperature may solve the incomplete reduction, as shown above, but not the surface re-oxidation due to exposure to air. However, industrial activation of Co FT catalysts takes place in the absence of atmospheric air, where the sample is activated in a sealed fixed bed FT reactor, followed by FT synthesis.[36] Hence, to obtain a near reaction representation of the effect of activation conditions on the Co FT catalyst, *in-situ* reduction of

the spinel Co_3O_4 supported on hollow carbon spheres under H_2 and syngas at 350 °C was performed (Figure 5.12).

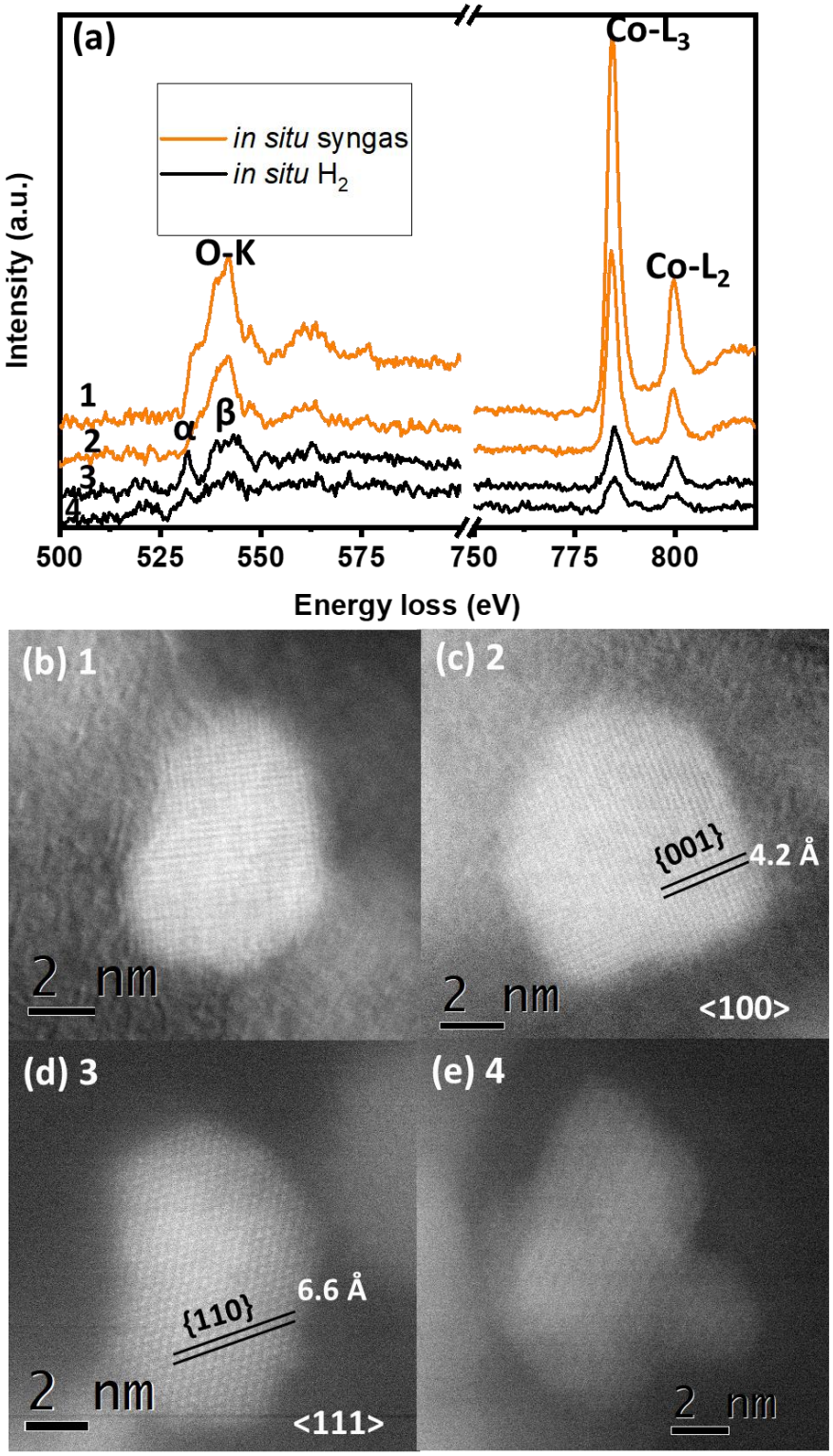

Figure 5.12. (a) The EELS spectra of 350 °C in-situ syngas (orange spectra) and H_2 (black spectra) activated catalyst particles. (b)-(c) STEM-ADF images of syngas reduced catalyst, (d)-(e) STEM ADF images of H_2 reduced

catalyst. Spectra 1-4 corresponds to STEM ADF images (b)-(e), respectively. The analysis was performed at 500 mbar and 350 °C.

The O-K edge fine structure of the *in-situ* H_2 reduced (black, Figure 5.12 (a)) Co FT catalyst is different from that of the *in-situ* syngas reduced (orange, Figure 5.12 (a)) catalyst in that the relative intensity of the pre-peak 'α' is higher in the H_2 reduced material and is only present as a shoulder in the syngas reduction spectrum. Furthermore, the onset of the Co-L_3 peak of the *in-situ* syngas spectrum is slightly shifted to lower energy loss. As described earlier, an intense O-K edge pre-peak (~530 eV) and a higher energy loss shifted Co-L_3 edge is associated with an increase in Co oxidation state. This, therefore, suggests that the Co catalyst activated under H_2 has a higher oxidation state than the Co catalyst activated under syngas. To support this, the high-resolution STEM-ADF image of syngas activated catalyst particles exhibit an interplanar spacing of 4.2 Å consistent with the {001} planes of CoO (Figure 5.12 (c)). In contrast, the high-resolution STEM-ADF image of H_2 activated catalyst particle shows an interplanar spacing of 6.6 Å consistent with {110} planes of Co_3O_4 (Figure 5.12 (d)). The absence of contrast from the oxidised shell on the catalyst particles (Figure 5.12 (b)-(e)) confirms that the observed core-shell structures from *ex-situ* activation are a consequence of re-oxidation in atmospheric air and not the true activation product.

These *in-situ* and *ex-situ* data suggest that syngas achieves a better degree of reduction at an industrially relevant FT reduction temperature (350 °C) than H_2, and both *in-situ* and *ex-situ* data are in agreement. However, the *in-situ* experiment for syngas did not achieve full reduction due to the shorter reaction time (2hrs vs 20 hrs) compared to the *ex-situ* experiments due to the impracticality (i.e. possible chip damage over time etc.) of running a 20 hrs *in-situ* gas-phase reaction in a microscope.

5.3.4 Implications to Fischer-Tropsch synthesis

As discussed in the introduction and literature review (Chapter 2, section 2.2), the activation of Co FT catalysts under different gaseous atmospheres has a direct influence on the catalytic performance of the catalyst.[1–5] Specifically, Co catalysts activated in syngas show a higher CO conversion compared to catalysts activated in H_2. This chapter investigated the differences in the properties of the catalysts activated in syngas and H_2, to better explain the observed differences in the catalytic performance reported in literature. The two main reasons for the differences in the catalytic performance are proposed in this study: Firstly, the EELS data (Figure 5.2) revealed better reducibility in syngas compared to H_2; where the active metallic Co is achieved in syngas, and CoO is obtained in H_2. It is well documented that Co is active for FT synthesis in its metallic state[15], thus, the unavailability of active metallic Co sites in H_2 activated catalyst could explain the observed inferior catalytic performance in contrast to syngas activated catalysts. Secondly, one of the reasons for the loss of activity during FT synthesis is particle sintering. The examination of the morphology of the activated catalysts (Figure 5.1) revealed the encapsulation of Co particles within carbon fibres in the syngas activated catalyst. Therefore, it is proposed that this carbon fibre encapsulation may provide sinter resistance during FT synthesis, thus, allowing the catalyst to maintain optimum performance for hours without the loss of activity due to sintering. In contrast, the encapsulation of catalyst particles is not observed in H_2 activation due to the absence of CO to undergo disproportionation. To support this, the activation of Co FT catalysts at 600 °C resulted in severe sintering for H_2 compared to syngas activated catalyst due to the absence of sinter resistance in H_2 (Figure 5.11). Therefore, these reasons could be the answers to the effect of reducing gas composition on the FT synthesis.

5.4 Conclusions

The effect of reducing gas atmosphere on the activation of Co FT catalysts using STEM-ADF and EELS was studied *ex-situ* and *in-situ*. At 350 °C, *ex-situ* H_2 activation produced mainly CoO (Co^{2+} oxidation state) catalyst particles enclosed with {111} facets. In contrast, activation in syngas produced twinned fcc Co particles encapsulated in carbon fibres, and core-shell particles, with a metallic Co core and a CoO shell. The oxidised shell was determined to arise as a consequence of exposure to atmospheric air during sample transfer. Increasing the activation temperature to 600 °C helped to drive the complete reduction of CoO to active metallic Co in H_2, and the graphitisation of carbon fibres in syngas, but the observed disadvantage of high-temperature activation is particle sintering. *In-situ* reduction in H_2 and syngas showed the absence of an oxide shell on the particles, confirming the re-oxidation of Co catalyst during sample transport. Overall, syngas activation is the most effective method in order to obtain an active metallic Co sinter resistant catalyst at lower temperatures.

5.6 References

(1) de la Peña O'Shea, V. A.; Campos-Martín, J. M.; Fierro, J. L. G. *Catal. Commun.* **2004**, *5* (10), 635–638.

(2) Gnanamani, M. K.; Jacobs, G.; Shafer, W. D.; Davis, B. H. *Catal. Today* **2013**, *215*, 13–17.

(3) Ducreux, O.; Rebours, B.; Lynch, J.; Roy-Auberger, M.; Bazin, D. *Oil Gas Sci. Technol. - Rev. l'IFP* **2009**, *64* (1), 49–62.

(4) de la Peña O'Shea, V. A.; Homs, N.; Fierro, J. L. G.; Ramírez de la Piscina, P. *Catal. Today* **2006**, *114* (4 SPEC. ISS.), 422–427.

(5) Dehghan, R.; Hansen, T. W.; Wagner, J. B.; Holmen, A.; Rytter, E.; Borg, Ø.; Walmsley, J. C. *Catal. Letters* **2011**, *141* (6), 754–761.

(6) Zhao, Y.; Feltes, T. E.; Regalbuto, J. R.; Meyer, R. J.; Klie, R. F. *J. Appl. Phys.* **2010**, *108* (6), 063704.

(7) Pearson, D. H.; Ahn, C. C.; Fultz, B. *Phys. Rev. B* **1993**, *47* (14), 8471–8478.

(8) Grunes, L. A.; Leapman, R. D.; Wilker, C. N.; Hoffmann, R.; Kunz, A. B. *Phys. Rev. B* **1982**, *25* (12), 7157–7173.

(9) Suntivich, J.; Hong, W. T.; Lee, Y. L.; Rondinelli, J. M.; Yang, W.; Goodenough, J. B.; Dabrowski, B.; Freeland, J. W.; Shao-Horn, Y. *J. Phys. Chem. C* **2014**, *118* (4), 1856–1863.

(10) Braconnier, L.; Landrivon, E.; Clémençon, I.; Legens, C.; Diehl, F.; Schuurman, Y. *Catal. Today* **2013**, *215*, 18–23.

(11) Ward, M. R.; Boyes, E. D.; Gai, P. L. *ChemCatChem* **2013**, *5* (9), 2655–2661.

(12) Paryjczak, T.; Rynkowski, J.; Karski, S. *J. Chromatogr. A* **1980**, *188* (1), 254–256.

(13) Chase, M. W.; Curnutt, J. L.; Downey, J. R.; Mcdonald, R. A.; Syverud, A. N.; Valenzuela, E. A. *J. Phys. Chem. Ref. Data* **1982**, *11* (3), 695–940.

(14) Pankratz, L. B. *Thermodynamic properties of elements and oxides*; Washington D.C., 1982.

(15) Khodakov, A. Y.; Chu, W.; Fongarland, P. *Chem. Rev.* **2007**, *107* (5), 1692–1744.

(16) Bremmer, G. M.; Zacharaki, E.; Sjåstad, A. O.; Navarro, V.; Frenken, J. W. M.;

Kooyman, P. J. *Faraday Discuss.* **2017**, *197* (0), 337–351.

(17) Treptow, R. S.; Jean, L. *J. Chem. Educ.* **1998**, *75* (1), 43.

(18) Li, S.; Pasc, A.; Fierro, V.; Celzard, A. *Journal of Materials Chemistry A*. Royal Society of Chemistry August 17, 2016, pp 12686–12713.

(19) Tsakoumis, N. E.; Rønning, M.; Borg, Ø.; Rytter, E.; Holmen, A. *Catal. Today* **2010**, *154* (3–4), 162–182.

(20) Phaahlamohlaka, T. N.; Dlamini, M. W.; Mogodi, M. W.; Kumi, D. O.; Jewell, L. L.; Billing, D. G.; Coville, N. J. *Appl. Catal. A Gen.* **2018**, *552*, 129–137.

(21) Aydin, C.; Lu, J.; Browning, N. D.; Gates, B. C. *Angew. Chemie* **2012**, *124* (24), 6031–6036.

(22) Dembélé, K.; Bahri, M.; Melinte, G.; Hirlimann, C.; Berliet, A.; Maury, S.; Gay, A.-S.; Ersen, O. *ChemCatChem* **2018**, *10* (18), 4004–4009.

(23) Wang, Z. L.; Bentley, J.; Evans, N. D. *Micron* **2000**, *31* (4), 355–362.

(24) Wang, Z. L.; Yin, J. S.; Jiang, Y. D. *Micron* **2000**, *31* (5), 571–580.

(25) Cosandey, F.; Su, D.; Sina, M.; Pereira, N.; Amatucci, G. G. *Micron* **2012**, *43* (1), 22–29.

(26) Riedl, T.; Gemming, T.; Wetzig, K. *Ultramicroscopy* **2006**, *106* (4–5), 284–291.

(27) Leapman, R. D.; Grunes, L. A. *Phys. Rev. Lett.* **1980**, *45* (5), 397–401.

(28) Gontard, L. C.; Dunin-Borkowski, R. E.; Gass, M. H.; Bleloch, A. L.; Ozkaya, D. *J. Electron Microsc. (Tokyo).* **2009**, *58* (3), 167–174.

(29) Clarebrough, L. M.; Forwood, C. T. *Phys. Status Solidi* **1976**, *33* (1), 355–366.

(30) Ino, S.; Ogawa, S.; Taoka, T.; Akahori, H. *Japanese J. Appl. Physics, Part 1 Regul. Pap. Short Notes Rev. Pap.* **1972**, *11* (12), 1859.

(31) Tang, C.; Shi, J.; Bai, X.; Hu, A.; Xuan, N.; Yue, Y.; Ye, T.; Liu, B.; Li, P.; Zhuang, P.; Shen, J.; Liu, Y.; Sun, Z. *ACS Catal.* **2020**, *10* (3), 2026–2032.

(32) Wilms, M.; Broekmann, P.; Kruft, M.; Stuhlmann, C.; Wandelt, K. *Appl. Phys. A* **1998**, *66*, 473–475.

(33) Kwak, G.; Kim, D.-E.; Kim, Y. T.; Park, H.-G.; Kang, S. C.; Ha, K.-S.; Jun, K.-W.; Lee, Y.-J. *Catal. Sci. Technol.* **2016**, *6* (12), 4594–4600.

(34) du Plessis, H. E.; de Villiers, J. P. R.; Tuling, A.; Olivier, E. J. *Phys. Chem. Chem. Phys.* **2016**, *18* (43), 30183–30188.

(35) Wang, Z. L.; Bentley, J.; Evans, N. D. *J. Phys. Chem. B* **1999**, *103* (5), 751–753.

(36) Schulz, H. *Appl. Catal. A Gen.* **1999**, *186* (1–2), 3–12.

Chapter 6 : Conclusions and Future Work

6.1 General Conclusions

The objectives of this thesis were to study the surface structure of a Co_3O_4 Fischer-Tropsch (FT) precursor catalyst and its reactivity towards syngas in contrast to H_2 to determine the most effective routes for the activation of Co where maximum reduction is achieved. Electron microscopy was used to explore the following research questions, as highlighted in the introduction:

d) Which surface terminations are found on the precursor Co_3O_4, and how do they compare to the theoretical Co_3O_4 surface terminations known to be active for CO and H_2 adsorption and dissociation?

e) What is the difference in the morphology, structure, and chemistry (valence state) of the Co FT catalyst when activated in H_2 compared to syngas activation?

f) How does temperature affect the properties in (b)?

6.1.1 Characterisation of Active Surfaces of the Co_3O_4 Precursor

Focal-series specimen exit wavefunction reconstruction (EWR) was used to study the surface structure and terminations of the Co_3O_4 precursor to answer question (a) above. The following conclusions were drawn from this study:

- From the electron dose experiments, it was concluded that the electron dose per frame in a focal series required to restore the specimen exit wavefunction, where both oxygen and cobalt atomic columns are resolved without visible beam-induced damage, is 1188 e/Å^2.
- Subsequently, the available surface atomic active sites for CO and H_2 adsorption were determined from the restored phase of the Co_3O_4 EWR from <110>, <111>, <510>, and <112> projections.
- By comparison with theoretical calculations, it was concluded that the {100} and {110} surfaces would have the highest reactivity towards CO due to the availability of octahedrally coordinated Co atoms, and surface O atoms to form a triangular Co–C–O coordination which is known to reduce the dissociation energy of CO.
- In contrast, the {115}, {112} surfaces would be more reactive towards H_2 due to the Co–O bridge site at the surface terminations.
- Of the examined surfaces, contraction of the Co–O projected distance relative to the bulk due to surface relaxation was observed on {100} surfaces viewed along <110> projections.
- Through comparison with DFT studies in the literature, it was concluded that the defective surfaces ({110}, and {113}) examined would be more reactive than perfect/flat surfaces.

6.1.2 The Activation of Co Fischer-Tropsch Catalysts in H_2 vs Syngas

After successful characterisation of the surface structure of the Co_3O_4 precursor, the effect of reducing gas atmosphere (H_2 or syngas) on the activation of Co FT catalysts was studied *ex-situ* and *in-situ* using STEM-ADF and EELS to answer questions (b) & (c). The following conclusions were drawn from this study:

- At 350 °C, *ex-situ* H_2 activation produced mainly CoO (Co^{2+} oxidation state) catalyst particles enclosed by {111} facets. In contrast, activation in syngas produced twinned fcc Co particles encapsulated in carbon fibres, and also produced core-shell particles, with a metallic Co core and a CoO shell.
- It was concluded that the oxidised shell was as a consequence of exposure to atmospheric air during sample transfer.
- Increasing the activation temperature to 600 °C helped to drive the complete reduction of CoO to active metallic Co in H_2. However, significant particle sintering was observed, which is a disadvantage of high-temperature activation.
- *In-situ* reduction in H_2 and syngas showed the absence of an oxide shell, confirming the reoxidation of Co catalyst during sample transport.
- Overall, it was concluded that syngas activation is the most effective method to obtain an active metallic Co sinter resistant catalyst at lower temperatures.

6.2 Recommendations for Future Work

6.2.1 *In-situ* Reduction of Co_3O_4 as a Function of Temperature and Time

The degree of reduction and the physical properties of the catalyst changes with increasing reduction time and temperature during activation.[1–4] These changes have been explored with *in-situ* X-ray techniques[2–4], and recently, with aberration-corrected environmental TEM[1] using H_2. However, there is no *in-situ* variable-temperature and time study which compares H_2 and syngas in the activation of Co FT catalysts. In this thesis, it was observed in Chapter 5 that increasing the reduction temperature to 600 °C improved the reducibility of Co_3O_4 in H_2. In addition, the 20 hrs *ex-situ* reduced catalysts were better reduced than 2 hrs *in-situ* reduced catalysts. As a result, in future work, it would be worth exploring the *in-situ* activation of the catalysts in H_2 and syngas as a function of temperature (i.e. from room temperature to 600 °C in 100 °C intervals), and also as a function of time at 350 °C. The results from the variable-temperature study would provide insight into the temperature at which full reduction is achieved since it is argued (Chapter 2, section 2.2) that syngas achieves complete reduction at a lower temperature (~230 °C) compared to H_2 (~600 °C). Furthermore, the changes in the properties of the catalysts with increasing temperature under different gases could be elucidated. A time-resolved isothermal study would shed light on the rate of activation in H_2 and syngas at 350 °C, and the dynamics of the carbon nanofibre growth and encapsulation of the Co particles in syngas.

6.3 General Outlook on the Future Applications of Advanced Electron Microscopy on Fischer-Tropsch and Heterogenous Catalysis

Advanced electron microscopy (*in-situ* and *ex-situ*) techniques applied in this thesis may yet be the critical tools required to unlock the mysteries of the Fischer-Tropsch catalysis and heterogeneous catalysis in general at the local scale. For example, post *in-situ* Co FT catalyst activation studies, FT synthesis could be performed *in-situ* by lowering the TEM holder temperature to 220-250 °C and passing the syngas feedstock over the activated catalyst. Thus, the physicochemical properties of the active catalyst, including the evolution of Co active surfaces, can be directly monitored *in-situ* as a function of CO conversion and product selectivity during the reaction. This allows for a direct correlation between the activation conditions, Co active sites, and subsequent catalytic activity and selectivity. The success of such an experiment will provide crucial insight into the dynamic relationship between catalyst surface structure, size, activity and selectivity.[5,6] This has been one of the most significant information gaps in the study of the effect of particle size on the catalytic activity and selectivity in Co FT synthesis, because conclusions are generally drawn from particle sizes before the activation and synthesis.[5,6] However, it has been shown that nanoparticles typically undergo morphological changes through sintering and surface rearrangements during reactions[7,8]– changes which are otherwise unobservable without *in-situ* EM.[9]

Additionally, one of the most important advancement in Fischer-Tropsch synthesis and heterogenous catalysis in general, is the development of multi-metal catalysts[2] and single-atom catalysts[10] in an effort to enhance the catalytic activity and selectivity. The direct imaging of

the location and interactions of different elements in a multi-metal catalyst requires the use of high-resolution Z-contrast imaging and EELS. For example, it has been shown that the position of Ru on a Ru-promoted Co catalyst plays a vital role in improving the reducibility of the catalyst through hydrogen spill over effect.[2] Thus, the use of high-resolution Z-contrast imaging in conjunction with EELS could provide direct evidence of the optimum dispersion of Ru to achieve maximum reduction through hydrogen spill over. Recently, single-atom catalysis has become the frontier of heterogenous catalysis.[10] However, due to the small differential scattering cross-section of a single atom, the current available imaging techniques capable of directly resolving an atom with sufficient contrast are limited to aberration-corrected Z-contrast imaging. This led to a series of high-impact publications.[10] Furthermore, the use of atomic resolution EELS will play a crucial role in the elemental mapping of single-atom catalysts.[11,12] Therefore, the future applications of advanced electron microscopy (*ex-situ* and *in-situ*) in catalysis will broaden our understanding of the fundamental key processes in catalysis, and the properties of novel complex multi-metal catalysts and single-atom catalysts.

6.4 References

(1) Ward, M. R.; Boyes, E. D.; Gai, P. L. *ChemCatChem* **2013**, *5* (9), 2655–2661.

(2) Phaahlamohlaka, T. N.; Kumi, D. O.; Dlamini, M. W.; Forbes, R.; Jewell, L. L.; Billing, D. G.; Coville, N. J. *ACS Catal.* **2016**, acscatal.6b03102.

(3) Hoffman, A. S.; Singh, J. A.; Bent, S. F.; Bare, S. R. *J. Synchrotron Radiat.* **2018**, *25* (6), 1673–1682.

(4) Garces, L. J.; Hincapie, B.; Zerger, R.; Suib, S. L. *J. Phys. Chem. C* **2015**, *119* (10), 5484–5490.

(5) Liu, J.-X.; Wang, P.; Xu, W.; Hensen, E. J. M. *Engineering* **2017**, *3* (4), 467–476.

(6) den Breejen, J. P.; Radstake, P. B.; Bezemer, G. L.; Bitter, J. H.; Frøseth, V.; Holmen, A.; de Jong, K. P. *J. Am. Chem. Soc.* **2009**, *131* (20), 7197–7203.

(7) Simonsen, S. B.; Chorkendorff, I.; Dahl, S.; Skoglundh, M.; Sehested, J.; Helveg, S. *J. Catal.* **2011**, *281* (1), 147–155.

(8) Somorjai, G. A. *The Flexible Surface. Correlation between Reactivity and Restructuring Ability*; 1991; Vol. 7.

(9) He, B.; Zhang, Y.; Liu, X.; Chen, L. *ChemCatChem* **2020**, *12* (7), 1853–1872.

(10) Wang, A.; Li, J.; Zhang, T. *Nat. Rev. Chem.* **2018**, *2* (6), 65–81.

(11) Krivanek, O. L.; Dellby, N.; Hachtel, J. A.; Idrobo, J. C.; Hotz, M. T.; Plotkin-Swing, B.; Bacon, N. J.; Bleloch, A. L.; Corbin, G. J.; Hoffman, M. V.; Meyer, C. E.; Lovejoy, T. C. *Ultramicroscopy* **2019**, *203*, 60–67.

(12) Kimoto, K.; Asaka, T.; Nagai, T.; Saito, M.; Matsui, Y.; Ishizuka, K. *Nature* **2007**, *450* (7170), 702–704.